工學博士學位論文

Fabrication of Shape-Controlled Graphenes Based on 'Top-down' and 'Bottom-up' Approaches and Their Applications

하향식/상향식 접근방법을 통한 형태 조절된 그래핀의 제조 및 응용

2013年 2月

서울大學校 大學院

化學生物工學部

洪 鎭 庸

Fabrication of Shape-Controlled Graphenes Based on 'Top-down' and 'Bottom-up' Approaches and Their Applications

하향식/상향식 접근방법을 통한 형태 조절된 그래핀의 제조 및 응용

指導敎授: 張 正 植

이 論文을 工學博士 學位論文으로 提出함

2012年 10月

서울大學校 大學院

化學生物工學部

洪 鎭 庸

洪 鎭 庸의 工學博士 學位論文을 認准함

2012年 11月

委 員 長 _____

副委員長 _____

委 員 _____

委 員 _____

委 員 _____

Fabrication of Shape-Controlled Graphenes Based on 'Top-down' and 'Bottom-up' Approaches and Their Applications

by

Jin–Yong Hong

Submitted to the Graduate School of Seoul National University

in Partial Fulfillment of the Requirements

for the Degree of Doctor of Philosophy

February, 2013

Thesis Adviser: Jyongsik Jang

ABSTRACT

Graphene, typically composed of one-atom-thick layer of carbon in a 2D hexagonal lattice, is a basic building block for graphitic materials of all other dimensionalities. The graphene has attracted tremendous worldwide attention because of their fascinating properties different from those of the carbon-based graphitic materials (*e.g.*, extremely high charge carrier mobility, large specific surface area, thermal/electrical conductivity, and chemical/mechanical stability). Up to date, various synthetic methods for preparing graphene have been developed. However, most previous synthetic methods suffer from the precise control of the size, shape, edge, layer of graphene sheets. Consequently, it is still challenging to produce graphene with tailored morphology and diameters for various applications.

This dissertation describes the two different ways in the synthetic methodology of graphene will be presented in the viewpoint of top-down approach and bottom-up approach. As a ‘top-down approach’, the graphene sheets with well-defined shape are successfully fabricated using a simple oxidation and exfoliation process of high-crystalline carbon nanofibers (CNFs). Interestingly, the diameter and shape of the graphene sheets can be controlled

by selectively designing the morphology of starting materials and optimizing the cutting method. As a 'bottom-up approach', graphene sheets are formed using layer-by-layer (LbL) self-assembly approach with a metallic dopant. The LbL approach is used to form poly(allylamine)(PAA)/poly(styrenesulfonate) (PSS) multilayer on a quartz substrate. During the carbonization process, the PSS layers can be transformed into graphene sheets due to its inherent aromatic and highly ordered structure. PAA layers served to protect the structural layers as well as prevent the agglomeration of graphene sheets. Most, importantly, these novel approaches can be used as an alternative tool for fabrication of various carbon-based nanomaterials with rational nanostructure design and may offer an opportunity for the further investigation of industrial applications, and might be expanded to allow the applications of graphene sheets in a wide range of areas (*e.g.*, Transparent electrode, dipole antenna, acoustic actuator, nucleating agent, nano-filler, electro-responsive materials, and so on.).

KEYWORDS: Carbon nanomaterials; Graphene; Synthetic methodology; Top-down; Bottom-up; Transparent electrode; Electrorheological fluid

STUDENT NUMBER: 2006–21396

List of Abbreviations

μCP : microcontact printing

1D : one-dimensional

2D : two-dimensional

3D : three-dimensional

AAO : anodic aluminum oxide

AFM : atomic force microscope

ANC : adaptive noise cancellation

APS : ammonium persulfate

C_{60} : fullerene

CNFs : carbon nanofibers

CSR : controlled shear rate

CVD : chemical vapor deposition

EA : elemental analysis

EG : epitaxial graphene

ER : electrorheological

FE-SEM : field emission scanning electron microscopy

FET : field effect transistor

FT-IR : fourier transform infrared

G : gravitational acceleration

GICs : graphite intercalation compounds

GNRs : graphene nano ribbons

GO : graphene oxide

GPCNFs : graphitized platelet carbon nanofibers

GT : green technology

HCNFs : herringbone type of carbon nanofibers

ITO : indium tin oxide

I–V : current–volatge

LbL : layer-by-layer

LEDs : light emitting diodes

LPCVD : low pressure chemical vapor deposition

MICS : medical implant communication service

MWCNT : multi-walled carbon nanotube

NMR : nuclear magnetic resonance

OFET : organic field-effect transistors

OLEDs : organic light-emitting diodes

OM : optical microscope

PAA : poly(allylamine)

PAHs : polycyclic aromatic hydrocarbons

PANI : polyaniline

PCNFs : platelet carbon nanofibers

PDMS : polydimethylsiloxane

PEDOT : poly(3,4-ethylenedioxythiophene)

PET : polyethylene terephthalate

PPy : polypyrrole

PSS : poly(styrenesulfonate)

PVDF : poly(vinylidene fluoride)

PYR-NHS : 1-pyrenebutanoic acid succinimidyl ester

RFID : radio frequency identification

rGO : reduced graphene oxide

RL : return loss

SiC : silicon carbide

SWCNT : single-walled carbon nanotube

TEM : transmission electron microscopy

UHV : ultrahigh vacuum

UV-vis : ultraviolet-visible

VDP : vapor deposition polymerization

V_g : sedimentation velocity

VSWR : voltage standing wave ratio

XPS : X-ray photoelectron spectroscopy

XRD : X-ray diffraction

η : viscosity

ρ_l : liquid density

ρ_p : particle density

τ_y : yield stress

List of Figures

Figure 1. Structures of various important carbon nanomaterials.

Figure 2. The procedure followed for the production of chemically-modified graphenes using graphite as the starting material.

Figure 3. Schematic diagram and photographs of the roll-based production of graphene films grown on a copper foil.

Figure 4. Variation in resistance of a graphene film for different distances between holding stages.

Figure 5. Schematic illustration and electrical characteristics of high-performance, transparent, stretchable graphene FETs on a PDMS rubber substrate.

Figure 6. Vapor sensing by inkjet-printed rGO/PET obtained by ascorbic acid reduction of dispersed graphene oxide.

Figure 7. Schematics of CO_2 laser-patterning of free-standing hydrated GO films to fabricate rGO–GO–rGO devices with in-plane and sandwich geometries.

Figure 8. a) Plausible formation procedure of graphene layers with well-defined shape using the platelet carbon nanofibers. b) HR-TEM images of as-prepared PCNFs. c) TEM image of GPCNFs. d) STM images of isolated graphitized CNFs.

Figure 9. TEM images (a-e) for oxidized GPCNFs as a function of mass ratio of oxidant to GPCNFs: a) pristine GPCNFs, b) $R_{K/GP}$=1, c) $R_{K/GP}$=2, d) $R_{K/GP}$=3, e) $R_{K/GP}$=6 (inset: related schematic illustration), f) AFM image of exfoliated oxidized graphene discs with the mean thickness of 1.2 nm.

Figure 10. XRD patterns of platelet CNF, graphitized platelet CNFs (GPCNFs), and oxidized GPCNFs (inset: Changes in XRD patterns of GPCNFs as a function of $R_{K/GP}$ value).

Figure 11. Solid ^{13}C NMR of oxidized GPCNFs with a different $R_{K/GP}$ value.

Figure 12. XPS spectra of oxidized GPCNFs with different mass ratios of $R_{K/GP}$ value.

Figure 13. TEM images of as-prepared (a, b) and graphitized platelet carbon nanofibers (c). The platelet carbon nanofibers has relative small

diameter of ca. 30–50 nm, allowing the fabrication of small-diameter graphene discs (d). Graphene discs are oxidized under controlled conditions ($R_{K/GP}$=3) and reduced by using mechanical reduction method.

Figure 14. TEM images of (a) graphitized herringbone carbon nanofibers and (b) oxidized graphitized herringbone carbon nanofibers ($R_{K/GP}$=3) (inset: isolated bow-tie shaped graphene discs).

Figure 15. Schematic illustration for reduction of hydroxyl and epoxy groups for oxidized graphene discs to reduced graphene discs trans-formation.

Figure 16. UV-vis absorption spectra of reduced graphene discs solution as a function of reduction time.

Figure 17. Raman spectra of reduced graphene discs, oxidized graphene discs, GPCNFs and PCNFs. Graphene discs are oxidized under controlled conditions ($R_{K/GP}$=6) and reduced by using mechanical reduction method.

Figure 18. XPS Survey of a) oxidized graphene discs and b) reduced graphene discs. (right: XPS C1s spectra of oxidized graphene discs and reduced graphene discs) Graphene discs are oxidized under controlled conditions ($R_{K/GP}$=6) and reduced by using mechanical reduction method.

Figure 19. FT-IR spectra of reduced graphene discs, oxidized graphene discs and GPCNFs. Graphene discs are oxidized under controlled conditions ($R_{K/GP}$=6) and reduced by using mechanical reduction method.

Figure 20. A non-contact mode AFM image of a) oxidized graphene disc and b) reduced graphene disc with height profiles along the diagonal line in the image.

Figure 21. Graphene discs are oxidized under controlled conditions ($R_{K/GP}$=6) and reduced by using mechanical reduction method. UV-vis absorption spectra of oxidized graphene disc solution. Graphene disc solution reduced by water, ethylene glycol, N, N-dimethylformamide, n-butanol and ethanol, respectively.

Figure 22. Various graphene discs solution is oxidized under controlled conditions ($R_{K/GP}$=6) and reduced by using mechanical reduction method.

Figure 23. Formation mechanism for the multi-layer epitaxial graphene nanosheets on a quartz substrate.

Figure 24. Thermogravimetric analysis of PSS and PAA.

Figure 25. TEM image of graphene nanosheets prepared by LbL self-assembly approach: (a) with a metallic dopant, (b) without a metallic dopant.

Figure 26. TEM image of graphene single nanosheet prepared by LbL self assemble (inset: Raman spectrum of graphene nanosheets (thickness~100 nm) deposited on a silicon wafer).

Figure 27. Raman spectra of resulting as-carbonized PSS/PAA multi-layers under various carbonization temperatures.

Figure 28. AFM image of graphene nanosheets (inset: a line scan taken vertically through the dashed line on the topography image).

Figure 29. Deconvoluted XPS spectrum for graphene nanosheets.

Figure 30. Survey XPS of as-synthesized graphene nanosheets.

Figure 31. Transmission spectra of graphene sheet as a function of sheet thickness.

Figure 32. Digital photograph images of the filtration-wet transfer process. A uniform flexible graphene nanosheet film was obtained by vacuum filtration using an AAO membrane and transferred to a PET film.

Figure 33. Transmittance (550 nm) and sheet resistance of prepared graphene sheets as a function of thickness. (inset: The same data represented by transmittance versus sheet resistance).

Figure 34. *I–V* characteristics of graphene sheet at a scan rate of 50 mVs^{-1}.

Figure 35. Designed graphene-based electronic circuit pattern for ink-jet printing.

Figure 36. Digital photographs of graphene-based electronic circuit turn off and turn on.

Figure 37. Sheet resistance changes of graphene-based electronic circuit as a function of bending angle (inset: schematic diagram of graphene film on polymer substrate and folded to various angles).

Figure 38. a) The fabrication of patterned GO on PET film by inkjet printing. b) Large-area patterned GO (left image) and graphene sheets resulted from the reduction procedure (right image). c) The reduction process was performed by mild-thermal annealing at 90 °C with hydrazine and ammonia vapor.

Figure 39. a) AFM image of patterned graphene sheets with 70 μm line width obtained by inkjet printing for 1 pass and reduction process (observable range of AFM : 50 μm) b) The film thickness of patterned graphene sheets as a function of printing number.

Figure 40. The various optical images of a) graphene sheets b) PPy c) PANI patterns prepared by inkjet printing and VDP method. The optic images were magnified at marked areas.

Figure 41. The optical micrographs of patterned straight lines of a) graphene sheets b) PPy c) PANI with the width of *ca.* 70 μm. In all images, the scale bar is 50 μm.

Figure 42. The optical micrographs of patterned graphene-based thin film with the width of a) *ca.* 70 μm b) *ca.* 100 μm c) *ca.* 200 μm. In all cases,

the scale bar is 50 μm. d) The electrical measurement of the full line and consecutive repeated pattern having a gap of 70 μm between dots in the dotted line by using the multimeter. The pattern was magnified by optical microscopy (scale bar: 125 μm).

Figure 43. The photo image of gradient patterned graphene sheets with controlled surface resistance as a function of lightness. Grayscale images were designed by computer software.

Figure 44. Surface resistance of patterned graphene sheets as functions of the GO concentration and printing number. The surface resistance was measured by four-probe method, and patterned graphene-based thin film has minimum sheet resistance of 65 Ω sq^{-1} (30 times printing with 0.7 % GO ink).

Figure 45. The return loss curve of the dipole antenna application using patterned graphene sheets electrode. (inset: Smith chart impedance diagram of designed dipole antenna).

Figure 46. a) Schematic illustration and b) photograph of PVDF-based thin film acoustic actuator using flexible and transparent graphene

electrodes. The P and F meant polarization and force of the acoustic actuator, respectively.

Figure 47. Fabrication of graphene electrodes on PVDF film by inkjet printing and vapor deposition process. The reduction process was performed by mild-thermal annealing at 90 °C with hydrazine and ammonia vapor.

Figure 48. Comparison of deconvoluted XPS spectrum of pristine PVDF, O_2 plasma treated PVDF films, exfoliated GO by inkjet printing for 10 passes and graphene thin films resulted from the reduction procedure onto the PVDF substrate in the C1s region.

Figure 49. Raman spectra of GO and graphene film on the PVDF substrate showing G and D peaks.

Figure 50. Film thickness of graphene electrodes as a function of the printing number using inkjet printing and reduction process (Inset: AFM image of graphene film acquired by inkjet printing for 1 pass which has observable range of 50 μm).

Figure 51. Surface sheet resistances of graphene-based PVDF films with different film thickness (Inset: the data represented by transmittance versus sheet resistance with the same film thickness). The average layer thickness is considered to be ca. 15~20 nm.

Figure 52. The frequency response of the graphene-based thin film transducer with three different electrode thickness (60, 90 and 120 nm) compared to the PEDOT:PSS-based commercial thin film transducer.

Figure 53. Each frequency response at the flat and bending conditions (radius: 6 cm) of graphene-based thin film transducer with 120 nm electrode thickness.

Figure 54. The ANC effect on the harmonics of graphene-based thin film transducer from 3 kHz tonal signal. A soft substrate (3M VHB4910 acrylic form tape) was cleaved to the film to make an ANC actuator (stars indicate harmonic sounds at multiples of 3 kHz).

Figure 55. Schematic illustration of the different steps for fabricating GO sheet-based ER fluids.

Figure 56. a) Photographs of the GO sheet-based ER fluid prepared by centrifugation of dispersion of GO sheets in ethanol (upper phase) and silicone oil (lower phase). b) Extrusion of the GO sheet-based ER fluid from a needle.

Figure 57. Schematic illustration for the dispersing state of (a) solvent exchanged GO sheets and (b) mechanically grinded GO sheets.

Figure 58. Effect of switching the applied electric field on the shear stress of the GO sheet-based ER fluids (5 wt% in silicone oil).

Figure 59. Shear stress for the 5 wt% of GO sheet-based ER fluids under electric field strength (5 kV/mm). Open and closed symbols indicate with and without electric field strengths, respectively.

Figure 60. Dynamic yield stress as a function of weight fraction for the GO sheet-based ER fluids under 5 kV/mm of electric field [inset: Dynamic yield stress of various GO sheet-based ER fluids as a function of electric field strength (5 wt% in silicone oil)].

Figure 61. (a-d) Microscope images of chain formation in silicone oil suspension of GO (5 wt % in silicone oil) under an applied electric

fields of 1 kV mm^{-1}. The gap between two electrodes was fixed to 1.0 mm.

Figure 62. Sedimentation properties of two different types of GO sheet-based ER fluids (1 wt% in silicone oil) [inset: definition of sedimentation ratio].

List of Tables

Table 1. Elemental and physical parameter of oxidized GPCNFs.

Table 2. Electrical properties of as-prepared samples.

Table 3. *VSWR* and *RL* of designed dipole antenna by patterned graphene sheets.

Table 4. Off-field viscosity of GO sheets in silicone oil.

Table 5. Physical parameters and sedimentation velocity of GO sheets in silicone oil.

Table of Contents

ABSTRACT i

List of Abbreviations iii

List of Figures vii

List of Tables xix

Table of Contens xx

1. INTRODUCTION 1

1.1. Background 1

1.1.1. Graphene 1

1.1.2. Synthesis of graphene 4

1.1.2.1. Exfoliation 5

1.1.2.2. Epitaxy on silicon carbide 8

1.1.2.3. Chemical vapor deposition 9

1.1.2.4. Chemical synthesis 12

1.1.3. Application fields 14

1.1.3.1. Electrode 15

1.1.3.2. Transistor 18

1.1.3.3. Chem/Bio sensor 21

1.1.3.4. Supercapacitor 24

1.2. Objectives and Outline of the Study 27

1.2.1. Objectives 27

1.2.2. Outline 27

2. EXPERIMENTAL DETAILS 32

2.1. 'Top-down' Approach for Fabricating Uniform Graphene Sheets with Disc Shape 32

2.1.1. Preparation of graphitized carbon nanofibers 32

2.1.2. Transversal cutting of graphitized carbon nanofibers 32

2.1.3. Mechanical reduction of oxidized graphene sheets 33

2.2. 'Bottom-up' Approach for Fabricating Single Layer Graphene Sheets based on a Layer-by-Layer Self-assembly 35

2.2.1. Preparation of poly(allylamine)/poly(styrenesulfonate) (PAA/PSS) multi-layer using layer-by-layer self-assembly 35

2.2.2. Carbonization of PSS/PAA multi-layer and oxidation/ reduction of graphene sheets 37

2.3. Applications 39

2.3.1. Foldable graphene electrode using ink-jet printing method 39

2.3.2. Graphene patterning *via* ink-jet printing method and their application to wideband dipole-antenna 41

2.3.3. Flexible & transparent graphene electrode as an acoustic actuator using inkjet printing 45

2.3.4. Electrorheological properties of graphene suspensions with improved sedimentation stability 48

3. RESULTS AND DISCUSSION 51

3.1. 'Top-down' Approach for Fabricating Uniform Graphene Sheets with Disc Shape 51

3.1.1. Preparation of graphitized carbon nanofibers 51

3.1.2. Transversal cutting of graphitized carbon nanofibers 54

3.1.3. Mechanical reduction of oxidized graphene sheets 65

3.2. 'Bottom-up' Approach for Fabricating Single Layer Graphene Sheets based on a Layer-by-Layer Self-assembly 82

3.2.1. Preparation of poly(allylamine)/poly(styrenesulfonate) (PAA/PSS) multi-layer using layer-by-layer self-assembly 82

3.2.2. Carbonization of PSS/PAA multi-layer and oxidation/reduction of graphene sheets 86

3.3. Applications 97

3.3.1. Foldable graphene electrode using ink-jet printing method 97

3.3.2. Graphene patterning *via* ink-jet printing method and their application to wideband dipole-antenna 107

3.3.3. Flexible & transparent graphene electrode as an acoustic actuator using inkjet printing 121

3.3.4. Electrorheological properties of graphene suspensions with improved sedimentation stability 136

4. CONCLUSIONS 154

REFERENCES 158

국문초록 171

1. INTRODUCTION

1.1. Background

1.1.1. Graphene

Graphene, a one-atom-thick planar sheet of sp^2-bonded carbon atoms densely packed in a honeycomb crystal lattice, has grabbed appreciable attention to be used as a next generation electronic material, due to its exceptional properties including high current density, ballistic transport, chemical inertness, high thermal conductivity, optical transmittance and super hydrophobicity at nanometer scale (Figure 1) [1,2]. Graphene has been extensively studied in the last several years even though it was only isolated for the first time in 2004 [3]. Andre Geim and Konstantin Novoselov won the 2010 Nobel Prize in Physics for their groundbreaking work on graphene. The fast uptake of interest in graphene is due primarily to a number of exceptional properties that it has been found to possess.

Intrinsic graphene is characterized as a semi-metal or zerogap semiconductor and its unique electronic properties produce an unexpectedly high opacity for an atomic monolayer, with a startlingly low absorption ratio of 2.3 % of white light [4]. Electrical characterization has shown a remarkable high electron mobility at room temperature, with experimentally reported values in excess of 15,000 $cm^2 V^{-1} s^{-1}$ [5]. The corresponding resistivity of the

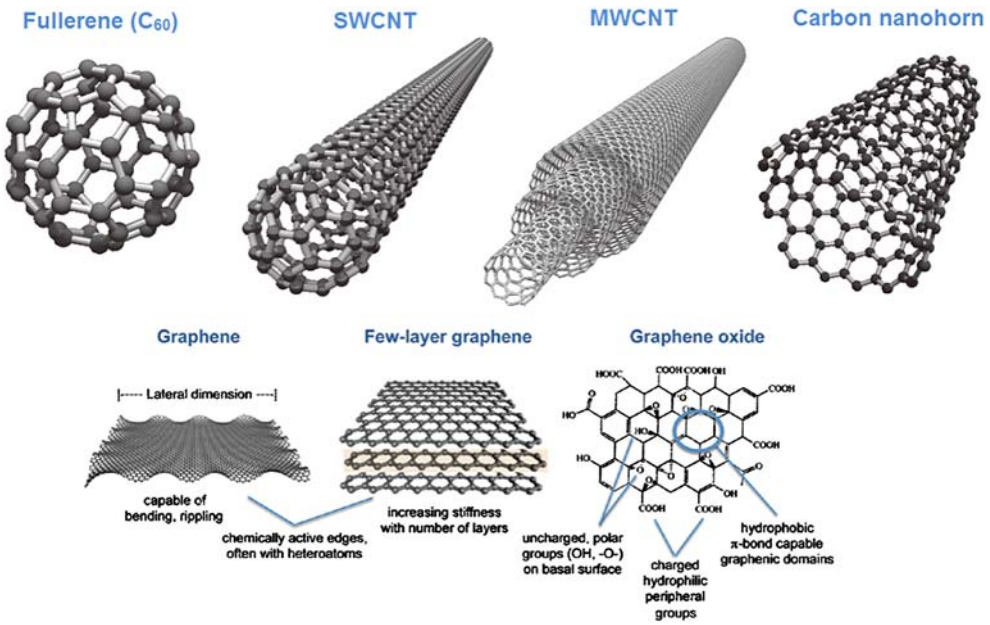

Figure 1. Structures of various important carbon nanomaterials: fullerene (C_{60}), single-walled carbon nanotube (SWCNT), multi-walled carbon nanotube (MWCNT), carbon nanohorn, graphene, few layer graphene and graphene oxide. Reprinted with permission. Copyright 2012 Elsevier.

graphene sheet would be 10^{-6} ohm–cm, less than the resistivity of silver, the lowest resistivity substance known at room temperature [6]. Graphene nano ribbons (GNRs), with zigzag or armchair configuration, show different electrical property; the zigzag GNRs are metallic, while armchairs can be either metallic or semiconductor. The energy band gap of armchair GNRs are inversely proportional to the width [6].

Exceptional electrical properties of graphene have attracted applications for future electronics such as ballistic transistors, field emitter, components of integrated circuits, transparent conducting electrodes and sensors. Graphene has a high electron (or hole) mobility as well as low Johnson noise (electronic noise generated by the thermal agitation of the charge carriers inside an electrical conductor at equilibrium, which happens regardless of any applied voltage), allowing it to be utilized as the channel in a field effect transistor (FET). Combination of excellent electrical property and low noise make graphene an excellent sensor. Its entire volume is exposed to the surrounding due to its 2D structure, making it very efficient to detect adsorbed molecules. The high electrical conductivity and high optical transparency promote graphene as a candidate for transparent conducting electrodes, required for applications in touch-screens, liquid crystal displays, organic photovoltaic cells and organic light-emitting diodes (OLEDs) [6].

1.1.2. Synthesis of graphene

Creating high-quality graphene in scalable, economical processes is the first step towards practical application of graphene. Work on isolating graphene has progressed over many decades of research [7]. The structure of graphite, and essentially graphene as well, was known since the invention of x–ray diffraction crystallography. However, it was unknown weather or not a truly two dimensional crystal could exist, as extraplanar phonons would be entropically overwhelming over long ranges [8]. Solution-based exfoliation of graphite (*i.e.*, *via* oxidation or graphite intercalation compounds (GICs)) gave an early look at realizing atomic planes of carbon [9]. In the 1960s, Boehm speculated that reducing exfoliated graphite oxide would yield monolayers in solution [10], though the term 'graphene' was not coined until 1986 [11] and formally accepted in 1994 [12]. A number of early studies found monolayers of carbon in graphitic structures, formed on various carbide [13–15] and transition metal [16–20] surfaces, as early as van Bommel in 1975 with SiC. [21] These surface science and chemistry studies did not explore any electronic properties, as the strongly bound metallic surfaces disrupt the perpendicular π orbitals, with the exception of SiC. The first electronic measurements of ultrathin graphitic carbon around 2004 required samples sufficiently isolated from its substrate, (*e.g.*, on SiO_2) and ignited an explosion of interest in the field.

[22,23] Synthesis techniques can be categorized into micromechanical exfoliation, solution-based and chemically assisted exfoliation, chemical synthesis, epitaxial growth through sublimated SiC surfaces, and the pyrolysis of hydrocarbons on metal surfaces. Each has its own advantages, challenges, shortcomings, and unique features in terms of processability, quality, scalability and cost.

1.1.2.1. Exfoliation

The exfoliation of graphite is a process in which bulk graphite can be separated into single atomic planes. Attempts prior to development of the so-called “Scotch tape method” were unable to observe isolated single layers [24,25]. Ever since the first graphene discovered using micromechanical cleavage of bulk graphite, this method has been widely used to prepare high-quality graphene samples, which is less formally called peeled graphene. The technique is quite simple; utilizing everyday adhesive tape to repeatedly peel layers off of highly oriented pyrolytic graphite and pressing it onto an appropriate substrate, typically but not limited to oxidized silicon [26].

Chemical exfoliation of graphite in solution represents one potential approach to high volume production of graphene. As opposed to direct physical cleavage, chemicals are used to intercalate bulk graphite by inserting reactants

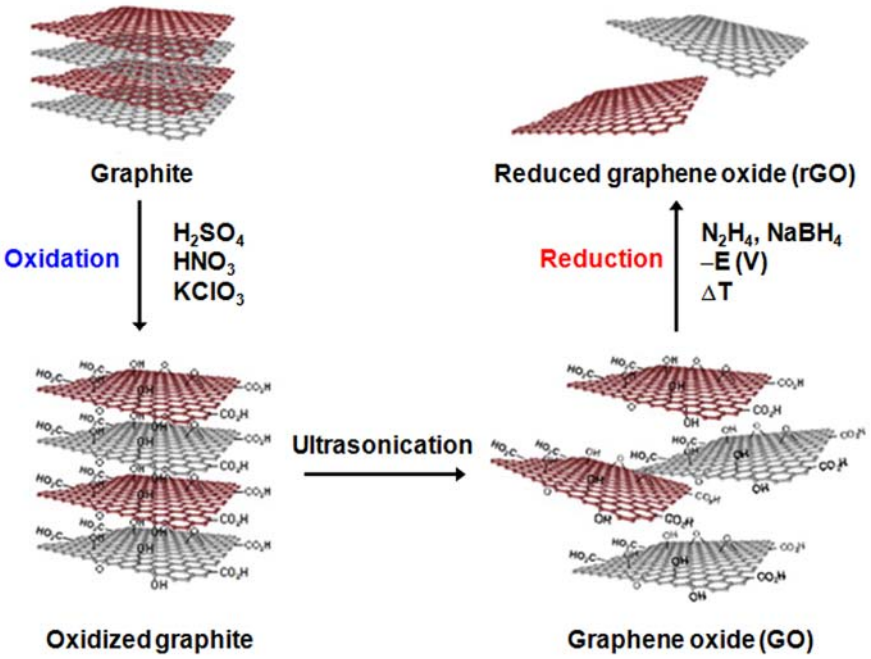

Figure 2. The procedure followed for the production of chemically-modified graphenes using graphite as the starting material. This is followed by: (1) An oxidative treatment is initially performed to generate oxidized graphite; (2) exfoliation by ultrasonication to generate GO; (3) reduction of GO by using various reduction methods to produce rGO.

between layers that weaken the cohesive van der Waals force [27]. Dai's group was the first to report success in producing high-quality, single-layer graphene sheets, stably suspended in organic solvents by steps of chemical intercalation, reintercalation, and sonication [28]. A liquid exfoliation approach has also been reported to produce graphene by sonicating graphite powder in N-methylpyrroidone [29]. A homogeneous colloidal suspension of graphene sheets or ribbons can be made simply by stirring in surfactant solution.

A more efficient way to obtain large volumes of graphene is by firstly synthesis of graphite oxide, then exfoliation into monolayers, and finally reduction to remove the oxygen [30,31]. The Brodie, Staudenmeier and Hummers methods are the three most common ways to oxidize graphite. Among these, a slightly modified Hummers method has become the most popular in producing graphite oxide, for its relatively shorter reaction time and absence of toxic side products (Figure 2). After oxidation, the interlayer spacing increases from 0.34 nm in graphite to above 0.6 nm, with weakened van der Waals forces between the layers. Exfoliation is typically augmented with sonication, yielding single layers of graphene oxide (GO), which are soluble in water without the assistance of surfactants to form a stable colloidal system. Many methods of removing the oxygen from the GO structure through chemical, [32] thermal, [33] electrochemical [34] or electromagnetic flash [35]

and laser-scribe [36] techniques have been successful, but generally resulted in inferior samples which are hence more precisely named reduced graphene oxide (rGO).

1.1.2.2. Epitaxy on silicon carbide

Epitaxial graphene (EG) growth on silicon carbide (SiC) surfaces is an effective bottom-up approach to create carbon-based electronics, which has been demonstrated on wafer scale. [37,38] The pioneering work on EG was conducted by heating 6H-SiC in ultrahigh vacuum (UHV) in the temperature range of 1200–1600 °C. The silicon atoms on the surface sublimate at high enough temperature and the exposed carbon atoms reconstruct to form graphitic layers. EG can grow on both the C-terminated and Si-terminated surfaces, though films grow much faster on the carbon face. [39]

Surfaces of cubic 3C-SiC (β-SiC) are also capable of epitaxial growth, with low interface interaction, and cheaper, commercialized β-SiC/Si wafers. [40] Most EG growth is accomplished in UHV. However, larger, several-micrometer domains have been obtained in an argon atmosphere. Direct growth of graphene nanoribbons has been achieved on prefabricated SiC nanofacets, utilizing crystal plane selective growth rates from a lowered surface free energy. SiC offers a suitable insulating structure in which devices

can be fabricated with a sufficient buffer layer that isolates the graphene π orbitals, keeping the linear dispersion intact. Transferring EG to arbitrary substrates using thermal release tape has been accomplished, without a significant drop in carrier mobility. [41] Industrial scale growth on SiC is primarily limited by the high cost of single-crystal SiC wafers.

1.1.2.3. Chemical vapor deposition

Chemical vapor deposition (CVD) method has emerged to be one of the most promising techniques for the large-scale production of single and multiple layer graphene films. Uniform, wafer size graphene films have been grown on both single crystal and polycrystalline transition metal surfaces at high temperatures by pyrolysis of hydrocarbon precursors such as methane. [42–44] Figure 3 shows the largest continuous area of CVD graphene reported to date: 30-inch diagonal length, grown on copper foil in an 8-inch diameter quartz tube at low pressure [45]. The number of graphene layers depends highly on the carbon solubility of the substrate. For metals with relatively high carbon solubility, such as nickel, [46] the carbon atoms can dissolve at high temperature, then precipitate onto the metal surface and form single or multilayer graphitic films upon cooling. These non-uniform films with a wide thickness range from 1 to around 10 layers with monolayer domain sizes up to

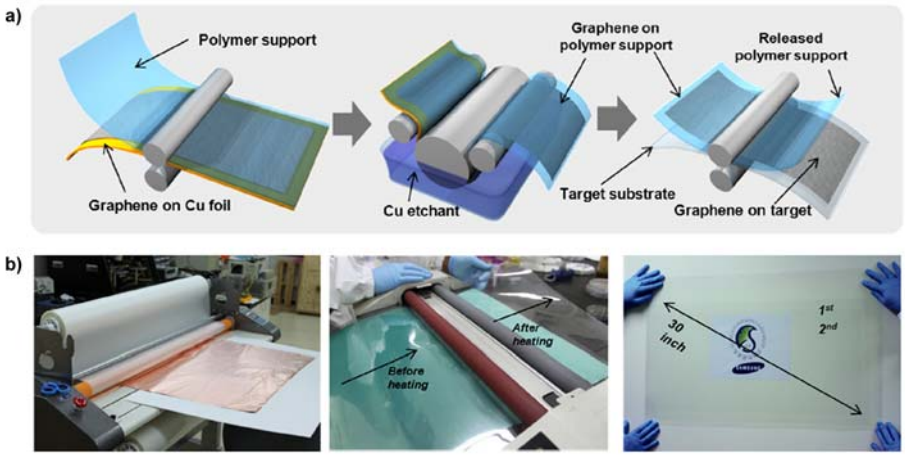

Figure 3. a) Schematic diagram of the roll-based production of graphene films grown on a copper foil. The processes are divided into three steps: (1) the adhesion of polymer supports, (2) copper etching and (3) transfer to the target substrate. b) Photographs of the roll-based production of graphene films on copper foil produced by the process shown in panel (a). Reproduced with permission from Ref. 45. Copyright 2010 Right Managed by Nature Publishing Group.

several tens of micrometers in diameter were produced on nickel substrates [47]. The thickness and crystal ordering can be controlled by the cooling rate and hydrocarbon gas concentration. On the other hand, low carbon solubility in certain transition metals, for instance copper [48] and platinum [49] enables complete monolayer coverage [50].

Lattice mismatch between the metal surface and graphene typically forms a pseudomorphic interface and generally displays a moiré pattern as well as lattice strain. Graphene epitaxially grown on single crystal metal substrates can avoid surface defects on the metal grain boundaries and help to mitigate orientation mismatch, however still has significant misaligned domains and grain boundaries. Polycrystalline films offer a more economical alternative that is still capable of large domains without noticeable performance difference within individual domains.

Yan and coworkers broke the self-limiting effect of the low pressure chemical vapor deposition (LPCVD) process to enable second layer growth on prepared monolayer graphene using a fresh copper foil placed in the high-temperature upstream regime. Bernal AB-stacked bilayer graphene is possible with coverage area as high as 67 %, which shows typical gate response. [51] Furthermore, Chen and coworkers report the synthesis of controllable mono- and multilayer graphene films on Cu 0.69 Ni 0.31 alloy foils by LPCVD. By

using the alloy of low- and high-solubility catalysts, both thickness and quality of the films can be controlled by the growth temperature and cooling rate. [52]

The recent achievements in graphene growth by thermal CVD has confirmed reproducibility of good quality graphene on a centimeter scale substrate and successful transfer to many other substrates including Si, glass and polydimethylsiloxane (PDMS). These developments create new pathways for application of graphene in photovoltaic and flexible electronics. However, in near future, issues like growth of graphene on wafer size substrates, controlling efficiently the number of layers should be solved, for creating more interest in actual applications.

1.1.2.4. Chemical synthesis

Another alternative route for the controllable production of graphene is bottom-up organic synthesis. Graphene can be composed of interconnected polycyclic aromatic hydrocarbons (PAHs), which are very small two-dimensional graphene segments. This approach is attractive due to its high versatility and compatibility with various organic synthesis techniques. [53] Müllen and coworkers are pioneers in this field, reporting synthesis of nanoribbon like PAHs with lengths over 30 nm. [54,55] Recently, the largest stable colloidal graphene quantum dots were synthesized using a benzene-

based chemical route, which compose 132, 168, 170 conjugated carbon atoms. [56,57] However, the size of the as-grown graphene dots is limited due to decreasing solubility as sizes increase as well as an increasing number of possible side reactions, which is still a major challenge for organic synthesis of graphene molecules with controllable shapes, sizes and edge structures.

1.1.3. Application fields

Graphene has shown exceptional electrical, optoelectrical, mechanical and chemical properties and thus, has emerged to be a valuable platform for various applications. Graphene is intrinsically metallic and can be found in a number of promising applications utilizing it as a passive conducting component. Use of graphene as a conductor takes advantage of the exceptionally high conductivity considering its incredibly small form factor. The sheet resistance of an undoped pristine graphene monolayer is around 6 $k\Omega\ sq^{-1}$ at the charge neutrality point. [6] The conductivity can be increased by using electrostatic doping, or more practically *via* chemical doping, to increase carrier concentration. Additional advantages include its exceptional transparency, surface area, mechanical strength and flexibility. The following application fields of graphene pave the way for the practical application and industrialization of the advanced science and technology.

1.1.3.1. Electrode

Typically, indium tin oxide (ITO) is one of the most widely used transparent conducting material. However, high cost, limited supply and brittle nature of indium restricts its application in flexible substrate, motivating the search for highly transparent and conducting materials to replace ITO. The next generation of optoelectronic devices requires transparent conductive electrodes to be lightweight, flexible, cheap, environmentally attractive, and compatible with large-scale manufacturing methods. As mentioned previously, the extraordinary thermal, chemical and mechanical stability of graphene, combined with its superior carrier mobility and high transparency, the graphene is considered to be a promising material for future optoelectronic devices.

Previous researches show that graphene has a transmittance and sheet resistance combination comparable to conventional ITO films, and can be a viable alternative technology. Many devices that utilize transparent electrodes can benefit from using graphene electrodes such as transparent transistors, [58,59] displays, touch-panels, and optoelectronics.

With excellent mechanical strength and elasticity in addition to its electronic properties, graphene on a flexible substrate can offer exciting opportunities for bendable, rollable, foldable, and stretchable electronics [60].

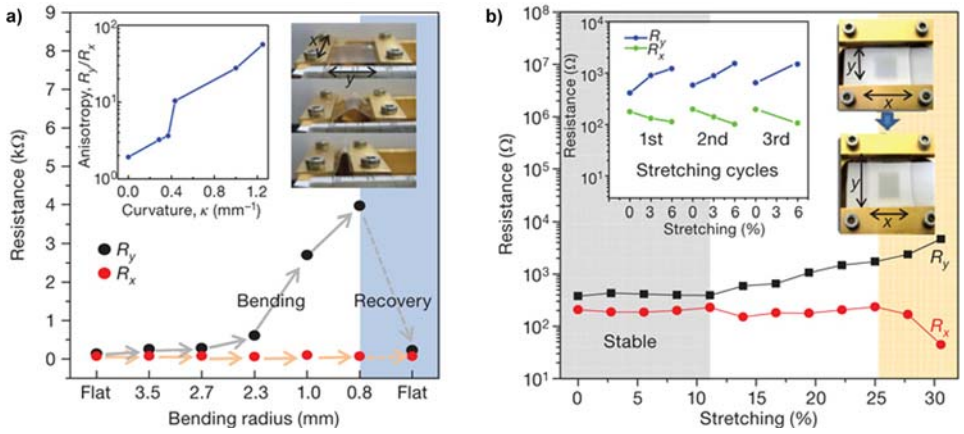

Figure 4. a) Variation in resistance of a graphene film transferred to a ~ 0.3 mm thick PDMS/PET substrate for different distances between holding stages (that is, for different bending radii). The left inset shows the anisotropy in four-probe resistance, measured as the ratio, R_y/R_x, of the resistances parallel and perpendicular to the bending direction, y. The right inset shows the bending process. b) Resistance of a graphene film transferred to a PDMS substrate isotropically stretched by ~12%. The left inset shows the case in which the graphene film is transferred to an unstretched PDMS substrate. The right inset shows the movement of holding stages and the consequent change in shape of the graphene film. Reprinted with permission from Ref. 61. Copyright 2009 Right Managed by Nature Publishing Group.

Kim *et al.* evaluated the foldability of the graphene films, transferred to a polyethylene terephthalate (PET) substrate (thickness, 100 μm) coated with a thin PDMS layer (thickness, 200 μm), by measuring resistance as a function of bending radious [61]. The resistances show little variation up to the bending radius of 2.3 mm (approximate tensile strain of 6.5%) and are perfectly recovered after unbending, (Figure 4). Notably, the original resistance can be restored even for the bending radius of 0.8 mm (approximate tensile strain of 18.7 %), exhibiting extreme mechanical stability.

Many types of electronics could fi nd their way into bendable devices, such as displays, data storage, sensors, [62] solar cells, wearable nanogenerators, and energy storage. Printable devices utilizing graphene-based conductive inks offer a relatively inexpensive and scalable approach to fabricating flexible electronics [63].

1.1.3.2. Transistor

FET is one of the potential applications of graphene. Graphene is unique as a channel material, because unlike other semiconductors, graphene does not require impurity doping to conduct electricity. In particular, graphene presents the phenomenon of self-doping [64]. Self-doping refers to the electric field effect in graphene, which allows the charge carrier type and concentration to be controlled with an outside electric field, or rather gate voltage. Graphene-based FET devices with a single back gate have been investigated, and experimental values of the field-effect mobility of graphene are one order of magnitude higher than that of silicon (Si) [65,66].

Organic field-effect transistors (OFET) with patterned single graphene sheet as source and drain electrodes were prepared using microcontact printing (μCP) [67]. A single graphene sheet was transferred to various substrates in a pattern defined by the geometry of the PDMS stamp. With single crystalline rubrene as an active channel, the devices exhibited excellent p-type characteristics. The highest mobility of transferred rubrene transistor was of 10.3 $cm^2 Vs^{-1}$ with approximately 10^7 of on/off ratio**.** It could be explained that the low Schottky barrier between single graphene layer and rubrene crystal led to excellent output curves showing up to 100 μA at a gate voltage of –20 V.

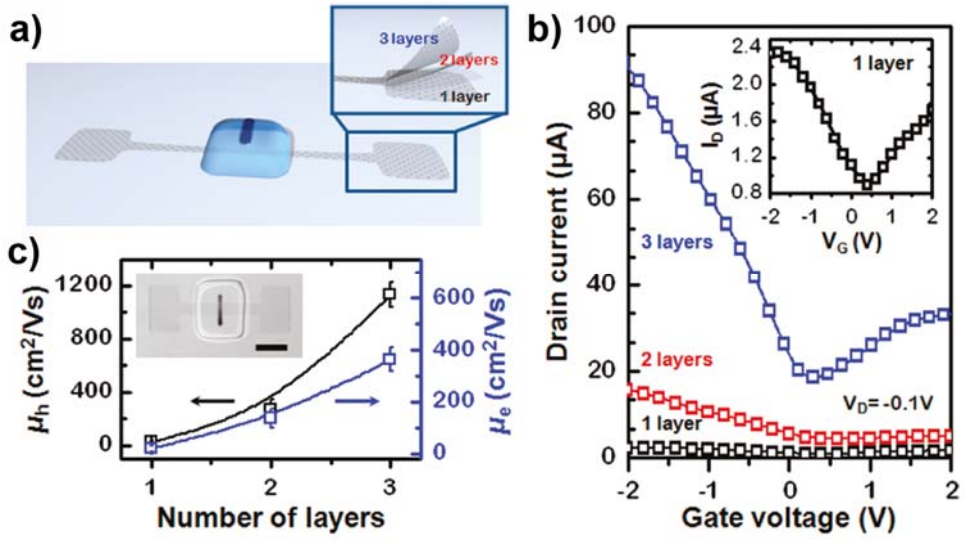

Figure 5. Schematic illustration and electrical characteristics of high-performance, transparent, stretchable graphene FETs on a PDMS rubber substrate. a) Schematic diagrams of mono-, bi-, and tri-layer graphene FETs. b) Transfer characteristics of graphene FETs as a function of the number of graphene layers. c) Hole and electron mobilities of graphene FETs as a function of the number of graphene layers. The inset shows the microscopy image of tri-layer graphene FETs on PDMS (scale bar, 300 μm). Reprinted with permission from Ref. 68. Copyright 2011 American Chemical Society.

Recently, Ahn *et al.* reported a promising route to the fabrication of an all-graphene-based FET array on a stretchable rubber substrate using a low-temperature printing process (Figure 5) [68]. All device components, including channel region and S/D electrodes, were transferred onto a substrate and then the gate insulator and gate electrode were printed in a manner that avoids the need for high-temperature processes. Notably, all-graphene-based transistors were fabricated on rubber substrates without traditional metal electrodes. All the devices were operated within a low voltage region (2 V) with a high on-current. The ultrahigh capacitance of the ion gel gate dielectric yielded the low-voltage and high-current operation. The specific capacitance of the ion gel was measured to be 5.17 μF cm^{-2} at 10 Hz, much larger than typical values for 300 nm thick SiO_2 dielectrics (10.8 $nFcm^{-2}$). The resulting monolithic devices displayed several advantages such as good mechanical stretchability, optical transmittance, simple device design, and improved contact at the channel-to-S/D interface.

1.1.3.3. Chem/Bio sensor

Many kinds of sensors using various nanomaterials have been described for both chemical and biological applications. Up to date, considerable attention has been directed towards the development of miniaturized, reliable, and highly sensitive sensors. Discovery of graphene has opened new area that promises ultra-sensitive and ultra-fast chem/bio sensors due to its conductivity variation as a function of extent of surface adsorption, large specific surface area, and low Johnson noise [69–71]. The sensing mechanism of graphene-based chem/bio sensors is based on the charge transfer between the adsorbed molecules and graphene sheets. As molecules adsorb to graphene surface, the location of adsorption experiences a charge transfer with graphene as a donor or acceptor, thus changing the Fermi level, carrier density, and electrical resistance of graphene. While this phenomenon occurs in other materials, graphene is superior due to its high electrical conductivity and low noise which makes this change in resistance detectable. Owing to these characteristics, various graphene-based sensors have been developed for both chemical and biological uses.

For example, a rugged and flexible graphene-based sensor was fabricated using IJP technique, followed by patterning of rGO onto flexible PET substrate (Figure 6) [72]. When inkjet-printed rGO/PET films are exposed to electron-

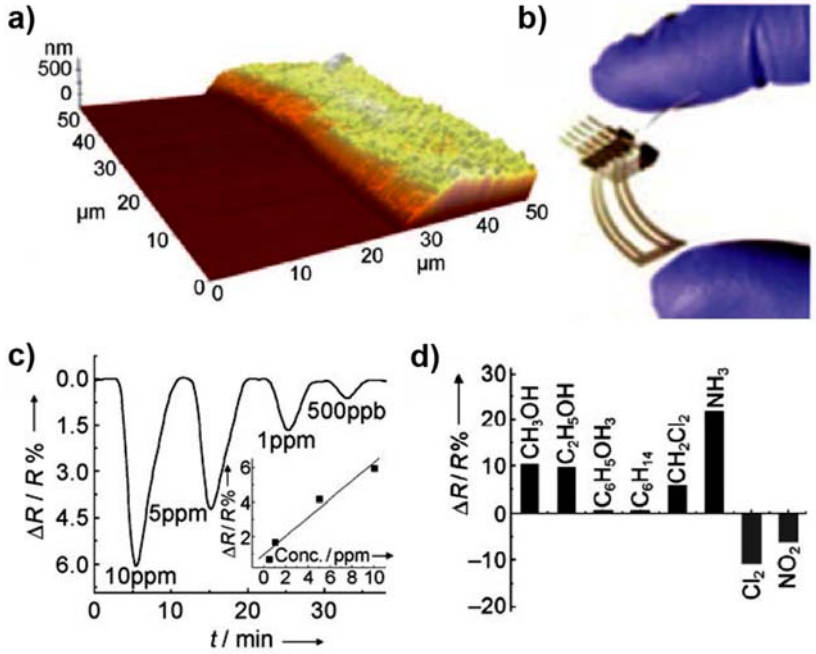

Figure 6. a) AFM image of rGO film obtained by reduction of the film in with ascorbic acid. b) digital image of inkjet-printed rGO/PET four-probe sensor. Vapor sensing by inkjet-printed rGO/PET obtained by ascorbic acid reduction of dispersed graphene oxide. c) Plot for resistance versus time when the film was exposed to a Cl_2 vapor. Inset: Plot of resistance versus vapor concentration. d) Selectivity plot: sensor exposed to saturated organic vapors, NH_3 (100 ppm), NO_2 (100 ppm), and Cl_2 (100 ppm). Reproduced with permission from Ref. 72. Copyright 2010 Wiley-VCH Verlag GmbH & Co. KGaA.

withdrawing vapors, the conductivity increases drastically. The sensing performance of the rGO/PET sensor is attributed to the effective adsorption of NO_2 vapors on the rGO surface. In general, the NO_2 is a strong oxidizer with electron-withdrawing ability. Accordingly, electron transfer from rGO surface to adsorbed NO_2 vapors leads to enriched hole concentration and enhanced electrical conduction in the rGO/PET sensor. Consequently, it can be considered that the rGO/PET sensors can reversibly and selectively detect the general class of electron-withdrawing vapors such as NO_2, Cl_2, etc.

In particular, the micropatterned graphene sheets with proteins are relevant to bioscience applications such as biomolecular sensors, single-cell sensors, and tissue engineering. Curtis *et al.* demonstrated a general strategy for the noncovalent chemical modification of epitaxial graphene for protein immobilization and micropatterning [73]. The chemical modification of graphene sheets for protein crosslinking was performed using bifunctional molecule 1-pyrenebutanoic acid succinimidyl ester (PYR-NHS). The aromatic pyrenyl group in PYR-NHS interacts strongly with the basal plane of graphene *via* π stacking.

1.1.3.4. Supercapacitor

Supercapacitors (also called electrochemical capacitors and ultracapacitors) based on carbon materials have some advantages such as high capacitive energy density and low material cost [74,75]. In particular, graphene possess a high electrical conductivity, high surface area, and outstanding mechanical properties comparable with or even better than CNTs. The specific surface area of a single graphene sheet is 2630 $m^2 g^{-1}$, larger than that of activated carbon and carbon nanotubes. These superior characteristics make graphene a most promising material for supercapacitors [76–78]. In addition, its mechanical strength and flexibility are attractive as conformal electrode materials particularly for flexible supercapacitors. From this view point, graphene has been applied to flexible supercapacitors.

A facile fabrication of graphene-based supercapacitor was developed using direct laser writing of micro-supercapacitors on hydrated GO films [79]. This technique provides the patterning of GO surface into rGO–GO–rGO structures in various geometries with micrometer resolution. Both in-plane and conventional sandwich electrodes with reduced graphite oxide were also patterned (Figure 7). The as-prepared laser-patterned devices (rGO–GO–rGO) demonstrated the excellent electrochemical performance without the use of an external electrolyte. The substantial amounts of trapped water in the

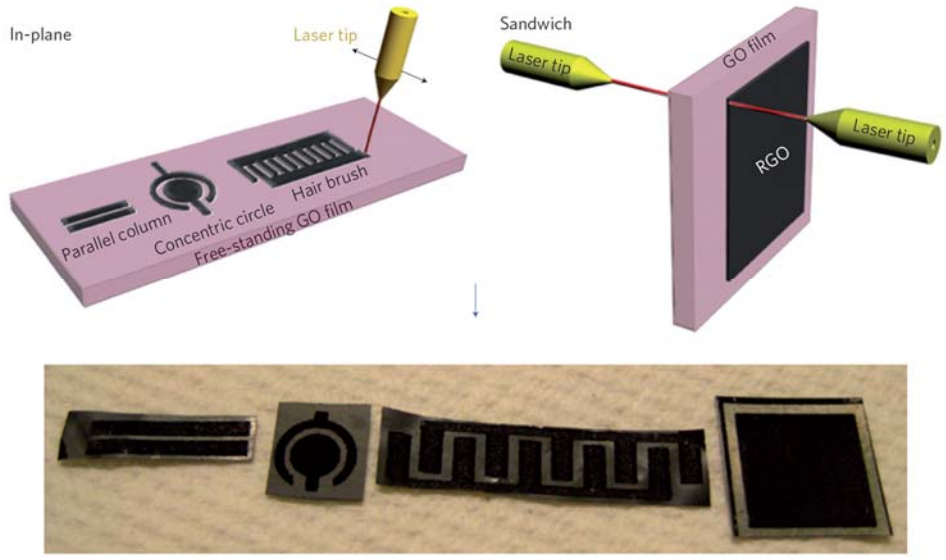

Figure 7. Schematics of CO_2 laser-patterning of free-standing hydrated GO films to fabricate rGO–GO–rGO devices with in-plane and sandwich geometries. The black contrast in the top schematics corresponds to rGO, and the light contrast to unmodified hydrated GO. For in-plane devices, three different geometries were used, and the concentric circular pattern gives the highest capacitance density. The bottom row shows photographs of patterned films. Reprinted with permission from Ref. 79. Copyright 2011 Right Managed by Nature Publishing Group.

graphite oxide made it simultaneously a good ionic conductor and an electrical insulator. It played the role in an electrolyte and an electrode separator with ion transport characteristics similar to that observed for Nafion membranes. As a result, the resulting micro-supercapacitor devices exhibited good cyclic stability, and energy storage capacities comparable to existing thin-film supercapacitors.

A very interesting route to graphene-based electrode has been proposed by directly patterning the graphite on cellulose paper [80]. The shear peeling method was introduced in order to increase the graphite surface area for supercapacitor application. The rough surface structure of paper enabled the exfoliation and adhesion of the graphitic materials. It formed continuous conducting paths on the surface, and provided significant adsorption area for double layer formation. As a result, the patterning of graphite on paper produced multilayer graphene with a large portion of edge structures. The as-fabricated paper supercapacitor demonstrated stable long cycling performance with 90 % capacity retention after 15,000 cycles and a high areal capacitance of 2.3 mF cm^{-2}. In addition, the solvent-free deposition technique represented a low cost, environmentally friendly, highly scalable and versatile fabrication method for integrated paper-based energy devices.

1.2. Objectives and Outline of the Study

1.2.1. Objectives

In the preceding section, the importance of graphene nanomaterials was introduced from the viewpoint of academic research and practical applications. The aim of this dissertation is to present two different synthetic methodologies to fabricate shape-controlled graphene sheets in the viewpoint of 'top-down' and 'bottom-up' approach. Furthermore, the formation mechanism of the graphene sheets is systematically investigated, and their application fields are also explored, including transparent electrode, dipole antenna, acoustic actuator, and electo-responsive materials

1.2.2. Outline

This dissertation involves the following subtopics:

I. 'Top-down' Approach for Fabricating Uniform Graphene Sheets with Disc Shape
   1. Preparation of graphitized carbon nanofibers
   2. Transversal cutting of graphitized carbon nanofibers
   3. Mechanical reduction of oxidized graphene sheets

II. 'Bottom-up' Approach for Fabricating Single Layer Graphene Sheets based on a Layer-by-Layer Self-assembly

1. Preparation of poly(allylamine)/poly(styrenesulfonate) (PAA/PSS) multi-layer using layer-by-layer self-assembly
2. Carbonization of PSS/PAA multi-layer and oxidation/reduction of graphene sheets

III. Applications

1. Foldable graphene electrode using ink-jet printing method
2. Graphene patterning *via* ink-jet printing method and their application to wideband dipole-antenna
3. Flexible & transparent graphene electrode as an acoustic actuator using inkjet printing
4. Electrorheological properties of graphene suspensions with improved sedimentation stability

A detailed outline of the study is as follows:

1. As a 'top-down approach', the graphene discs with well-defined shape are successfully fabricated using a simple oxidation and exfoliation process of high-crystalline carbon nanofibers (CNFs). To control the shapes of graphene discs, two different types of CNFs (platelet and herringbone type) are used as starting materials. The CNFs are formed by the perpendicular stacking of graphene discs, resultant in free edges on the external surface

and readily access to interlay spaces. Interestingly, the diameter and shape of the graphene discs can be controlled by selectively designing the morphology of starting materials and optimizing the cutting method. In addition, a mechanical reduction method for oxidized graphene discs is also proposed in order to combine the high recovery of π-conjugated electronic structure with the solution processability of graphene discs. The reduced graphene discs can be formed without any additives such as reducing agent and are highly dispersed in different solvents with high content of graphene discs.

2. As a 'bottom-up approach', graphene sheets are formed using layer-by-layer (LbL) self-assembly approach with a metallic dopant. The LbL approach is used to form poly(allylamine)(PAA)/poly(styrenesulfonate) (PSS) multilayer on a quartz substrate. During the carbonization process, the PSS layers can be transformed into graphene sheets due to its inherent aromatic and highly ordered structure. PAA layers served to protect the structural layers as well as prevent the agglomeration of graphene sheets. This novel strategy offers great possibility for fabricating various graphene-based nanomaterials with rational nanostructure design.
3. The inkjet printing has attracted a great deal of interest because of the simplified process through the non-contact, additive patterning and mask

less approach. Furthermore, it is also capable of conducting materials to be patterned precisely at desired positions without the loss of printing materials. Importantly, the hydrophilic property of GO as a conductive ink made it possible to overcome the above mentioned limitations related to conductive ink preparation. The patterned graphene sheets using this new technique had the sustained electrical conductivity, and the potential to make a gradation pattern offered attractive opportunity for controlling the sheet resistance at designed positions. In this study, as prepared patterned graphene sheets showed opto-electronic properties, and their application fields are also explored, including transparent electrode, dipole antenna, and acoustic actuator.

4. The ability to control rheological property is important in many technological applications. In particular, electrorheological (ER) fluids have received much attention due to their unique rheological features. The ER fluid is smart and intelligent material having the ability to change their rheological property under an applied electric field. In this study, a simple and effective dispersion approach is presented to investigate the electro-responsive characteristics of oxidized graphene sheets-based ER fluids assisted by solvent exchange method. The solvent exchanged oxidized graphene sheets exhibited consistently higher ER efficiency than that of

mechanically grinded oxidized graphene sheets. Furthermore, the ER fluids prepared by solvent exchange method represented excellent anti-sedimentation properties, and provided the feasible candidate for their practical or industrial applications.

2. EXPERIMENTAL DETAILS

2.1. 'Top-down' Approach for Fabricating Uniform Graphene Sheets with Disc Shape

2.1.1. Preparation of graphitized carbon nanofibers

Platelet carbon nanofibers (CNFs) were synthesized from carbon monoxide and hydrogen (160/40 (vol/vol, mL/min)) over a Fe catalyst at 600 ^{o}C. The herringbone CNFs with diameters ranging from 150 to 200 nm were prepared from carbon monoxide over Fe:Mn (3:7) alloy catalyst at 560 ^{o}C. The two different types of CNFs were purified in the 10 wt% HCl until the metal content was less than 0.2 wt%. These purified CNFs were further heat-treated at 2800 ^{o}C for 10 min to obtain graphitized CNFs.

2.1.2. Transversal cutting of graphitized carbon nanofibers

The graphitized CNFs were oxidized according to the Hummer's method. In a typical process, 1 g of graphitized CNFs were suspended in 100 mL of concentrated sulphuric acid with the assistant of 30 min ultrasonication (ultrasonic bath cleaner USK-4R). Then, 1–7 g potassium permanganate ($KMnO_4$) was slowly added into the solution. The reaction mixture was stirred at 0 ^{o}C for 30 min and then heated to 40 ^{o}C for an additional 1 h. After that, 100 mL of distilled water was added slowly into the solution within the ice

water bath. While the temperature cool down to room temperature (about 2 h), 400 mL of distilled water and 20 mL of 30 wt% H_2O_2 was added. The obtained solution was separated using centrifuge (Hitachi, Himac CR-GII) at the speed of 4800 rpm. And the remained slurry was washed with 3 M HCl for 3 times and acetone for 5 times using the centrifuge. The collected samples were dried using freeze-drying equipment (EVELA, FD-1000). After oxidation/washing process, the oxidized graphitized CNFs were exfoliated under ultrasonic assistance for 1 h. The concentration of oxidized graphitized CNFs solution is 2.0 g L^{-1}.

2.1.3. Mechanical reduction of oxidized graphene sheets

The reduction was dependent upon a wet milling technology using a nano dispersion machine (T.K.FILMICS 56, PRIMIX) without any assistant of reduced agent. About 70 mL of oxidized graphene discs solution (2.0 g L^{-1}) was put into the chamber with a Filmics mixer. The motor was set as 200 V, 3.7 kW and mixing section rpm was *ca.* 18400 rpm. The temperature of the solution was controlled by cooling agents to maintain the water temperature around 100 ^{o}C. The mixing time was changed from 10 min to 50 min.

X-ray diffraction was performed with Rigaku X-ray diffractometer with CuK target. High-resolution solid-state ^{13}C NMR experiments were carried out

on a JEOL ECA400 spectrometer operated at 100.53 MHz using the single pulse decoupling method. The elemental composition was obtained from the CHN elemental analysis (Yanako MT2 CHN Corder, Japan). X-ray photoelectron spectroscopy (XPS) spectra were obtained using a JPS-9000MC (JEOL) instrument equipped with an Mg K X-ray source. Field emission (FE) tests were performed in a vacuum chamber at a pressure of 7×10^{-8} Pa. Prior to elemental analysis and XPS measurement, samples were dried for 2 h at 120 ^{o}C. The UV-vis adsorption spectra were recorded under a Shimadzu UV-3600 spectrophotometer. The morphology of sample was observed under a field-emission scanning electron microscope (JEOL-6300F, JEOL, Japan), a high resolution transmission electron microscope (JEM-2010F, JEOL, Japan) and atomic force microscope (Nanoscope IIIa, Digital Instrument, USA). AFM topography analysis was carried out with a Digital Instruments Nanoscope IIIA from Veeco Systems in tapping mode using silicon tips with a resonance frequency of 320 kHz. Raman spectra were recorded using a Bruker FRA 106/S FT-Raman spectrometer with 1064 nm laser excitation (a spectral resolution of 1 cm^{-1}). For Raman spectroscopy analysis, the samples were dried in a vacuum oven for 12 h at room temperature and were examined under ambient conditions without any pre-treatment.

2.2. 'Bottom-up' Approach for Fabricating Single Layer Graphene Sheets based on a Layer-by-Layer Self-assembly

2.2.1. Preparation of poly(allylamine)/poly(styrenesulfonate) (PAA/PSS) multi-layer using layer-by-layer self-assembly

Anionic poly(styrenesulfonate); PSS (M_w = 70,000) and cationic polyallylamine; PAA (M_w = 70,000) were used as received from Aldrich. Iron (III) chloride (Aldrich, reagent grade, 97%) as a metallic dopant was used without further purification. Quartz substrate (3.0 cm × 3.0 cm, thickness of 1000 μm) was purchased from JMC Glass, manufactured in Korea.

Quartz substrate was cleaned by ultrasonication with a hot mixture of H_2SO_4/H_2O_2 (7:3) for 3 h. The quartz substrate was heated in a mixture of $H_2O/H_2O_2/NH_3$ (5:1:1) at 80 ˚C for 1 h, and then subsequently dried by N_2 gas purging. After that, the substrate is negatively charged and used for the polyelectrolyte deposition starting with the cationic PAA. The concentration of PAA and PSS solutions used for all the in this experiments was 1 mg mL^{-1}. The deposition steps were carried out as follows: At first step, aqueous $FeCl_3$ solution (7 M) was added into the PSS solution and allowed to equilibrate. The volume ratios of aqueous $FeCl_3$ solution to PSS solution was 2.0×10^{-2}. Afterwards, a few drops of polyelectrolyte solution were placed on the substrate and then the substrate was rotated with a spinner at 3000 rpm for 45

sec. After the deposition of each polyelectrolyte layer, the substrates were thoroughly rinsed with plenty of deionized water. The spinning time and the speed for the washing step were identical to those for the layer deposition.

2.2.2. Carbonization of PSS/PAA multi-layer and oxidation/ reduction of graphene sheets

The prepared PAA/PSS multilayer on a quartz substrate was placed in a furnace under N_2 atmosphere. The sample was heated to 1000 ˚C at a heating rate of 3 ˚C min^{-1} held at 1000 ˚C for 5 h, and then cooled to room temperature. As-carbonized PSS/PAA multi-layer was exfoliated in water by sonication for 120 min (Branson 1510E-MT bath sonicator) and followed by centrifugation at 500 rpm for 60 min to achieve exfoliated nanosheet of GO. A dilute GO suspension was subsequently reduced to graphene suspension in the presence of hydrazine solution and ammonium hydroxide solution.

The PSS/PAA multi-layer film was acquired using a PWM32 spinner (Headway Research, Inc.). Photographs of transmission electron microscopy (TEM) were obtained with a JEOL EM-2000 EX II microscope. In the sample preparation, the graphene nanosheets dispersed in water were cast onto copper grid. AFM topography analysis was carried out with a Digital Instruments Nanoscope IIIA from Veeco Systems in tapping mode using silicon tips with a resonance frequency of 320 kHz. Raman spectra were recorded using a Bruker FRA 106/S FT-Raman spectrometer with 1064 nm laser excitation (a spectral resolution of 1 cm^{-1}). The peak positions obtained from the Raman spectrometer have a margin of error of ±0.05 cm^{-1}. For Raman spectroscopy

analysis, the as-prepared graphene nanosheets were dried in a vacuum oven for 12 h at room temperature and were examined under ambient conditions without any pre-treatment.

2.3. Applications

2.3.1. Foldable graphene electrode using ink-jet printing method

A uniform flexible graphene film was obtained by vacuum filtration of this dilute graphene suspension using an anodic aluminum oxide (AAO) membrane (Whatman International Ltd.) and wet-transferred to a PET film. The film thickness was controlled by the volume of suspension filtered and hence the deposited graphene mass.

The graphene nanosheet films were measured for optical transparency with Ultraviolet-visible (UV-vis) sepectroscopy. The UV-vis spectra were taken with a Perkin-Elmer Lamda 20 spectrometer at a resolution of 1 nm. Current-voltage (*I–V*) measurements were conducted using a Wonatech WBCS 3000 potentiostat at room temperature. The samples were coated onto the interdigitated microelectrodes, and the data were collected at a scan rate of 50 mV s^{-1}. The electrical conductivity was measured by the four-probe method using a Keithley 2400 sourcemeter at room temperature.

Electrically conductive wire (100 % graphene nanosheets, thickness of 300 nm, width of 5 mm) was patterned on a polyimide film. The pattern designed on computer software (MS PowerPoint) is inkjet printed repeatedly for 30 passes. The inkjet printing of graphene suspension was carried out as follows: First, commercialized office desktop inkjet printer (Canon Pixima IP1300) was purchased and modified for this work. Ink cartridge was disassembled and

washed several times by ethanol and distilled water after removing all inks. Subsequently, the ink cartridge was dried in a vacuum oven at room temperature. Then, graphene nanosheet in distilled water (10 mL) was injected into the cartridge as an alternative ink. The concentration of water-dispersed graphene suspension was 0.05 wt%.

2.3.2. Graphene patterning *via* ink-jet printing method and their application to wideband dipole-antenna

The graphite flakes used in the majority of experiments was purchased from Sigma-Aldrich (Product Number 332461). GO was printed using a commercial office inkjet printer (Canon Pixima IP1300). Poly (ethyleneterephtalate) (PET, 3M) film was used as a substrate for inkjet printing. Aniline monomer (99 %) and ammonium persulfate (APS, 98 %) were obtained from Sigma Aldrich Co. Ltd, and pyrrole monomer (99 %) was obtained from Acros Organics and used without further purification. Hydrochloric acid (HCl, 35 wt% in H_2O) was purchased from Samjun Chem. Co. and used for doping of PANI.

GO was synthesized from natural graphite by a modified Hummers and Offeman method as originally presented by Kovtyukhova and colleagues. Synthesized purified GO suspensions were dispersed in water. Exfoliation of GO was achieved by sonication of the dispersion for 3 h to avoid the nozzle blockage. The obtained brown dispersion was then washed for 5 cycles of centrifugation at 3,000 rpm to remove any unexfoliated graphite oxide.

The ink cartridge (printer head) was disassembled and washed several times by ethanol and distilled water after removing all inks. The exfoliated GO in distilled water was injected into the modified cartridge as an alternative ink.

Subsequently, the completely sealed ink cartridge was placed in the printer body and prepared to use for further experiments.

For patterning of graphene sheets onto the PET film, oxygen plasma treatment was performed in order to modify the surface energies of target substrate (gas flow rate: 20 sccm, power: 100 W, time: 20 s). The complex patterned architectures were designed by computer software in advance (Microsoft PowerPoint 2003). The exfoliated GO solution was printed on the flexible PET film as the designed images using the modified inkjet printer. Subsequently, the printed film was properly cut and located in VDP chamber containing hydrazine and ammonia solution. The graphene sheets patterns were formed immediately at low temperature (90 $^{\circ}$C, 1 h).

For patterning the conduction polymers such as PPy abd PANI, oxidant agent APS 0.15g in distilled water (5 mL) was injected into the modified cartridge as an alternative ink. In the case of PET film, low temperature oxygen plasma treatment (gas flow rate: 20 sccm, power: 100 W, time: 20 s) was also conducted to increase the hydrophilic property of surface. The oxidant APS solution was printed on the PET film as the designed images. Subsequently, the patterned oxidant was properly cut and located in the VDP chamber containing pyrrole and aniline monomer (1mL). In case of patterned PANI, dilute hydrochloric acid solution (1 mL of HCl solution in 10 mL distilled water) was

also added in the VDP chamber. Immediately, the patterned PPy and emeraldine salt form of PANI were fabricated by thermal treatment (90°C).

A 300 nm thick, 300 × 30 mm rectangle GO film on glossy photo paper treated with oxygen plasma was obtained by inkjet printing repeatedly for 30 times. The rectangle GO/PET section was cut using scissors and placed at 90 °C VDP chamber with hydrazine and ammonia solution for 1 h. Patterned graphene sheets of dipole antenna were connected by silver paste to the power supply source.

TEM image was taken with a JEOL 6700F and the XPS spectra were recorded using Kratos Model AXIS-HS system. The AFM topography of the GO solution deposited on Si wafer was obtained by a Digital Instrument Nanoscope IIIA from veeco systems in tapping mode using silicon tips with a resonance frequency of of 320 KHz. Optical micrographs were taken using a Leica DM2500 P and the plasma reactor was of the parallel electrode type with a 13.56 MHz radio-frequency generator. The viscosity was measured by rheometer (AR 2000 Advanced Rheometer, TA Instruments) and the surface energy was calculated by Owens-Wandt equation after measuring the contact angle of distilled water droplet on the film surfaces. The measurement of electrical resistances was performed with a Keithley 2400 sourcemeter at 25 °C by a four-probe method. The sheet resistance was measured at 10 different

locations of graphene sheets based films and calculated as an average value. For the RFID antenna characteristics, E5071B ENA RF Network Analyzer of Agilent Technologies was carried out (300 kHz to 8.5 GHz). Impedance was plotted on the smith chart by first normalizing to the characteristic impedance of the system (50 ohms).

2.3.3. Flexible & transparent graphene electrode as an acoustic actuator using inkjet printing

The graphite flakes used in the majority of experiments were purchased from Sigma-Aldrich (Product Number 332461). GO was printed using a commercial office inkjet printer (Canon Pixima IP1300). The printer was equipped with a piezo-based print-head (dispenser system) with an inner diameter of 50 μm. The driving voltage applied to the piezo was 24 V and the dot spacing, which was the center-to-center distance between two adjacent droplets, was *ca.* 70 μm. Poly(vinylidene fluoride) (PVDF, Fils Co., Ltd) with 60 μm thickness was used as a substrate for inkjet printing.

GO sheets were synthesized from natural graphite by a modified Hummers and Offeman method as presented originally by Kovtyukhova and colleagues. Synthesized purified GO suspensions were exfoliated in water by sonication for 1.5 h to avoid the nozzle blockage. The obtained brown dispersion was then washed for 5 cycles of centrifugation at 3,000 rpm to remove any unexfoliated GO sheets.

The ink cartridge (printer head) was disassembled and washed several times by ethanol and distilled water after removing all inks. The exfoliated GO in distilled water (0.1 wt%) was injected into the modified cartridge as an

alternative ink. Subsequently, the completely sealed ink cartridge was placed in the printer body and prepared to use for further experiments.

For fabricating of graphene onto the PVDF film, low-temperature oxygen plasma treatment was performed in order to modify the surface energy of PVDF substrate (gas flow rate: 20 sccm, power: 100 W, time: 120 s at 5 $^{\circ}$C). The 10 × 10 cm rectangular architectures were designed by computer software in advance (Microsoft PowerPoint 2003), and GO ink printed on both sides of the PVDF film by inkjet printing repeatedly for several times. Subsequently, the printed GO film was properly cut and located in 90 $^{\circ}$C VDP chamber containing hydrazine and ammonia solution for 30 min under vacuum. The graphene were immediately formed at low temperature. Then, the graphene electrodes of acoustic actuator were connected by Cu tape to the amplifier and sound source, which was used to reduce the electrode contact resistance. The transducers were excited to produce sound by a 50 V_{rms} white noise signal. The range of frequency response was from 40 Hz to 20 kHz (audible frequency range) and measured at 1 m distance from the film along the centerline axis. As a commercial thin film speaker, PEDOT:PSS-based acoustic actuator had the 85 % transmittance and 10 × 10 cm rectangular size. For ANC application, a soft substrate (3M VHB4910 acrylic form tape, Young's modulus = 105 kPa)

was attached to graphene-based PVDF thin film in order to make an ANC actuator.

TEM image was taken with a JEOL 6700F and the XPS spectra was recorded using Kratos Model AXIS-HS system. The AFM topography was obtained by a Digital Instrument Nanoscope IIIA from veeco systems in tapping mode using silicon tips with a resonance frequency of 320 KHz. Plasma reactor was the parallel electrode type with a 13.56 MHz radio-frequency generator. The viscosity was measured by rheometer (AR 2000 Advanced Rheometer, TA Instruments) and the surface energy was calculated by Owens-Wandt equation after measuring the contact angle of distilled water droplet on the film surfaces. The measurement of electrical resistances was obtained with a Keithley 2400 sourcemeter at 25 °C by a four-probe method. The surface sheet resistance was measured at 5 different locations of graphene film and calculated as an average value. For the acoustic actuator characteristics, Brtiel and Kjaer 2012 audio analyzer was carried out (40 kHz to 20 kHz).

2.3.4. Electrorheological properties of graphene suspensions with improved sedimentation stability

Graphite (flake, <20 μm, synthetic) was purchased from Sigma–Aldrich. Other reagents including $KMnO_4$, HCl, H_2SO_4, H_2O_2 and ethanol were also obtained from Aldrich Chemical Co. All regents were used as received. Distilled water was used in all experimental processes. For electrorheological (ER) fluid application, silicone oil (Aldrich, poly(methylphenylsiloxane), viscosity = 100 cSt) was used as a dispersing medium.

GO was synthesized from graphite using a modified Hummers method. Typically, graphite (1.0 g) was added to 70 mL of H_2SO_4 in an ice bath, which was followed by the addition of $KMnO_4$ (3.0 g) and $NaNO_3$ (0.5 g). After stirring for 4 h, 70mL of distilled water was slowly added and maintained at that temperature for 30 min. Subsequently, H_2O_2 solution was added to the solution until the color turned a brilliant brown indicating fully oxidizing state. The as-prepared graphite oxide slurry was exfoliated to generate GO nanosheets by sonication using an ultrasonic generator (42 kHz, 100W, Branson 3510, Branson Cleaning Equipment Co., Shelton, CT, USA) for 3 h. Finally, the mixture was separated by centrifugation, washed repeatedly with 5% HCl and distilled water, and dried in a vacuum oven at 40 ºC for 24 h.

The dried GO was ground into uniform powder using a milling machine (Analytical Mill. A11, IKA Works). The solvent exchanged GO sheets were prepared using the difference of density between silicone oil and ethanol medium. First, 2.0 g of graphite oxide slurry (filter cake) in 20 mL of ethanol was sonicated for 2 h, and centrifuged at 500 rpm for 30 min to remove large particles. The supernatant of graphene in ethanol was decanted and further sonicated for several minutes to give the required homogeneous GO sheets dispersion in ethanol. Second, the 10 mL of GO sheets dispersed in ethanol was poured into 10 mL of silicone oil. The mixture was centrifuged at 10000 rpm for 30 min to settle down into silicone oil phase. After centrifugation, the supernatant was decanted and further dried. The loosely flocculated GO sheets were redispersed in silicone oil under sonication at room temperature, resulting a homogeneous black suspension. The repeated settling steps yield a stable dispersion of graphene in silicone oil containing up to 5.0 wt%.

The ER properties of the GO-based ER fluids were examined via rheometer (AR 2000 Advanced Rheometer, TA Instruments) with a concentric cylinder conical geometry of 15 mm cup radius with a gap distance of 1.00 mm, a high-voltage generator (Trek 677B), and a temperature controller. To start a run, an ER fluid is placed between cup and rotor, and DC voltage is applied. An electric field was applied for 3 min to obtain an equilibrium chain-like or

columnar structure before applying shear. All measurements were made at a room temperature. In this study, the yield stress values for the prepared ER fluids were mainly obtained from a flow curve, which was measured by a controlled shear rate (CSR) mode experiment. The stress value of the transition point at which shear viscosity abruptly decreased was regarded as the dynamic yield stress.

3. RESULTS AND DISCUSSION

3.1. 'Top-down' Approach for Fabricating Uniform Graphene Sheets with Disc Shape

3.1.1. Preparation of graphitized carbon nanofibers

The overall synthetic procedure for uniform graphene sheets with discs shape is represented in Figure 8a. Under our experimental conditions, two different types of high-crystalline CNFs (platelet and herringbone type) were employed as a starting material. The platelet CNFs (PCNFs) were prepared by the catalytic pyrolysis of carbon monoxide over iron metal particles at 600 ^{o}C.[24] The PCNFs had diameters of 80–300 nm with a polygonal cross section according to SEM observation, and the PCNFs had very high carbon content with the elemental composition of C (99.0 %), H (0.2 %) and O (0.8 %). XRD pattern revealed that the PCNFs had a high degree of graphitization with the interlayer distance (d_{002}) of ca. 0.336 nm, comparable to those of natural graphite. However, the high resolution TEM image (Figure 8b) displays that the graphitic interlayer is not strictly straight and some dislocation and tortuosity are existent in the local region.

To improve crystalline phase of graphite structure, the pristine PCNFs were further graphitized in argon atmosphere at 2800 ^{o}C. The graphitized PCNFs (GPCNFs) had similar XRD pattern of crystal structure but different

microscopic morphologies compared to their pristine PCNFs. As shown in Figure 8c and 8d, the GPCNFs were constructed by parallel close-packing of nano-sized plate units as illustrated in the model of hexagonal-type plate stacking. Such a plate unit had an average thickness of *ca.* 3 nm consisting of 8–10 graphene discs. This stacking formation of hexagonal-type plate was due to rearrangement and reorganization in the post-graphitization. In addition, it also inherited from the primal embryo in the as-prepared PCNFs as a reflection of the periodical repetition of temporal nucleation and growth of graphene layers [81,82].

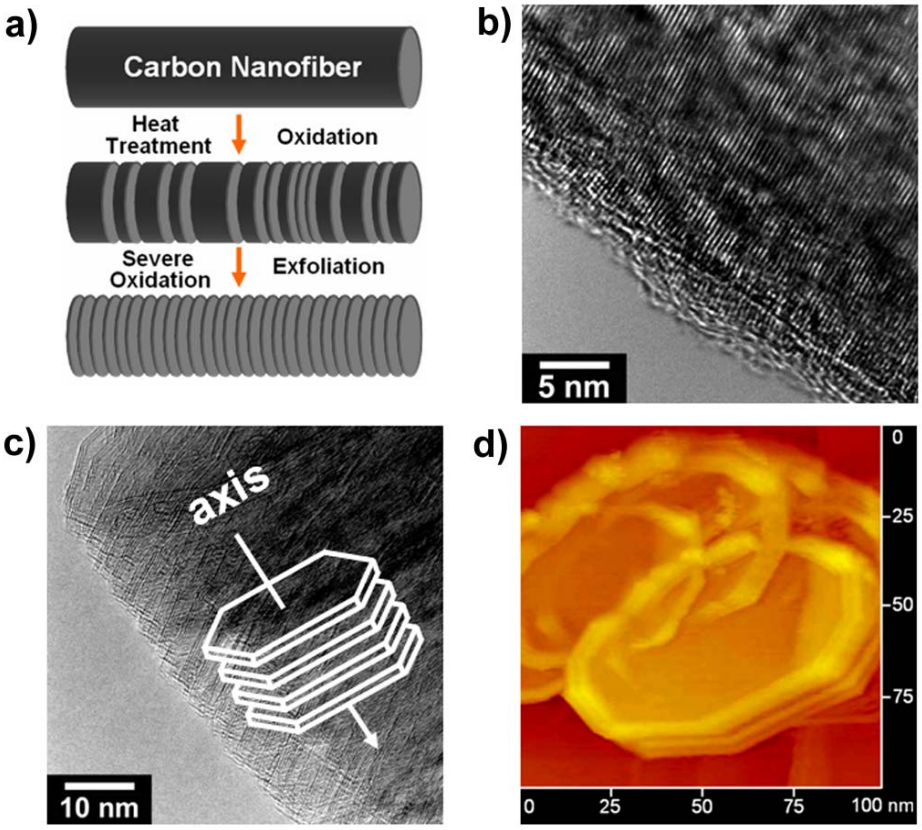

Figure 8. a) Plausible formation procedure of graphene layers with well-defined shape using the platelet carbon nanofibers. b) HR-TEM images of as-prepared PCNFs. c) TEM image of GPCNFs. d) STM images of isolated graphitized CNFs.

3.1.2. Transversal cutting of graphitized carbon nanofibers

In After post-graphitization, the GPCNFs were suspended in concentrated sulphuric acid followed by $KMnO_4$ treatment according to the Hummer's method [83]. Figure 9 demonstrates that the TEM image of oxidized GPCNFs as a function of mass ratio of oxidant to GPCNFs ($KMnO_4$/GPCNF, $R_{K/GP}$). After oxidation process, the oxidized GPCNFs were exfoliated under ultrasonic assistance for 1 h. The oxidized graphene discs were readily exfoliated from the oxidized GPCNFs. It was found that one hour ultrasonic treatment is enough to achieve complete exfoliation of oxidized GPCNFs to the individual oxidized graphene discs. A high degree of exfoliation was observed as the oxidation level increased in the range of 1–6 ($R_{K/GP}$).

In the case of the $R_{K/GP}$ of 1, the GPCNFs formed still integrity even though a lot of kerfs was homogeneously distributed (Figure 9b). When the $R_{K/GP}$ value increases to 2, the oxidized GPCNFs broke into small segments and still contained tens of plate units. These segments could be further splitted into smaller ones up to $R_{K/GP}$ value of 3. Further increasing the $R_{K/GP}$ value to 5, most of plate units were isolated and some oxidized graphene discs were separated from the structure units. Increasing the $R_{K/GP}$ value to 6, high quality and uniform oxidized graphene discs with average thickness of 1.2 nm were obtained. This phenomenon demonstrated that the single-layered oxidized

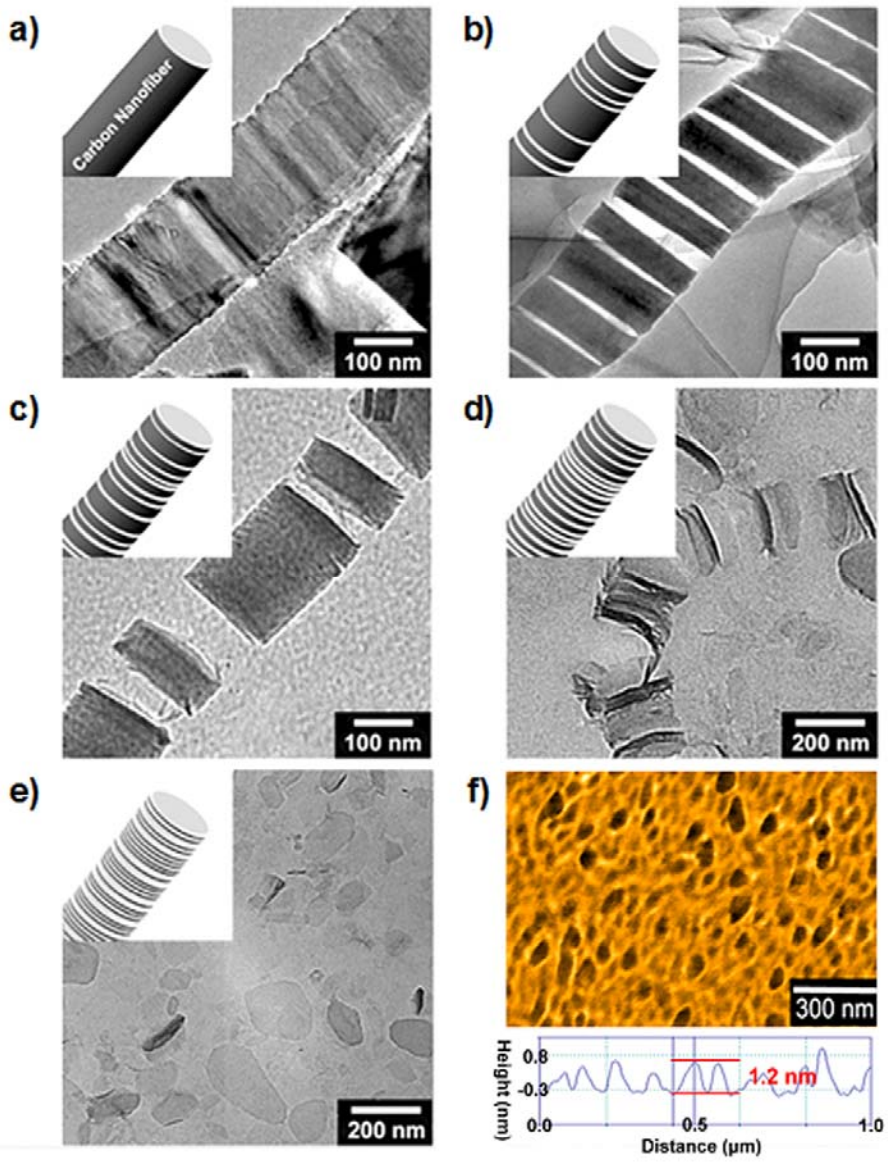

Figure 9. TEM images (a-e) for oxidized GPCNFs as a function of mass ratio of oxidant to GPCNFs: a) pristine GPCNFs, b) $R_{K/GP}$=1, c) $R_{K/GP}$=2, d) $R_{K/GP}$=3, e) $R_{K/GP}$=6 (inset: related schematic illustration), f) AFM image of exfoliated oxidized graphene discs with the mean thickness of 1.2 nm.

graphene discs were successfully exfoliated from the GPCNFs. However, perfectly thin graphene discs could not be obtained up to the $R_{K/GP}$ value of 7–10, due to structural collapse of GPCNFs based on the excessive oxidation.

The structure evolution from GPCNFs to oxidized GPCNFs was investigated with different oxidation levels by XRD analysis (Figure 10). The treated samples at $R_{K/GP}$ value of 1 & 2 had a relatively broad peak at 2 θ values of ~ 26 ^{o} (a d_{002} spacing of 0.34 nm), originated from the graphitic structure. In the case of $R_{K/GP}$ value of 3–6, this peak dramatically diminished but a new shape peak appeared at ~11.7 ^{o} (d-spacing value of 0.76 nm), which was very similar to that of graphitic oxide [84].

The solid state ^{13}C NMR spectra of GPCNFs at $R_{K/GP}$=3–6 (Figure 11) showed C–OH, C–O–C expoxide, conjugated double groups, aromatic entities and carboxylic groups at 60, 70, 105, 130 and 165 ppm, respectively, which might be same as the structure of graphite oxide.[85,86] Judging from these data, it is concluded that the oxidized GPCNFs is generated by oxidation using $KMnO_4$ as a oxidizing agent and contains a wide range of oxygen functional groups, such as hydroxyl and epoxy groups on the basal plane and carboxylic acid groups at the edges, which make the GPCNFs hydrophilic. The oxygen functional groups in the GPNCFs allow dynamic intercalation of water molecules into the GPCNFs. Furthermore, the interlayer distance is also

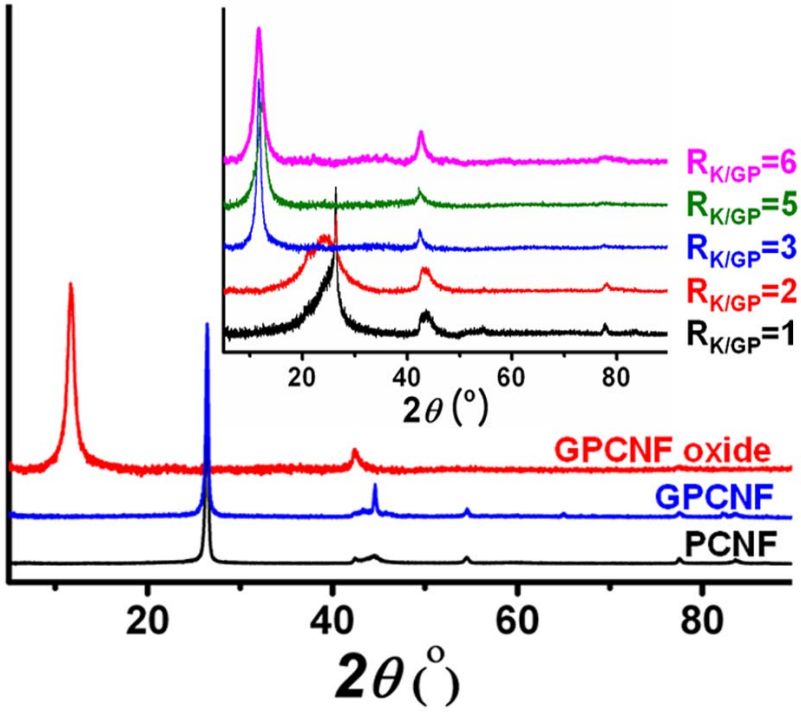

Figure 10. XRD patterns of platelet CNF, graphitized platelet CNFs (GPCNFs), and oxidized GPCNFs (inset: Changes in XRD patterns of GPCNFs as a function of $R_{K/GP}$ value).

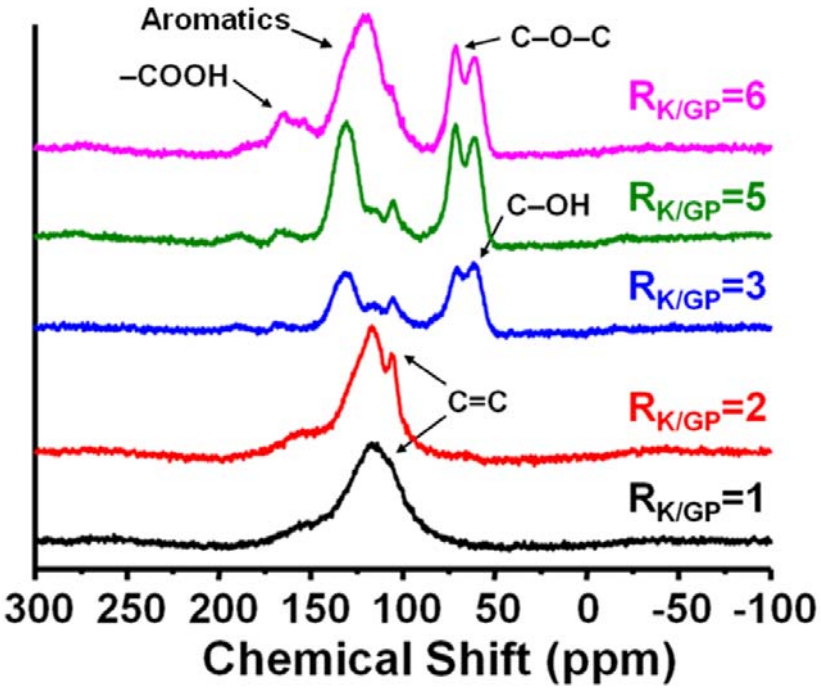

Figure 11. Solid ^{13}C NMR of oxidized GPCNFs with a different $R_{K/GP}$ value.

directly connected to dispersity of aqueous oxidized GPCNFs solution. That means that the water molecules are highly bound to the oxidized graphene discs. Then the dispersity and stability can be enhanced. Consequently, the high $R_{K/GP}$ value ($R_{K/GP} \approx 6$) enable to achieve complete exfoliation and obtain high quality & uniform oxidized graphene discs.

In addition, the GPCNFs with different oxidation levels were analyzed by elemental analysis (EA), XPS, solid ^{13}C NMR. As shown in Table 1, the C : O : H ratio of oxidized GPCNFs varied from 6.00 : 0.50 : 0.56 ($R_{K/GP}$=1) of initial oxidation level to 6.00 : 2.89 : 4.48 of high oxidation level ($R_{K/GP}$=6). From the XPS spectra of oxidized GPCNFs (Figure 12), deconvolution of the C 1s spectra showed five individual component groups that represented graphitic carbon (C_{G1}, 284.4 eV) and carbon present in phenol, alcohol, or ether (C_{G2}, 286.1 ± 0.3 eV), carbonyl or quinine groups (C_{G3}, 287.3 ± 0.3 eV), carboxyl, lactone, or ester groups (C_{G4}, 289.1 eV) and carbonate groups (C_{G5}, 290.6 eV). Deconvolution of the O 1s spectra yielded four peaks; the peak at 531.0–531.3 eV (O_{G1}) corresponded to carbonyl oxygen atoms; the peak at 532.1–532.5 eV (O_{G2}) corresponded to carbonyl oxygen atoms in esters, amides, and anhydrides as well as oxygen atoms in hydroxyls or ethers; the peak at 533.1–533.5 eV (O_{G3}) corresponded to ether oxygen atoms in esters and anhydrides; and the peak at 534.1–534.4 eV (O_{G4}) corresponded to oxygen

Table 1. Elemental and physical parameter of oxidized GPCNFs.

Samples	$R_{K/GP}$ [a]	C:O:H ratio [b]	$D_{(002)}$ spacing [c]
GPCNFs	-	6: 0: 0.001	0.34 nm
Oxidized GPCNFs-1	1	6: 0.50: 0.56	0.34 nm
Oxidized GPCNFs-2	2	6: 0.91: 1.82	0.34 nm
Oxidized GPCNFs-3	3	6: 1.97: 3.10	0.73 nm
Oxidized GPCNFs-4	4	6: 2.33: 3.50	0.73 nm
Oxidized GPCNFs-5	5	6: 2.62: 3.95	0.74 nm
Oxidized GPCNFs-6	6	6: 2.89: 4.48	0.76 nm

[a] These values indicate the mass ratio of oxidant to GPCNFs ($KMnO_4$/GPCNF). [b] These values were obtained from CHN analysis. [c] The d-spacing values were calculated by means of Bragg's law.

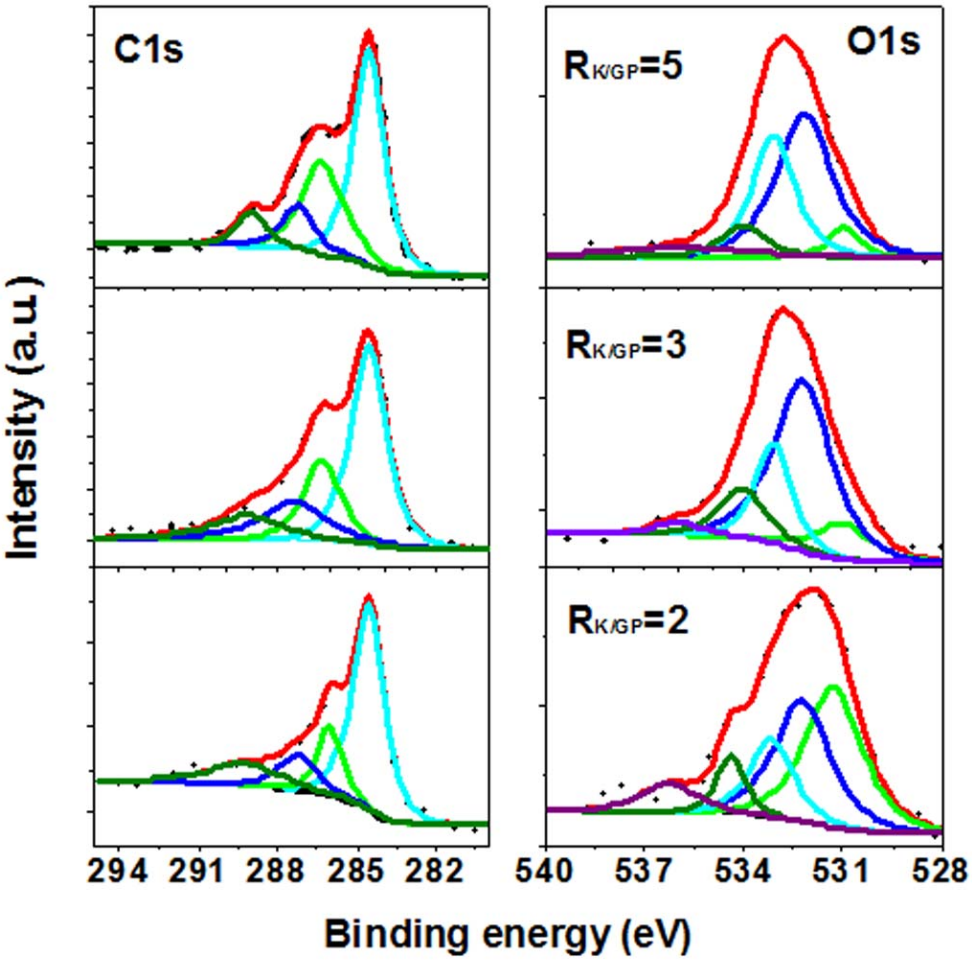

Figure 12. XPS spectra of oxidized GPCNFs with different mass ratios of $R_{K/GP}$ value.

atoms in carboxyl groups. Consequently, the XPS spectra reveal that the oxidized GPCNFs consisted mainly of carbonyl, carboxyl and hydroxyl groups.

Interestingly, the diameter of graphene discs was in accordance with that of the PCNFs, which could be controlled by changing the chemical vapor decomposition conditions of CNF growth process. The PCNFs with small diameter of 30–50 nm could be prepared from carbon monoxide over a Fe : Co : Ni : MgO (7.0 : 2.0 : 0.5 : 0.5 in weight ratio) catalyst at 600 ^{o}C, and allowing the fabrication of graphene discs with small diameter (Figure 13).

Except the PCNFs, the herringbone type of CNFs (HCNFs) was also used as a starting material. Figure 14 illustrates the graphitized HCNFs and oxidized graphitized HCNFs with different morphology. The HCNFs with diameters ranging from 150 to 200 nm were prepared from carbon monoxide over Fe : Mn (3 : 7) alloy catalyst at 560 ^{o}C. As a consequence or their high crystallinity and different morphology, the HCNFs also readily oxidized and exfoliated, which cause bow-tie shape of graphene discs (Figure 14b inset). It was noteworthy that the graphene discs with different defined shapes could be obtained by selectively designing the shape of starting materials and optimizing the transversal cutting method.

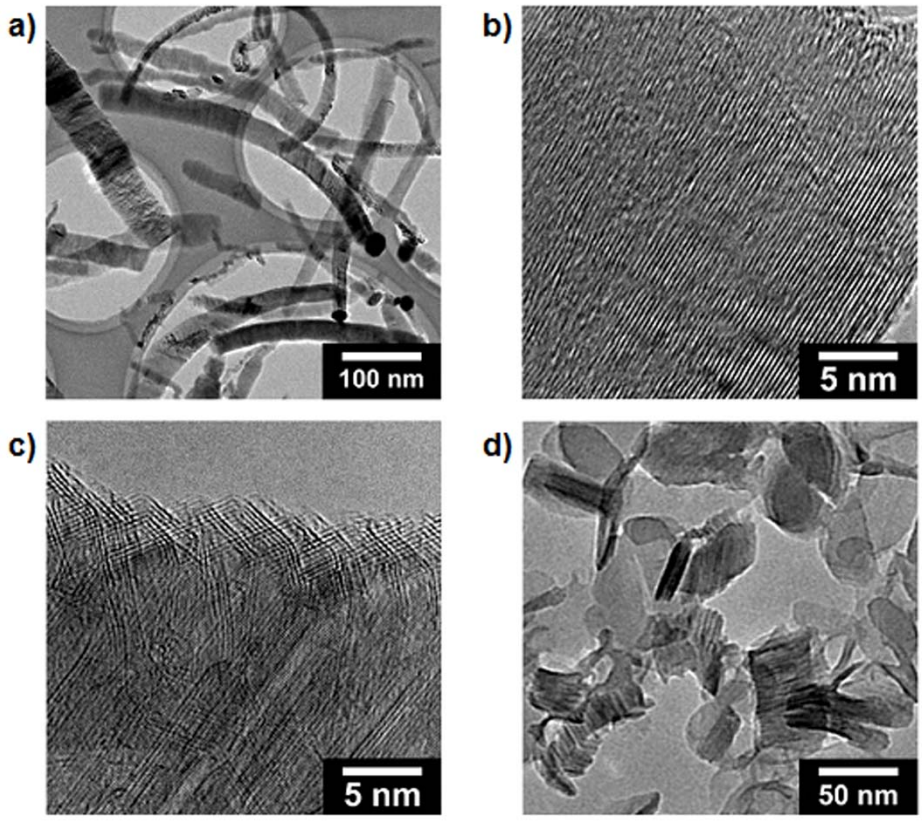

Figure 13. TEM images of as-prepared (a, b) and graphitized platelet carbon nanofibers (c). The platelet carbon nanofibers has relative small diameter of ca. 30–50 nm, allowing the fabrication of small-diameter graphene discs (d). Graphene discs are oxidized under controlled conditions ($R_{K/GP}$=3) and reduced by using mechanical reduction method.

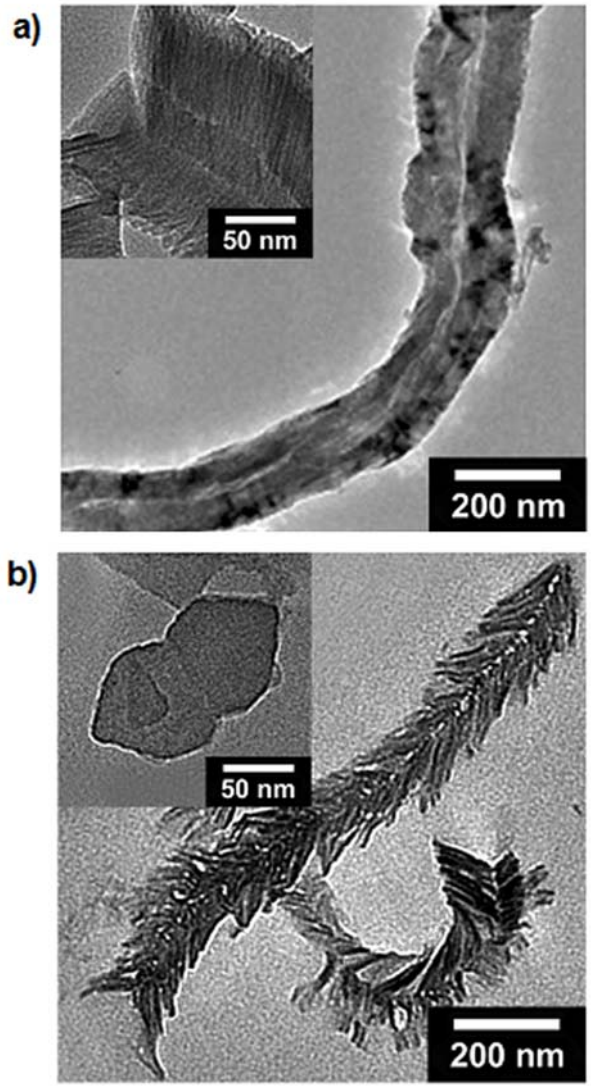

Figure 14. TEM images of (a) graphitized herringbone carbon nanofibers and (b) oxidized graphitized herringbone carbon nanofibers ($R_{K/GP}$=3) (inset: isolated bow-tie shaped graphene discs).

3.1.3. Mechanical reduction of oxidized graphene sheets

Since the discovery of graphene in 2004, they have published numerous research papers which have demonstrated the various reduction processes for the graphene oxide. Surveys of the main results obtained in this field have been summarized in several papers [87,88]. In this study, an alternative reduction method based on green technology (GT) is reported. A mechanical reduction method for graphene oxide is also proposed to combine the high recovery of π-conjugated electronic structure with the solution processability of graphene discs. First, the oxidized graphene discs were oxidized, and then completely exfoliate from GPCNFs. Reduction of oxidized graphene discs containing oxygen functional groups can be explained by the following two respects.

First, mechanical reduction mechanism is considered in terms of de-hydration of oxidized graphene discs. Figure 15 shows the schematic diagrams for the de/hydration process to the preparation of reduced graphene discs. The oxidized graphene discs were firstly oxidized, and then completely exfoliated from GPCNFs. The oxidized graphene discs containing oxygen functional groups such as epoxide and hydroxyl groups aligned perpendicular to the basal-plane carbon atoms and carboxylic acid groups at the edge of the basal plane of sheets. The oxygen reduction and simultaneous restoration of the network within the carbon structure (transformation of the carbon sp^3 bonds

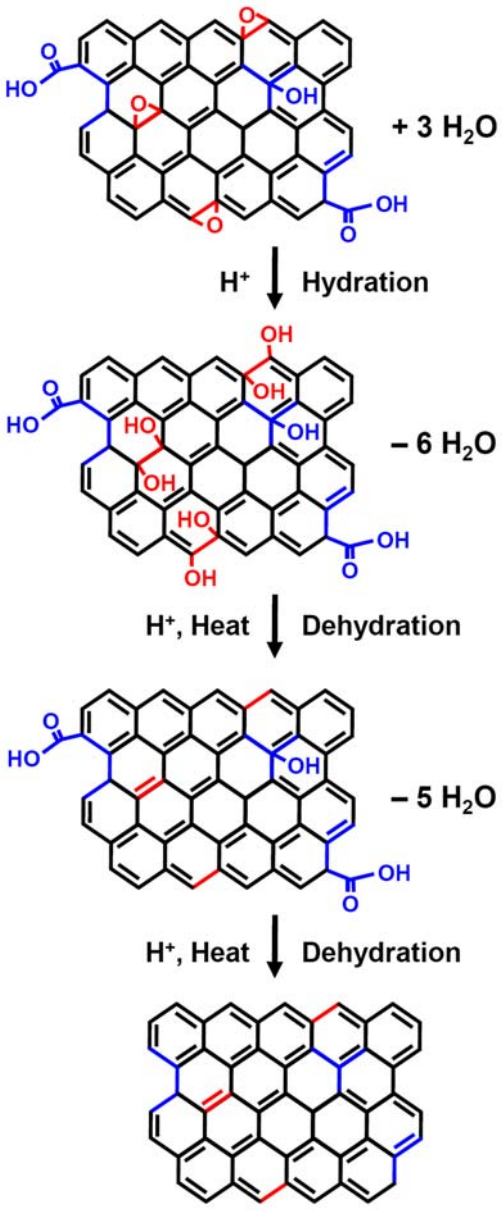

Figure 15. Schematic illustration for reduction of hydroxyl and epoxy groups for oxidized graphene discs to reduced graphene discs transformation.

sp^2) can be explained by dehydration of oxidized graphene discs in acidic aqueous medium as a source of H^+. The acid-catalyzed dehydration of epoxy groups is a two-step process. If an epoxy group is attached to carbon atoms of graphene discs with two hydrogen atoms attached to the neighboring carbons, in an acidic environment the system will first hydrate, transforming the epoxy group (–O–) to two hydroxyl groups (–OH), which then reduce to H_2O and graphene discs with sp^2-bonded carbon atoms. In the case of hydroxyl groups, the acid-catalyzed dehydration of alcohol is occurred *via* one-step process. If hydroxyl groups and hydrogen atoms are attached to two neighboring carbons, in an acidic environment they can combine through dehydration reaction, resulting in H_2O and reduced graphene discs with recovery of π-bonding. In addition, the dehydration of hydroxyl group can occur on the edges or basal planes of graphene discs. The edges of the oxidized graphene discs, as well as some parts of its basal plane, are terminated by hydrogen, hydroxyl, ether, and carboxylic groups. Thus, the elimination of OH and H can occur on the edge sites of graphene discs.

The mechanical reduction based on a wet milling technology can be considered as second factor. In general, during every chemical reaction sufficient energy needs to first be absorbed (endothermic) to break the bonds. This energy is called the activation energy and is defined as the minimum

amount of energy required by the reactants before products will form. Some reactions have higher activation energies and need to absorb much more heat energy in order to break the bonds. A covalent bond is an electrostatic attraction between positive protons in the nucleus (called the positive nuclear charge) of the bonded atoms and the negative shared electrons in the bond. To break this bond sufficient energy needs to be absorbed by the bond to overcome the attraction between the protons and electrons. The stronger the bond the greater the amount of energy required to break it. Under experimental condition, oxidized graphene disc solution was put into the chamber with a Filmics mixer that created a centrifugal field of *ca.* 18400 rpm. This high speed revolution of turbine caused the oxidized graphene discs to collide with each other, and endowed high surface energy to reduce the oxygen-containing functional groups and formed the sp^2 structure of carbon without any additives such as reducing agent.

Taking these results into account, it is concluded that both the acid-catalyzed dehydration and the high surface energy caused by wet milling technology give a combined or synergistic contribution to reduction of oxidized graphene discs into reduced graphene discs.

Figure 16 depicts UV-vis absorption spectra of reduced graphene discs. The reduction time directly affects the reduction of a colloidal suspension of

exfoliated graphene discs. The oxidized graphene discs had a maximum absorption wavelength (λ_{max}) at 230 nm related to π–π^* electron transition in the polyenetype structure. However, the reduced graphene discs (at 50 min of reduction time) exhibited a λ_{max} at 268 nm, which was contributed by π–π^* electron transition in the polyaromatic system. In a mechanical reduction process, both the bathochromic shift of λ_{max} and the hyper-chromicity were observered in the entire range (>230nm). These phenomena indicated that the π-conjugated electronic structure of graphene discs could be gradually recovered with increasing the reduction time [89].

Figure 17 also demonstrates the Raman spectra of as-prepared samples under various reaction procedures. The Raman I_D/I_G ratio is widely used to evaluate the quality of graphene nanomaterials. In general, I_D/I_G ratio of graphene is related to density of defects, as well as edge smoothness and edge structures (that is, arm-chair and zig-zag). However, because the edge structures of the graphene discs are unknown as yet, the I_D/I_G average ratio may reflect the quality of the graphene discs (including edge roughness, defects). All prepared samples represented a weak and broad band from 1250 to 3500 cm^{-1}. The Raman spectra indicated two strong wide bands near 1582

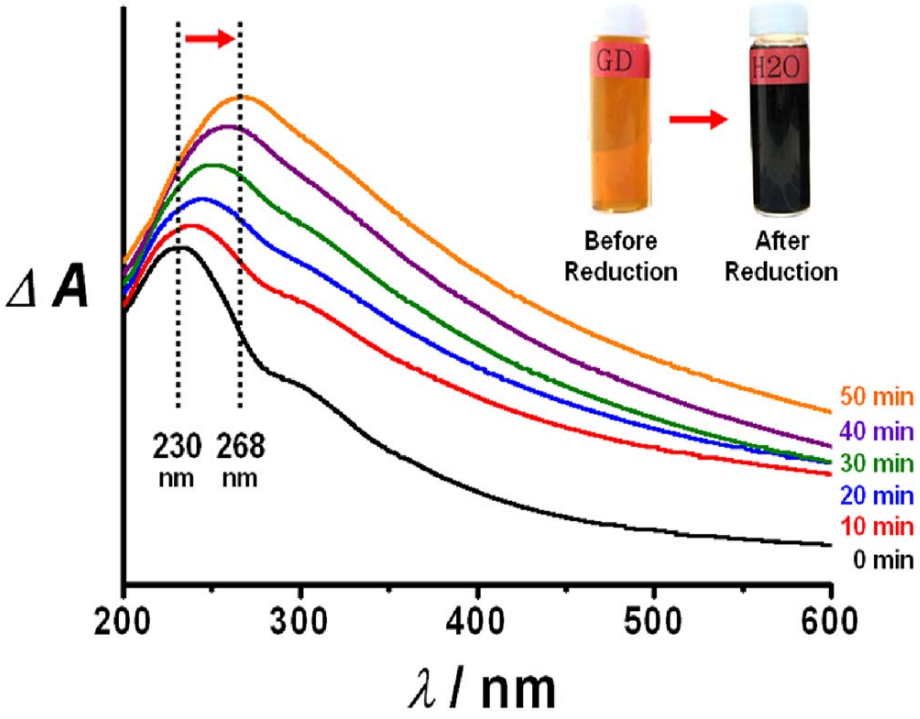

Figure 16. UV-vis absorption spectra of reduced graphene discs solution as a function of reduction time.

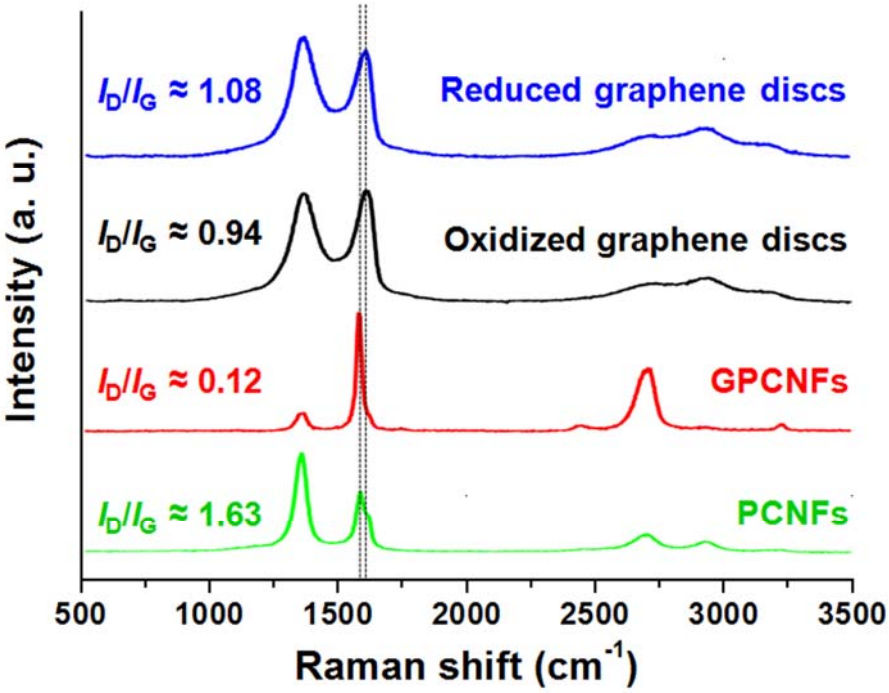

Figure 17. Raman spectra of reduced graphene discs, oxidized graphene discs, GPCNFs and PCNFs. Graphene discs are oxidized under controlled conditions ($R_{K/GP}$=6) and reduced by using mechanical reduction method.

and 1357 cm^{-1}. The peak located near 1582 cm^{-1} is due to the graphitic structure, whereas the peak near 1357 cm^{-1} is originated from disordered structure in the carbon. The Raman spectrum of the pristine GPCNFs, as expected, displays a prominent G peak, corresponding to the first-order scattering of the E2g mode ($I_D/I_G \approx 0.12$). In the Raman spectrum of oxidize graphene discs, the G band is broadened and shifted to 1594 cm^{-1}. In addition, the D band at 1363 cm^{-1} becomes prominent, indicating the reduction in size of the in-plane sp^2 domains, possibly due to the extensive oxidation. The Raman spectrum of the reduced graphene discs also contains both G and D bands however, with an increased D/G intensity ratio ($I_D/I_G \approx 1.08$) compared to that of oxidized graphene discs ($I_D/I_G \approx 0.94$). This change suggests that the oxidized graphene discs are transformed from amorphized states to more graphitic structures with significant amounts of defects [90,91].

To provide evidence that the reduction time affects the degree of reduction directly, the reduced graphene discs were also investigated by XPS techniques, Fourier transform infrared spectrometry (FT-IR), Atomic Force Microscope (AFM) and four-probe conductivity measurement. Figure 18 depicts a survey scan of oxidized/reduced graphene discs with the relative atomic percentages. Oxidized graphene consisted of carbon (67.2 %), oxygen (32.7 %), nitrogen (0.1 %), respectively. The C/O composition ratio of oxidized graphene discs

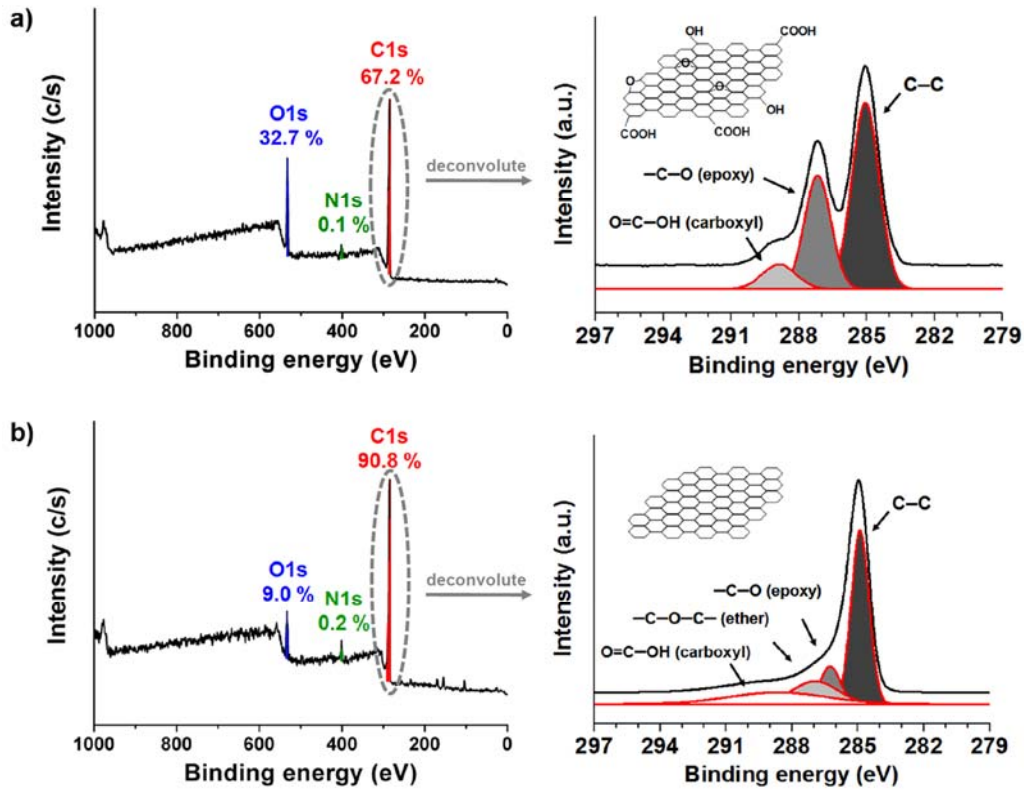

Figure 18. XPS Survey of a) oxidized graphene discs and b) reduced graphene discs. (right: XPS C1s spectra of oxidized graphene discs and reduced graphene discs) Graphene discs are oxidized under controlled conditions ($R_{K/GP}$=6) and reduced by using mechanical reduction method.

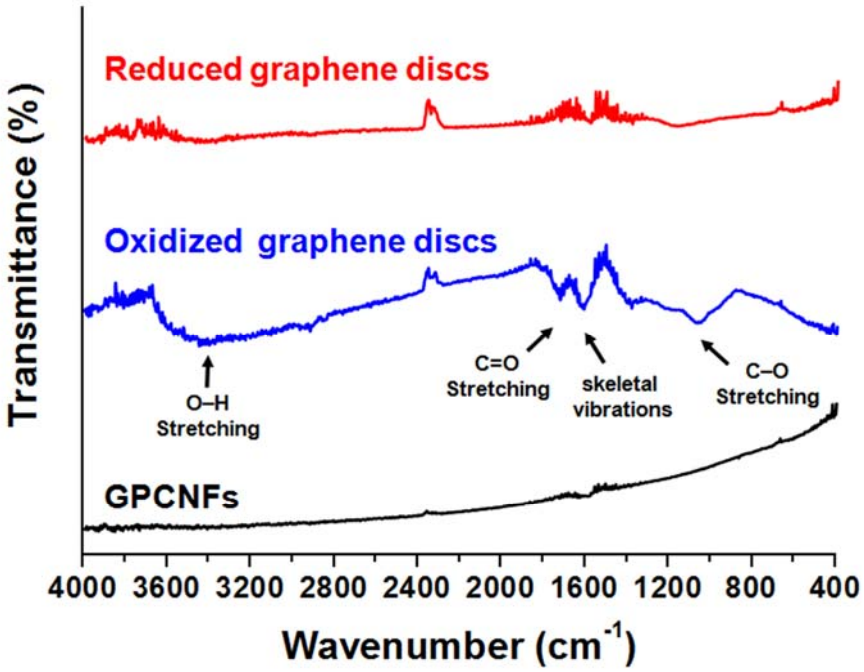

Figure 19. FT-IR spectra of reduced graphene discs, oxidized graphene discs and GPCNFs. Graphene discs are oxidized under controlled conditions ($R_{K/GP}$=6) and reduced by using mechanical reduction method.

(2.05) has good agreement with C/O ratio data obtained from CHN analysis (2.08). After mechanical reduction, the C/O composition ratio of oxidized graphene discs varied from 2.05 to 10.09 of high reduction level. The deconvoluted C1s XPS spectrums of oxidized graphene discs and reduced graphene discs by mechanical reduction are also presented. Generally, the C1s signal of oxidized graphene mainly consists of three components, which are C=C/C−C in aromatic rings (285.0 eV), C−O (286.5 eV) and O=C−OH (288.5 eV) peaks. While the C−O component comes from epoxy and hydroxyl groups, the O=C−OH bond originates from carboxyl groups. The XPS spectrum result was that ratio of the I_{C-O}/I_{C-C} decreased from 0.61 (oxidized graphene discs) to 0.21 (reduced graphene discs).

Figure 19 shows FT-IR spectra of GPCNFs, oxidized graphene discs and reduced graphene discs. While no significant peak was found in GPCNFs, the presence of different type of oxygen functionalities in graphene oxide was confirmed at 3400 cm^{-1} (O–H stretching vibrations), at 1720 cm^{-1} (stretching vibrations from C=O), at 1600 cm^{-1} (skeletal vibrations from unoxidized graphitic domains), and at 1060 cm^{-1} (C–O stretching vibrations). FT-IR peak of reduced graphene discs presents that O–H stretching vibrations observed at 3400 cm^{-1} was significantly reduced due to deoxygenation, and shows some reduction of epoxy groups.

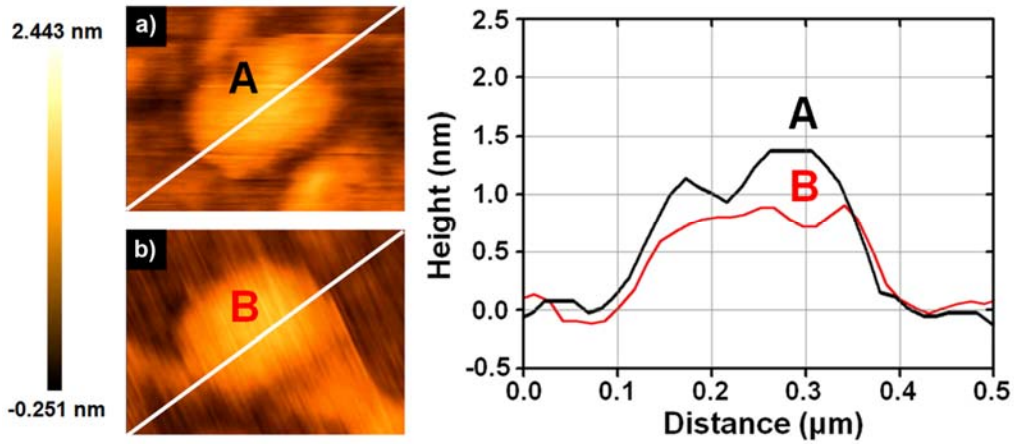

Figure 20. A non-contact mode AFM image of a) oxidized graphene disc and b) reduced graphene disc with height profiles along the diagonal line in the image. Graphene discs are oxidized under controlled conditions ($R_{K/GP}$=6) and reduced by using mechanical reduction method.

Table 2. Electrical properties of as-prepared samples

sample	electrical conductivity [a] (S/cm)
GPCNFs	1.5×10^{2}
Oxidized graphene discs [b]	7.4×10^{-4}
Reduced graphene discs [c]	1.4×10^{1}

[a] The measurement of electrical property was performed at ambient temperature by a four-probe method using Keithley 2400 as a sourcemeter, [b] Oxidized graphene discs are oxidized under controlled conditions ($R_{K/GP}$=6), [c] Reduced graphene discs are reduced by using mechanical reduction method.

An individual as-prepared graphene disc was observed by AFM measurement (Figure 20). The AFM image demonstrates that the thickness of the reduced graphene discs obtained is *ca.* 0.8 nm. This height value is smaller than that of oxidized graphene discs of *ca.* 1.2 nm. The height of oxidized graphene disc was expected to be thicker than the reduced graphene disc due to the presence of covalently bound oxygen and the displacement of the sp^3-hybridized carbon atoms.

To determine the extent to which the mechanical reduction of oxidized graphene discs restores the electrical properties of the graphitic network, the electrical conductivities of the GPCNFs, the oxidized graphene discs, and the reduced graphene discs were measured using four-probe conductivity measurement. The electrical properties of as-prepared samples are summarized in Table 2**.** The electrical conductivity of reduced graphene discs (1.4×10^1 S/cm) is about 5 orders of magnitude better than that of oxidized graphene discs, and closely approaches that of GPCNFs (approximately 10 times lower than the conductivity of GPCNFs).

Taking these results into account, it is concluded that both the acid-catalyzed dehydration and the high surface energy caused by wet milling technology give a combined or synergistic contribution to reduction of oxidized graphene discs into reduced graphene discs. The oxygen-containing

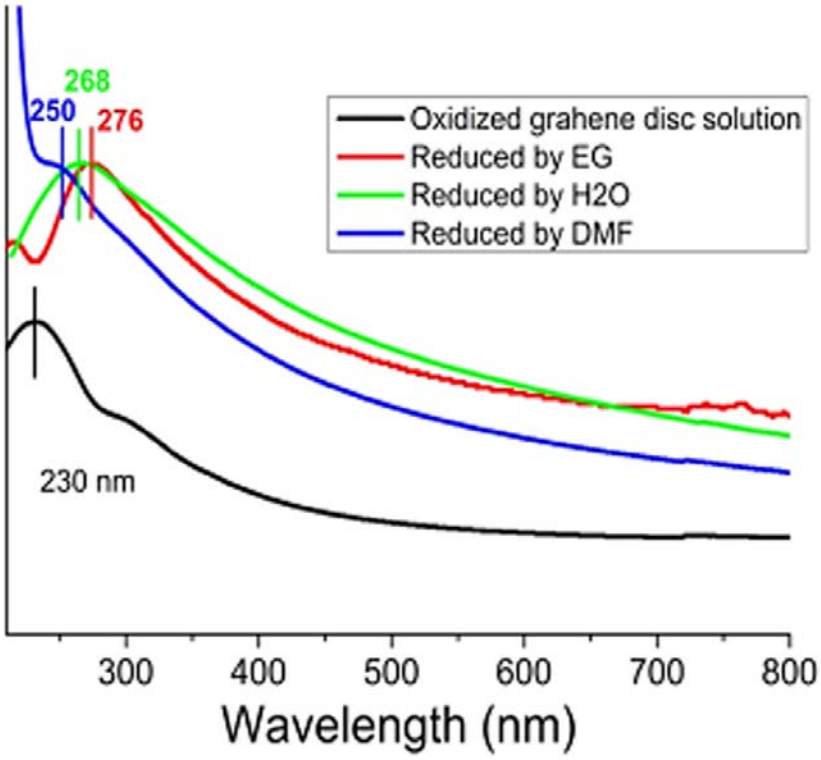

Figure 21. UV-vis absorption spectra of oxidized graphene disc solution. Graphene disc solution reduced by water, ethylene glycol, N, N-dimethylformamide, n-butanol and ethanol, respectively.

Figure 22. Various graphene discs solution is oxidized under controlled conditions ($R_{K/GP}$=6) and reduced by using mechanical reduction method.

functional groups were significantly removed from the surface of graphene discs as the mechanical reduction process proceeded gradually. The mechanical reduction of graphene discs can also be performed using other solvents such as ethylene glycol, propanol and N, N-dimethyl formamide, respectively. UV-vis absorption spectra also showed that the ethylene glycol provided best reduction performance owing to its intrinsic reduced characteristics (Figure 21). After the mechanical reduction, all prepared solutions exhibit a change of color from brown yellow to black, and notably, still kept in stable solution state. It could be ascribed in terms of the mixing effect, which prevented secondary agglomeration of graphene discs during the mechanical reduction process. By employing this mechanical reduction, the graphene disc solution with the concentration over 2.0 g L^{-1} was successfully acquired (Figure 22).

3.2. 'Bottom-up' Approach for Fabricating Single Layer Graphene Sheets based on a Layer-by-Layer Self-assembly

3.2.1. Preparation of poly(allylamine)/poly(styrenesulfonate) (PAA/PSS) multi-layer using layer-by-layer self-assembly

The overall synthetic procedure for graphene nanosheets is represented in Figure 23. The LbL approach was used to form poly(allylamine)(PAA)/ poly(styrenesulfonate)(PSS) multi-layer on a quartz substrate. During the carbonization process, the PSS layers could be transformed into graphene nanosheets due to its inherent aromatic and highly ordered structure [92,93]. PAA layers served to protect the structural layers as well as prevent the agglomeration of graphene nanosheets. Namely, PSS layer provides a carbon source for the formation of graphene nanosheet and PAA layer acts as a sacrificial layer.

The influence of the PAA layer on the formation of graphene nanosheets can be presumed by thermogravimetric (TG) analysis using similar conditions as performed in the carbonization process. In Figure 24, it is possible to observe the weight loss starting around around 200°C for PAA. After 200 °C, mass loss of the PAA occurs very rapidly. Whereas, the degradation rate for PSS is very low in comparison to the PAA. TGA data for PSS, it is observed that the degradation starts about 400 °C. A weight loss about 400 °C is

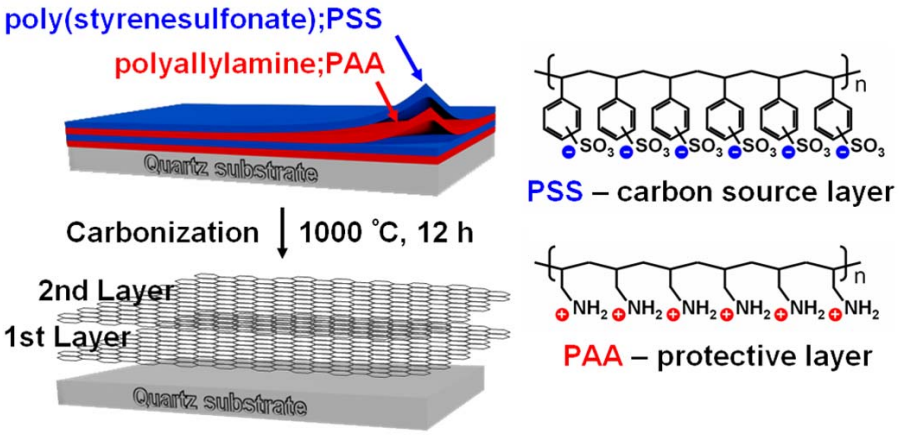

Figure 23. Formation mechanism for the multi-layer epitaxial graphene nanosheets on a quartz substrate.

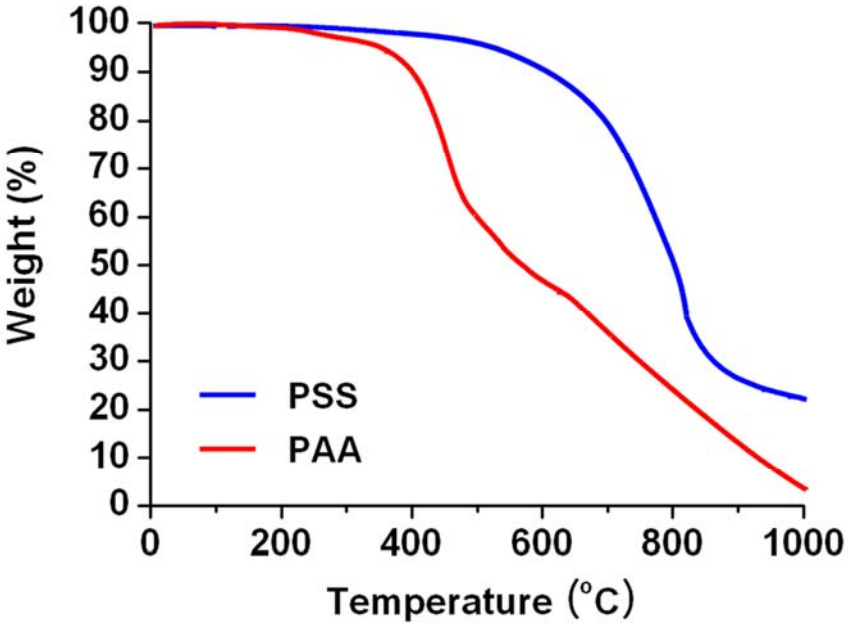

Figure 24. Thermogravimetric analysis of PSS and PAA.

observed in PSS that may be due to removing of sulfonic group of the PSS. Finally, the residual weight at 1000 °C (final temperature of carbonization) is almost zero (0.15 %), while the residual weight of the PSS at 1000 °C is more than 20%. The comparison of PAA and PSS TGA data confirms that the PSS has more thermal stability compared to the PAA.

3.2.2. Carbonization of PSS/PAA multi-layer and oxidation/ reduction of graphene sheets

Under our experimental conditions, the graphene formation occurs at moderate temperatures (< 1000 ºC). Interestingly, this phenomenon can be attributed to the presence of metallic dopant such as ferric cations. Importantly, the metallic dopant functions as both a transition metal and a pillar agent [97]. It has been reported that transition metals (Fe, Co, Ni, Mn, etc) can induce graphitization of the carbon source, since they act as catalysts in the heat treatment process [98–101]. The control experiment indicated that the metallic dopant induced facile cyclization and mass transfer during carbonization process (Figure 25). Furthermore, the multi-valent metallic dopant formed an ionic crosslinking with neighboring sulfonate groups ($-SO_3H$) in the PSS layers. The resultant crosslinking acts as a pillar to prevent agglomeration and shrinkage of graphene nanosheets.

During the carbonization process, The PSS layer with high thermal stability is suitable for forming graphene nanosheets as a carbon source for the formation of graphene nanosheets. In addition, thermal degradation of PAA layer allows neighboring graphene nanosheets to support each other from its initial growth phase and thus effectively prevent them from growing into randomly oriented graphene nanosheets on quartz substrates.

The formation of graphene nanosheets was confirmed by TEM analysis (Figure 26). The TEM observation revealed that the single graphene nanosheet has flake-like shape of graphene monolayer. The existence of fine wrinkles indicated some defects on the graphene surface during carbonization process. The Raman spectra indicated two strong wide bands near 1582 and 1357 cm^{-1} (Figure 26 inset). The peak located near 1582 cm^{-1} is due to the graphitic structure, whereas that the peak near 1357 cm^{-1} is originated from disordered structure in the carbon.

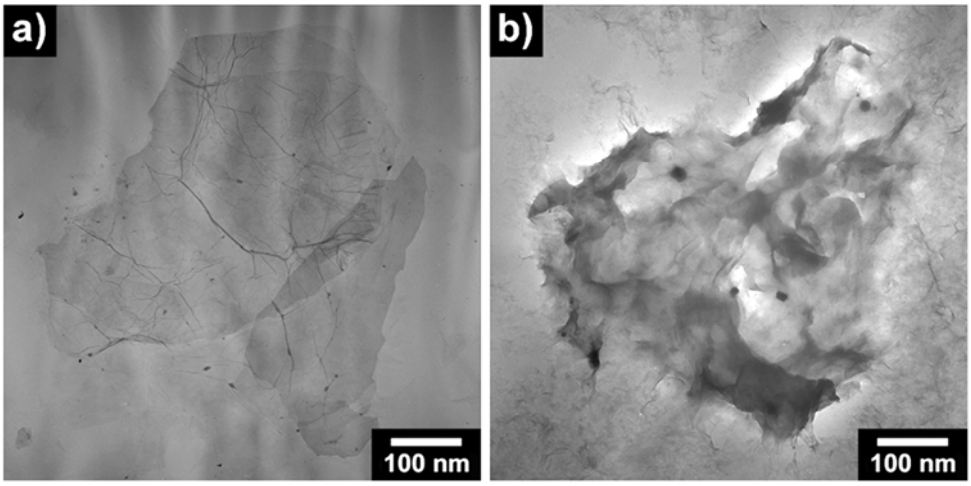

Figure 25. TEM image of graphene nanosheets prepared by LbL self-assembly approach: (a) with a metallic dopant, (b) without a metallic dopant.

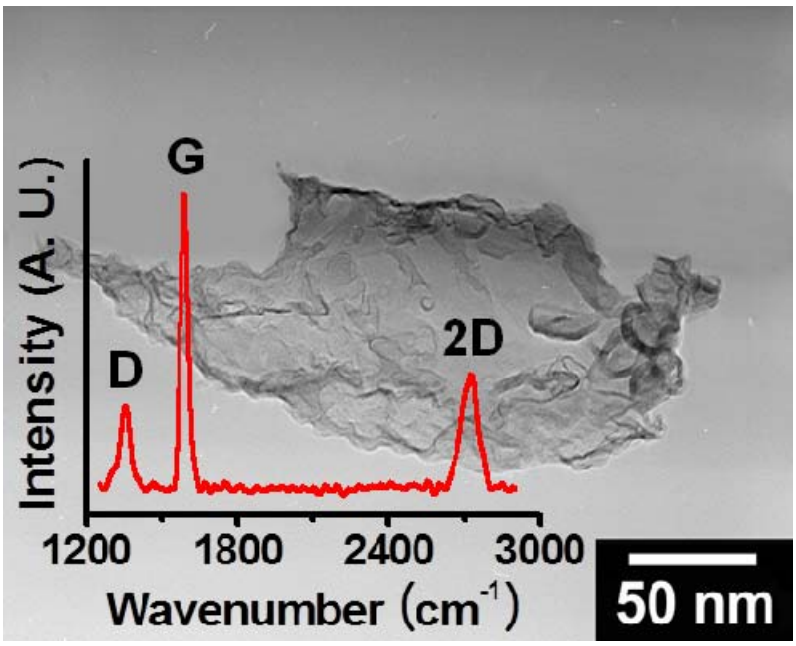

Figure 26. TEM image of graphene single nanosheet prepared by LbL self assemble (inset: Raman spectrum of graphene nanosheets (thickness~100 nm) deposited on a silicon wafer).

Figure 27 demonstrates the Raman spectra of as-carbonized PSS/PAA multi-layers under various reaction temperatures. Under our experimental condition, the samples represented a weak and broad band from 1250 to 1750 cm^{-1}. Interestingly, no carbon structures were found at 400 °C. Above 500°C, the Raman spectra indicated two strong wide bands near 1582 and 1357 cm^{-1}. The peak located near 1582 cm^{-1} is due lo the graphitic structure, whereas that the peak near 1357 cm^{-1} is originated from disordered structure in the carbon. With increasing reaction temperature, the intensity of the disordered structure (D peak) decreases, which indicates that the randomly and disorderly formed carbon structures are removed during heat-treatment. In addition, it is known that an increase in degree of carbon crystallinity is reflected by an increase in the intensity of the G mode, as well as a decrease in its bandwidth. The D mode intensity of the carbonized PSS/PAA multi-layers increased remarkably and narrowed its bandwidth above 1000 °C, indicating that the amount of amorphous carbon structure in the as-carbonized PSS/PAA multi-layers is very small. Consequently, the Raman results reflected that the I_D/I_G ratio decreased with increasing reaction temperature. This relatively small ratio of I_D/I_G ($I_D/I_G \approx 0.17$) indicated that the as-prepared graphene nanosheets had a low defect level in the atomic carbon structure [94,95].

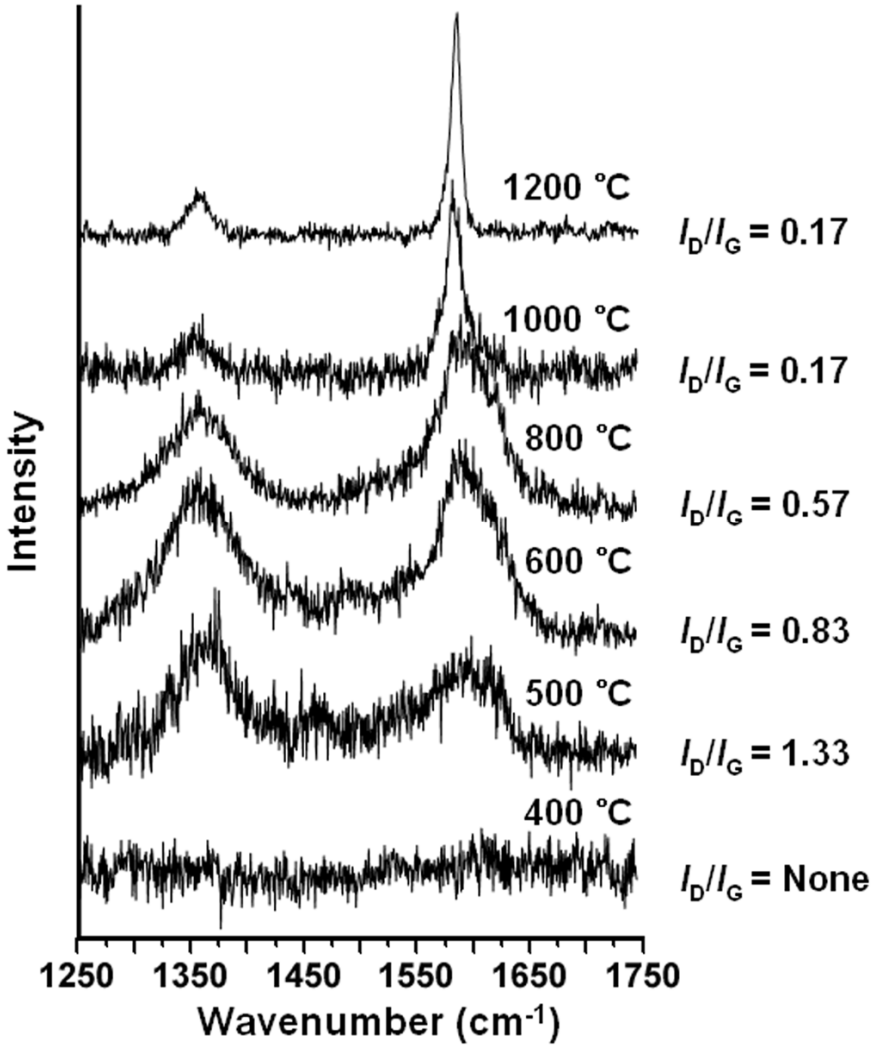

Figure 27. Raman spectra of resulting as-carbonized PSS/PAA multi-layers under various carbonization temperatures.

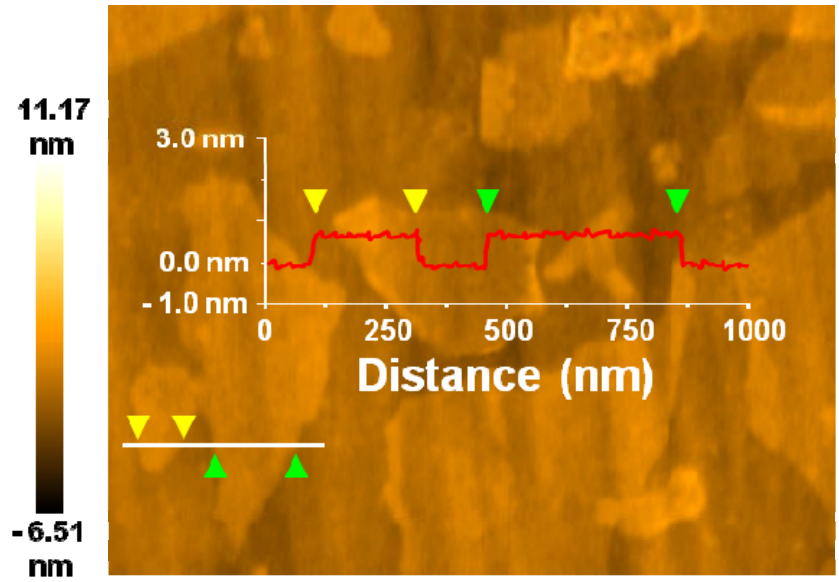

Figure 28. AFM image of graphene nanosheets (inset: a line scan taken vertically through the dashed line on the topography image).

In Figire 28, atomic force microscopy (AFM) image illustrated large numbers of graphene nanosheets, and their topography image revealed that the thickness of graphene sheets was measured to be 0.8–1.0 nm, consistent with monolayer graphene [96]. In addition, Figure 29 displays curve fitting of C1s peak of X-ray photoelectron spectroscopy (XPS) spectrum. The XPS spectra represented the nature of carbon and oxygen bonds. The characteristic peaks of graphene nanosheets appeared at 285.0 eV, 286.5 eV and 288.5 eV, which were originated from graphitic carbon C–C, C–O and O=C−OH, respectively. Furthermore, XPS spectrum depicts a survey scan of graphene nanosheets with the relative atomic percentages of carbon (91.9 %), oxygen (8.7 %), and nitrogen (0.2 %), respectively (Figure 30). Judging from these data, it could be concluded that the PAA/PSS multi-layers prepared by LbL method were successfully transformed into graphene nanosheets. Figure 31 demonstrates optical transmission spectra as a function of wavelength. The transmittance (λ = 550 nm) varies from 92 to 71 % as the films thickness increases from 10 to 100 nm.

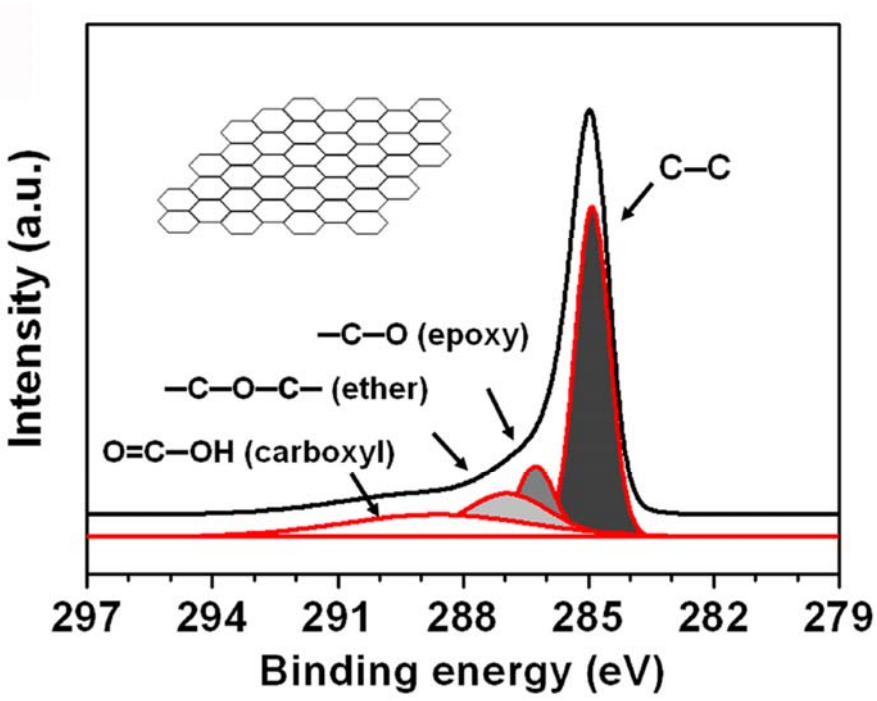

Figure 29. Deconvoluted XPS spectrum for graphene nanosheets.

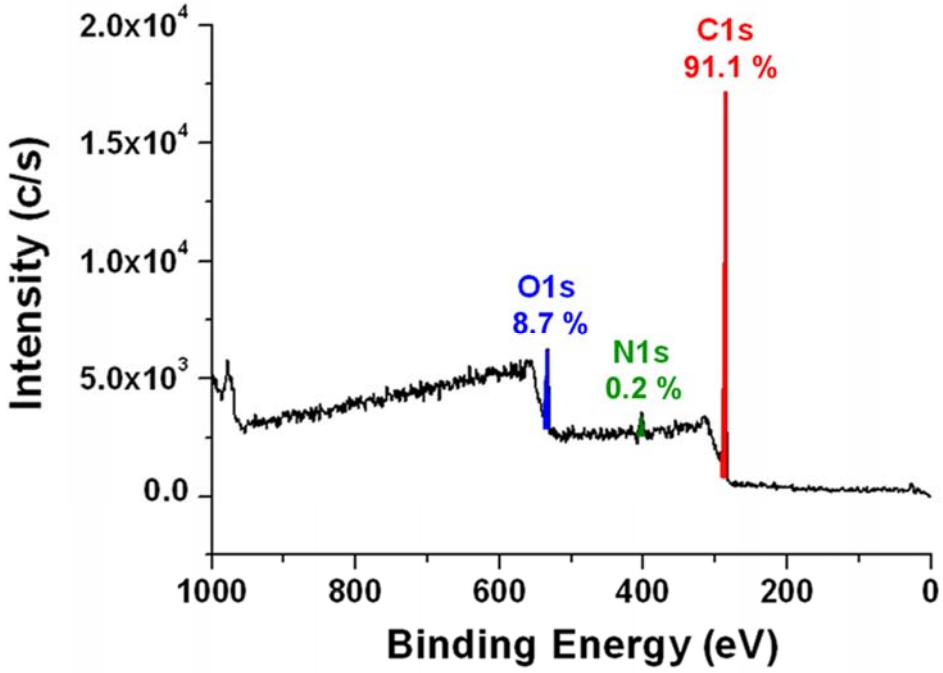

Figure 30. Survey XPS of as-synthesized graphene nanosheets.

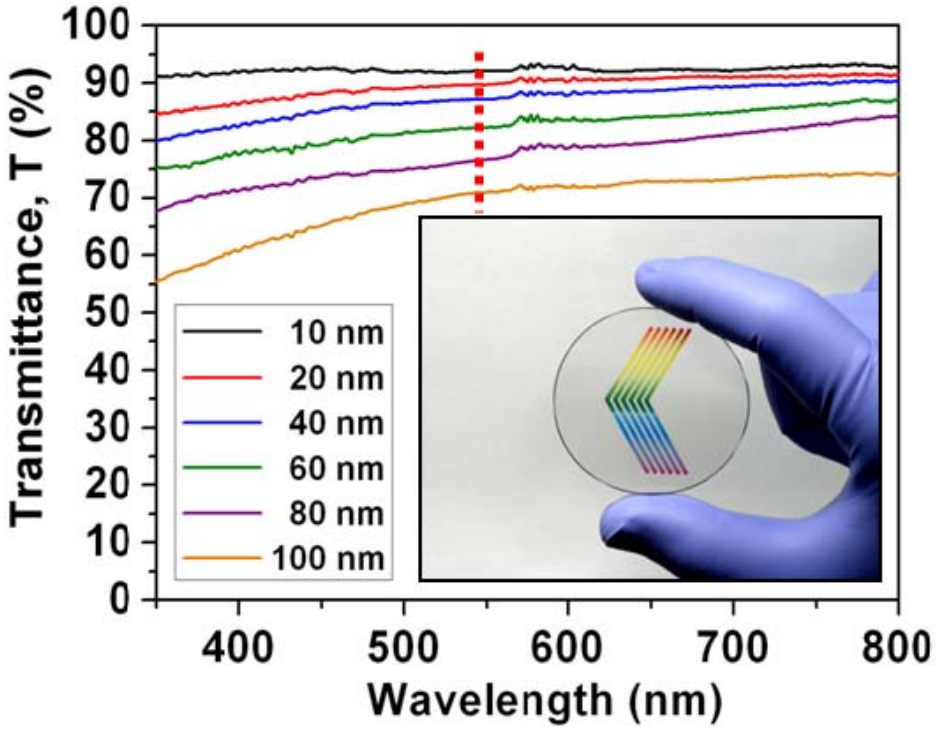

Figure 31. Transmission spectra of graphene sheet as a function of sheet thickness.

3.3. Applications

3.3.1. Foldable graphene electrode using ink-jet printing method

The as-synthesized graphene nanosheets could be applied as optically transparent electrode. In order to evaluate the optical and electrical properties of graphene nanosheets, the graphene nanosheets were transferred to a polyethylene terephthalate (PET) substrate by vacuum filtration method [102]. A uniform flexible graphene film was obtained by vacuum filtration of this dilute graphene suspension using an anodic aluminum oxide (AAO) membrane and wet-transferred to a PET film. The film thickness could be controlled by varying the filtration volume (Figure 32).

The transmittance and sheet resistance of graphene films are plotted in the viewpoint of film thickness (Figure 33). The transmittance and sheet resistance of graphene films decreased as the film thickness increased. The lowest sheet resistance value obtained in this study was ~1.2 kΩ sq^{-1} coupled with transmittance of ~ 71 %, which was comparable to that of graphene films prepared by other methods [103,104].

Figure 34 presents the current–voltage (*I–V*) characteristics of the graphene nanosheets deposited onto the PET substrates. The *I–V* characteristics are primarily determined by the intrinsic properties of the graphene nanosheets. All prepared samples exhibit the linear *I–V* curves over a voltage range from −0.1

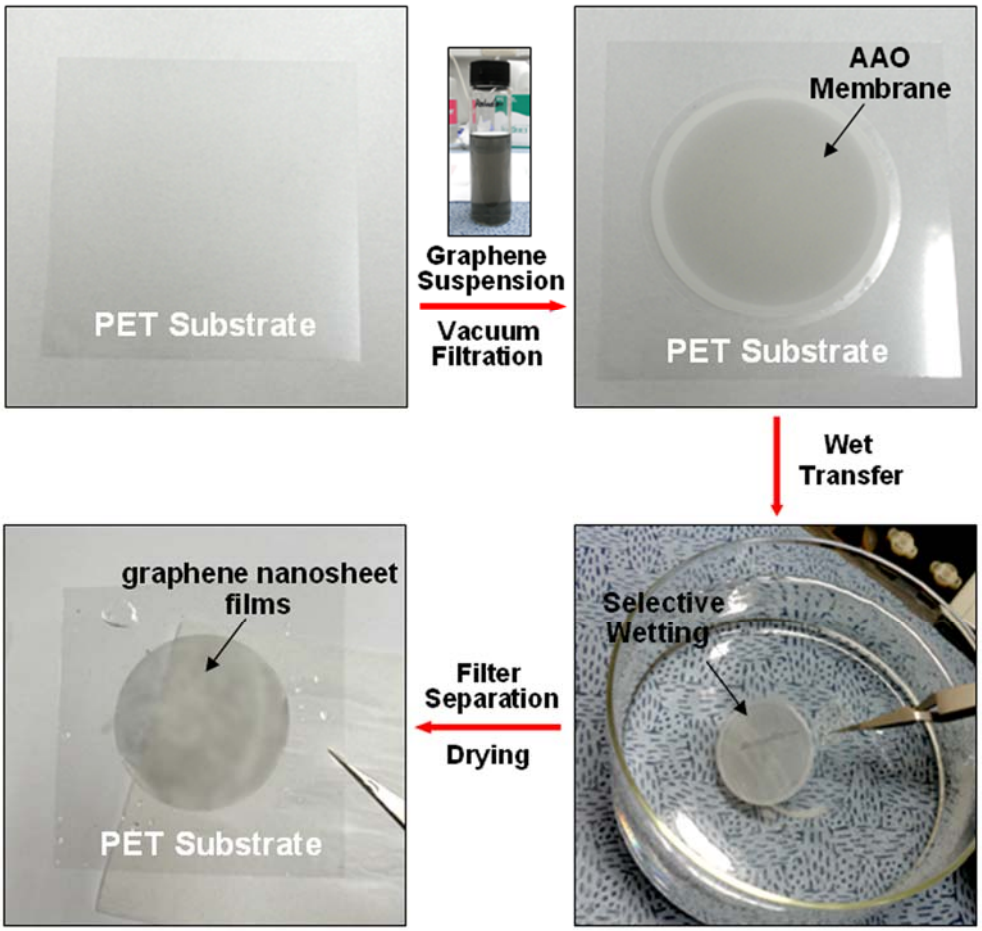

Figure 32. Digital photograph images of the filtration-wet transfer process. A uniform flexible graphene nanosheet film was obtained by vacuum filtration using an AAO membrane and transferred to a PET film.

to +0.1 V confirmed the Ohmic behavior. Furthermore, the dV/dI values were also dependent on the films thickness. For graphene film with thickness less than ~10 nm, the dV/dI value increased approximately 1~2 orders of magnitude compared to that of relatively thick films. In the case of the graphene film, the conductive pathway was created by the laterally contacted aggregates of individual graphene nanosheets. Therefore, deposition of relatively larger amounts of the corresponding samples is required to constitute adequate conductive pathways [105]. For this reason, the dV/dI values of the graphene films decreased with increasing film thickness. Hence, the above I–V characteristics provide an important observation in that the control of contact resistance by tailoring the film thickness can induce different electrical properties in a graphene-based electronic device.

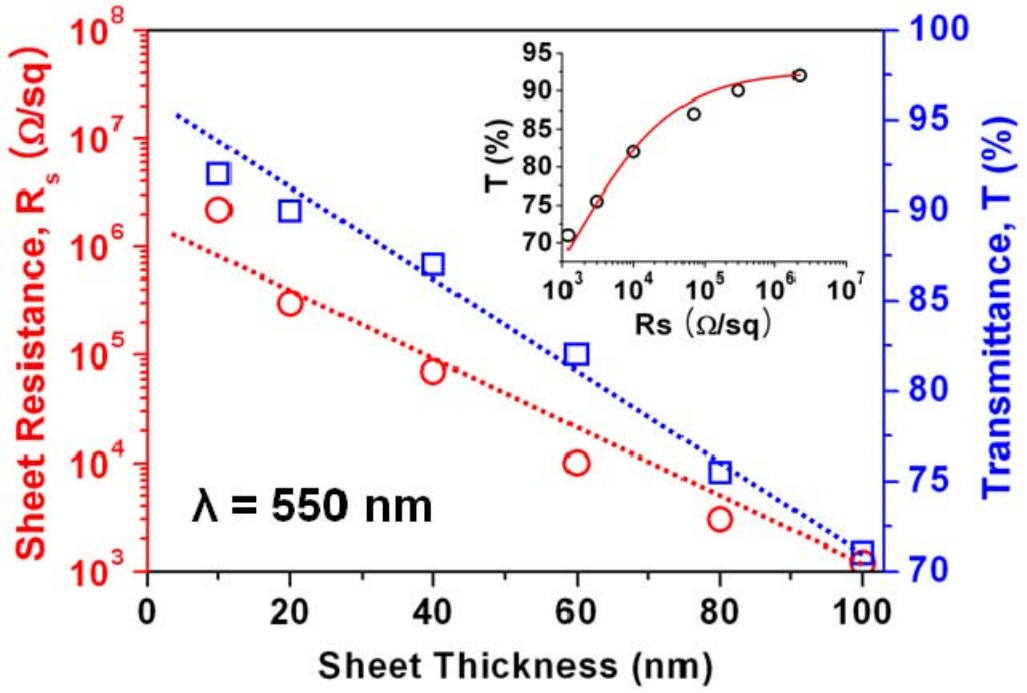

Figure 33. Transmittance (550 nm) and sheet resistance of prepared graphene sheets as a function of thickness. (inset: The same data represented by transmittance versus sheet resistance).

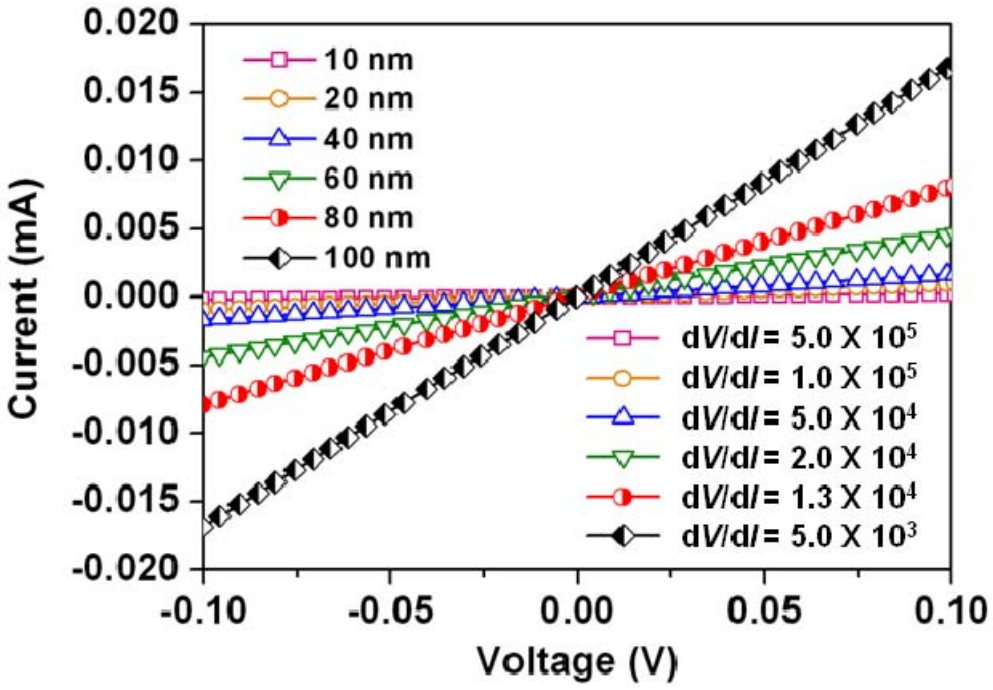

Figure 34. *I–V* characteristics of graphene sheet at a scan rate of 50 mVs^{-1}.

Figure 35 demonstrates the practical applications of a foldable printed circuit boards. An electrically conductive wire (100 % graphene nanosheets, thickness of 300 nm, width of 5 mm) was patterned on a polyimide film. The pattern designed on computer software is inkjet printed repeatedly for 30 passes. The light emitting diodes (LEDs) connected in series and applied by a 27.0 V DC power supply. The electrically connected LEDs could be turned on by applying voltage, demonstrating electrically conductive pathway of the graphene-based printed circuit (Figure 36).

In order to achieve an in-depth insight into the flexibility of graphene-based printed circuit, the electrical fatigue of graphene film on polymer substrate need to be considered. The electrical fatigue was calculated by measuring the sheet resistance change $\Delta R/R_s = (R–R_s)/R_s$, where R and R_s are the measured resistance and initial sheet resistance, respectively.

The graphene-based printed circuit was folded with angles ranging from –180° to +180° (Figure 37 inset). Figure 37 indicated that the sheet resistance increased in proportion to the amount of the fold: folding the circuit –180° (acute angle) led to *ca.* 10 % increase in sheet resistance; folding the circuit +180° (obtuse angle) led to *ca.* 12 % increase in sheet resistance. These results can be ascribed in terms of the mechanical aspects (compressive stress and tensile stress). In general, graphene nanosheets have a high tendency to stack

together (π–π stacking) such that the overlapping π orbitals lead to extensive charge delocalization, resulting in a conductive pathways. However, the mechanical deformation of stacked graphene film affects their high degree of regioregularity, and reduces the charge-carrier mobility. Under our experimental condition, both acute folding and obtuse folding produce structural fractures in the graphene film, lead to a decrease in the electrical conductivity.

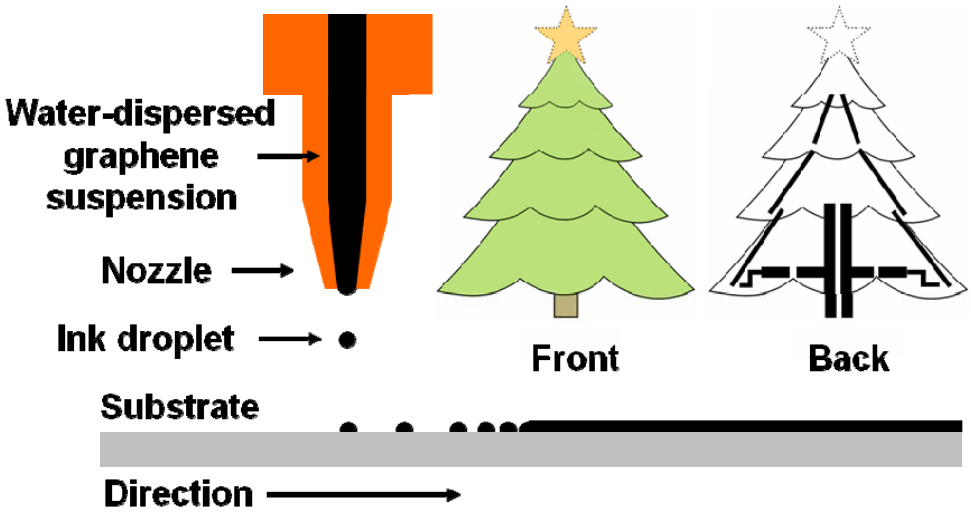

Figure 35. Designed graphene-based electronic circuit pattern for ink-jet printing.

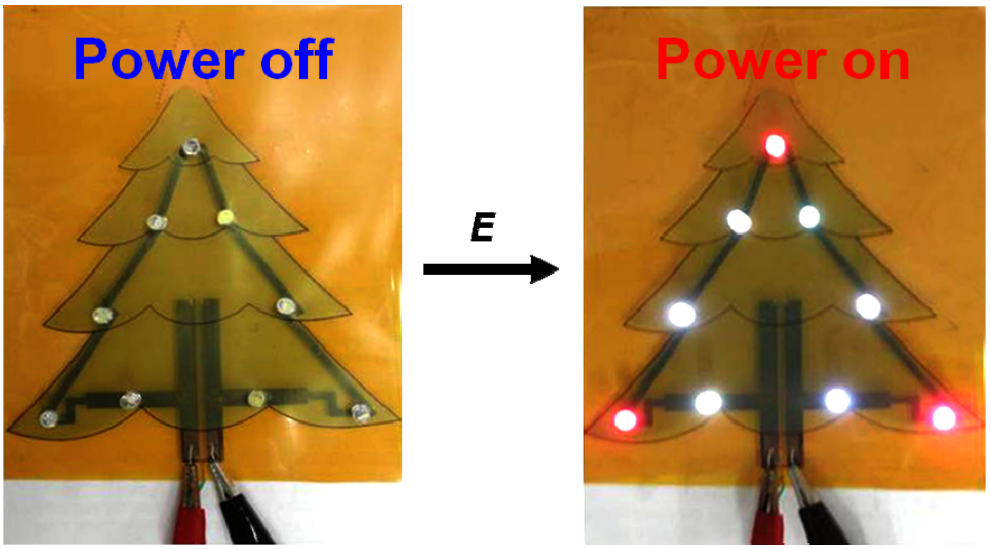

Figure 36. Digital photographs of graphene-based electronic circuit turn off and turn on.

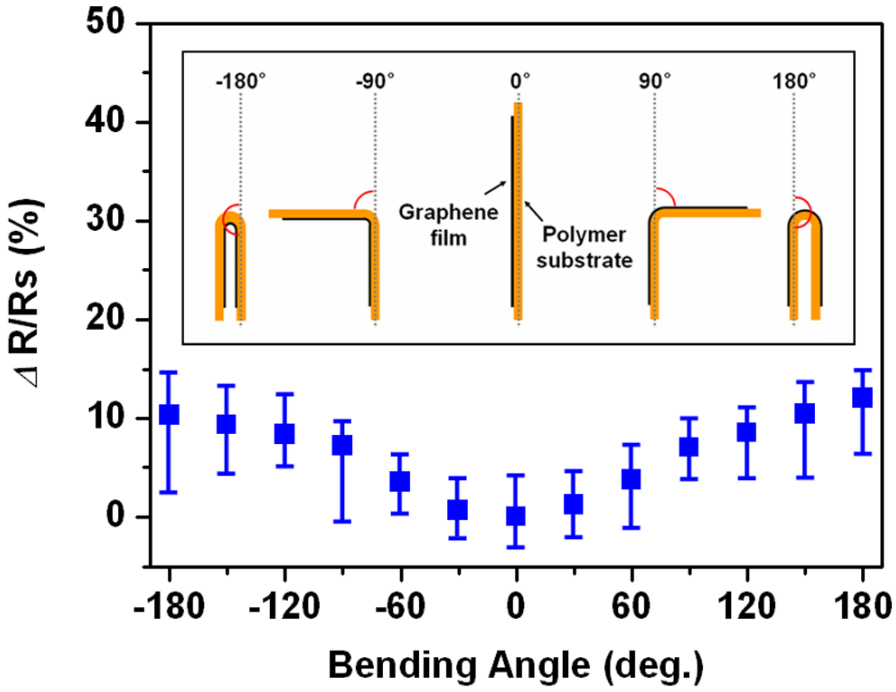

Figure 37. Sheet resistance changes of graphene-based electronic circuit as a function of bending angle. (inset: schematic diagram of graphene film on polymer substrate and folded to various angles)

3.3.2. Graphene patterning *via* ink-jet printing method and their application to wideband dipole-antenna

The overall procedure for line patternings of graphene sheets by inkjet printing is illustrated in Figure 38. In general, ideal ink for inkjet printing is required to have viscosity between 1 and 20 mPa s and to match the surface tension of the ink with the corresponding surface energy of the substrate.[6] In this experimental condition, the exfoliated GO aqueous solution had excellent dispersibility due to its hydrophilic property [106,107]. The viscosity value of GO aqueous sloution was measured to be *ca.* 2.2 mpa s, and this viscosity value is sufficient for inkjet printing without any other additives. In addition, to match between the surfaces energy of a substrate and the surface tension of GO ink (72.8 mNm^{-1}), PET film was treated with oxygen plasma. The surface energy of substrate increased from 41.0 mNm^{-1} to 68.7 mNm^{-1}. The GO based ink satisfying the above conditions could be printed out precisely onto the substrate *via* loading the GO solution to modified ink cartridge and patterned efficiently in large area (Figure 38b). Inherently, GO was electrically insulating because of the structural defects and oxidized GO domains [108,109]. Consequently, an additional reduction step is needed to make it electrically active. Under this experimental condition, this reduction process was conducted using the hydrazine vapor deposition and mild thermal annealing.

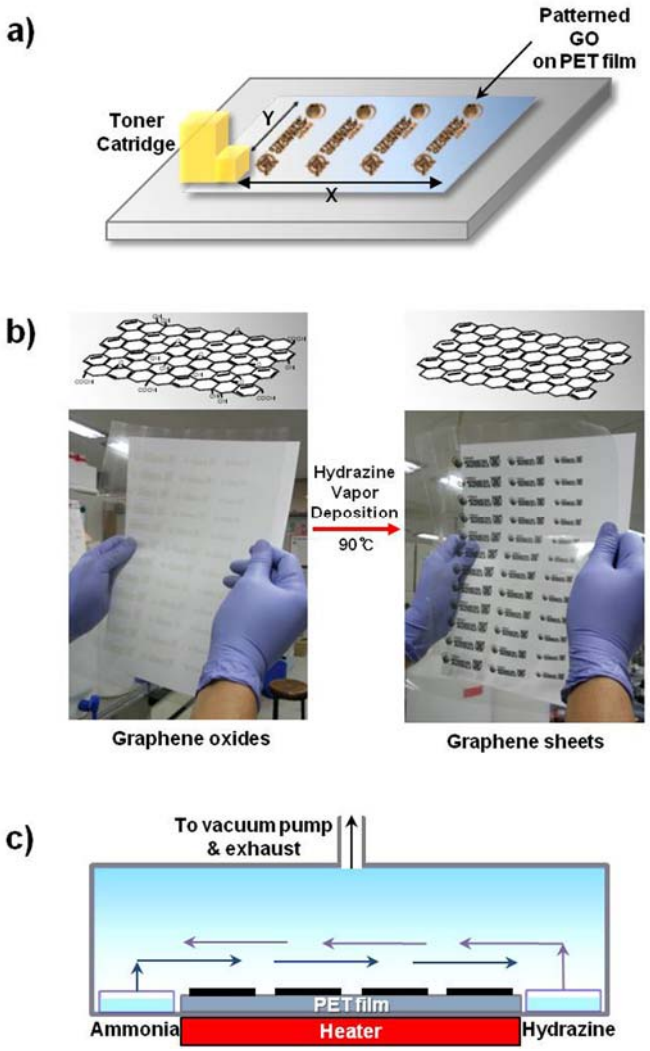

Figure 38. a) The fabrication of patterned GO on PET film by inkjet printing. b) Large-area patterned GO (left image) and graphene sheets resulted from the reduction procedure (right image). c) The reduction process was performed by mild-thermal annealing at 90°C with hydrazine and ammonia vapor.

In order to measure the thickness of the graphene-based thin film, AFM analysis was also performed to the film acquired by inkjet printing for 1 pass and VDP process. Figure 39a shows that the film thickness was estimated to be ca. 10 nm. As a result of up to a printing number of 30, it was noticed that the film thickness was linearly increased with increased printing number, and the average layer thickness was considered to be *ca.* 10~15 nm (Figure 39b). From the point of view, it was evident that graphene-based thin film consisted of a few layers of graphene.

The graphene sheet patterns prepared by inkjet printing are compared with the other conducting polymers such as polypyrrole (PPy) and polyaniline (PANI) (Figure 40) [110,111]. It demonstrated that well-defined patterns with various shapes and line widths of patterned graphene sheets were more clearly observed than those of the other conducting polymers on the PET film. For the definite comparison of line resolution, the minimum lines with *ca.* 70 μm were patterned (Figure 41). It also showed that the resolution of patterned graphene line was much higher than those of the others. The difference of resolution could be attributed to rapid polymerization process, matching surface energy between substrate and ink, and grain property on domain structure. In other words, as evaporated monomers were promptly deposited and polymerized on the patterned oxidant ammonium persulfate (APS) film, polymer nanoparticles

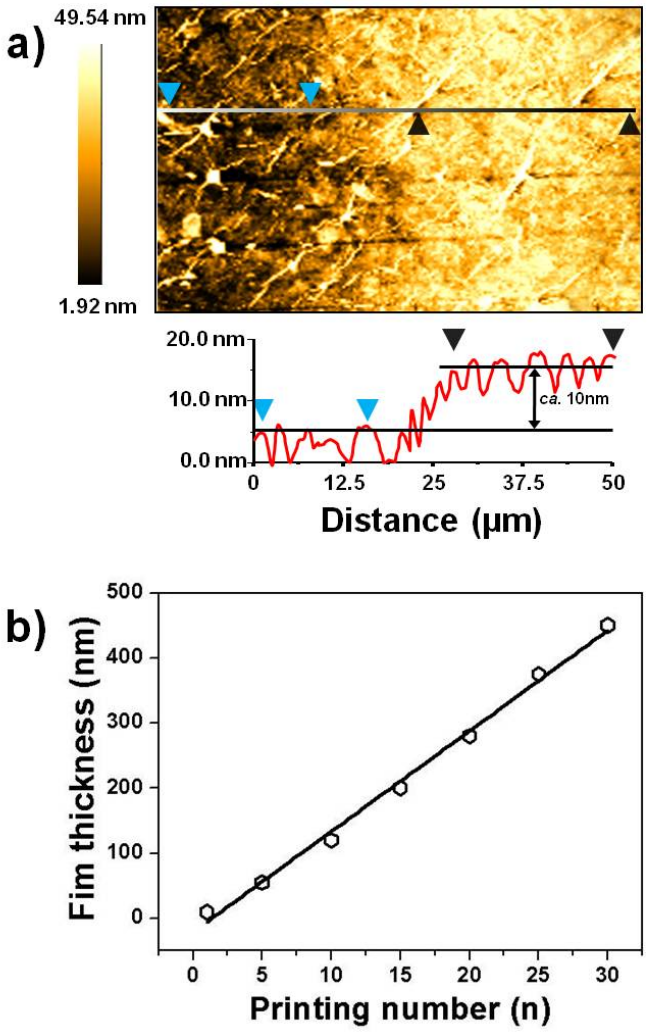

Figure 39. a) AFM image of patterned graphene sheets with 70 μm line width obtained by inkjet printing for 1 pass and reduction process (observable range of AFM : 50 μm) b) The film thickness of patterned graphene sheets as a function of printing number.

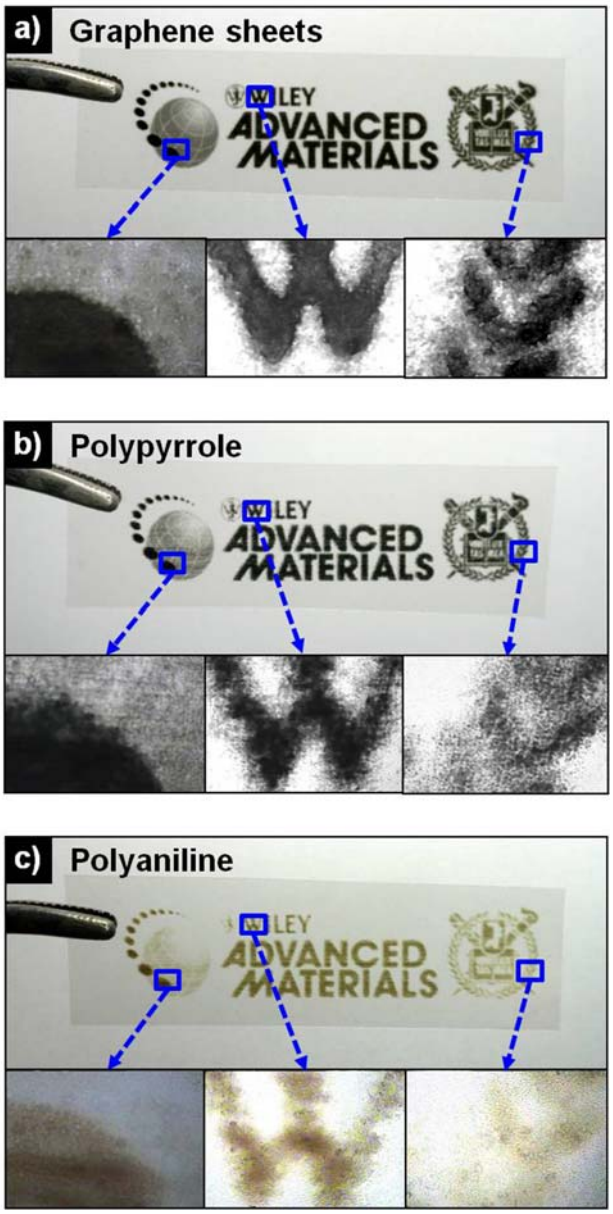

Figure 40. The various optical images of a) graphene sheets b) PPy c) PANI patterns prepared by inkjet printing and VDP method. The optic images were magnified at marked areas.

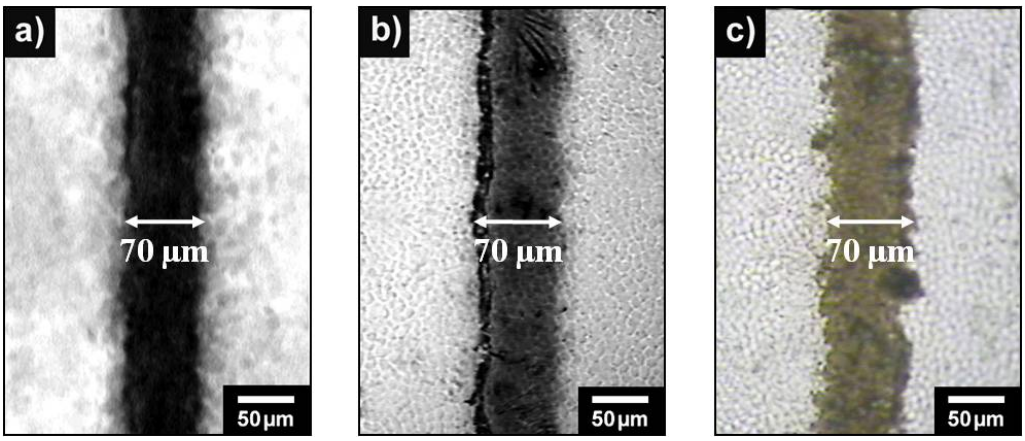

Figure 41. The optical micrographs of patterned straight lines of a) graphene sheets b) PPy c) PANI with the width of *ca.* 70 μm. In all images, the scale bar is 50 μm.

were aggregated that resulted in cracks and wrinkled form. Furthermore, high difference of surface tension between APS ink and oxygen-treated PET film caused matching problem of surface energy, resulting in forming line-edge waveness. For these reasons, high resolution of patterned graphene could be obtained.

In addition, the patterned graphene sheets with various line widths were successfully fabricated (Figure 42a, b and c). To clarify how well-defined patterns was formed without ink spread, dotted line having a gap of 70 μm between dots was printed, and then, current was measured by 2-probes of the multimeter connecting to the both ends of the dotted line. The current of the dotted line was zero unlike that of the full lines, which indicated that each dot of the dotted line was electrically distinct from each other, and the patterned graphene sheets were synthesized properly without ink spread (Figure 42d).

Moreover, the successful designed gradient pattern reveals that the electrical conductivity can be readily regulated in the same line, and suggests the possibility to fabricate various types of electrodes (Figure 43). The changes in concentration of GO ink and the number of printing were also capable of tuning the sheet resistance finely.

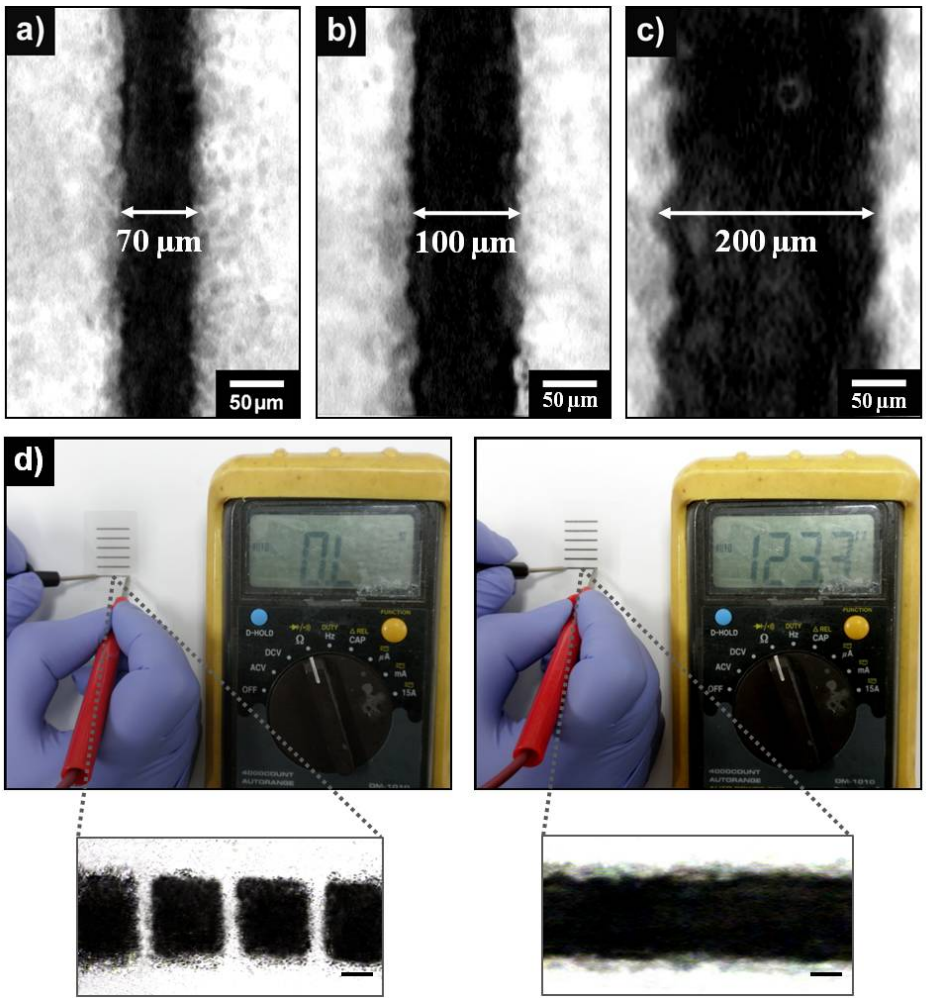

Figure 42. The optical micrographs of patterned graphene-based thin film with the width of a) *ca.* 70 μm b) *ca.* 100 μm c) *ca.* 200 μm. In all cases, the scale bar is 50 μm. d) The electrical measurement of the full line and consecutive repeated pattern having a gap of 70 μm between dots in the dotted line by using the multimeter. The pattern was magnified by optical microscopy (scale bar: 125 μm)

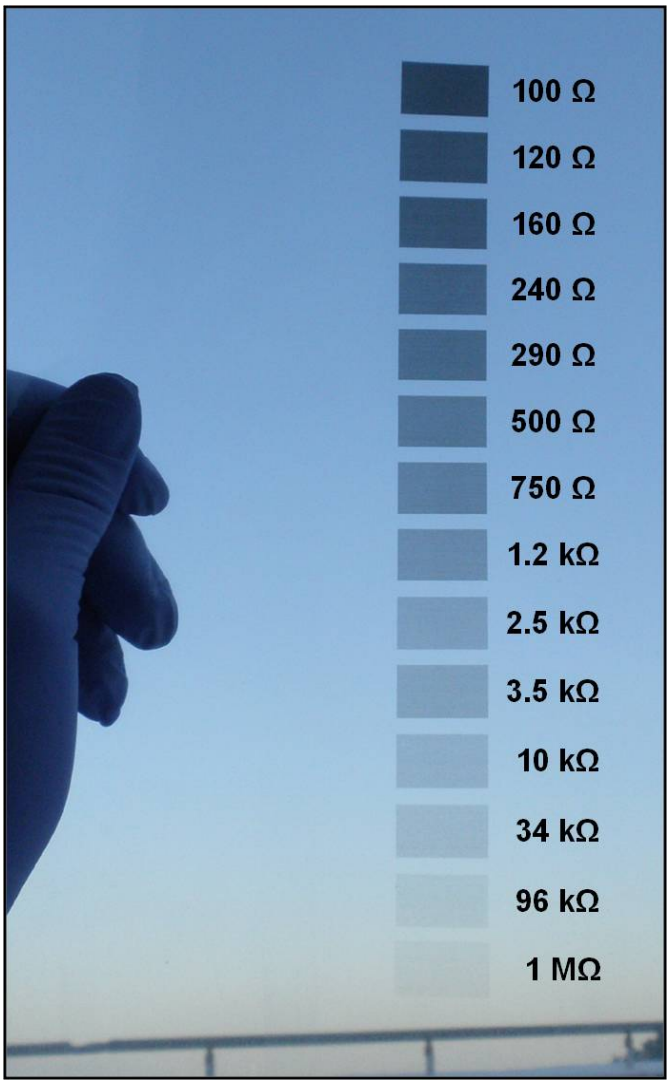

Figure 43. The photo image of gradient patterned graphene sheets with controlled surface resistance as a function of lightness. Grayscale images were designed by computer software.

The surface resistance of patterned graphene sheets is plotted as functions of GO concentration and printing number (Figure 44). To evaluate the electrical characteristics, the surface resistance of patterned graphene sheets was measured by four-probe method. When the printing number and GO concentration increased, the resistances of patterned graphene sheets decreased gradually. After the minimum surface resistance of patterned graphene sheets was obtained by repeat inkjet printing for 30 passes with 0.7 % GO ink, the value of surface resistance was estimated to be *ca.* 65Ω sq^{-1}. From the data, it can be inferred that the surface resistance of the patterned graphene-based thin films exhibits 3-fold reduction compared with that of surfactant-mediated graphene film owing to the insulating property of the additive [112,113].

On the basis of the above analysis, this study has demonstrated for the first time that the graphene-based thin film was able to be applied for electrode of WB radio frequency identification (RFID) antenna. It is wireless communications technology which can transfer large amounts of information over a very wide-band with relative low-power compared to the existing spectrum. The practical dipole antenna composed of two wires was chosen for this implementation [114,115]. Since the bandwidth is determined by the length of the dipole antenna, the length should be 30 cm to fabricate the 500 MHz bandwidth dipole antenna.

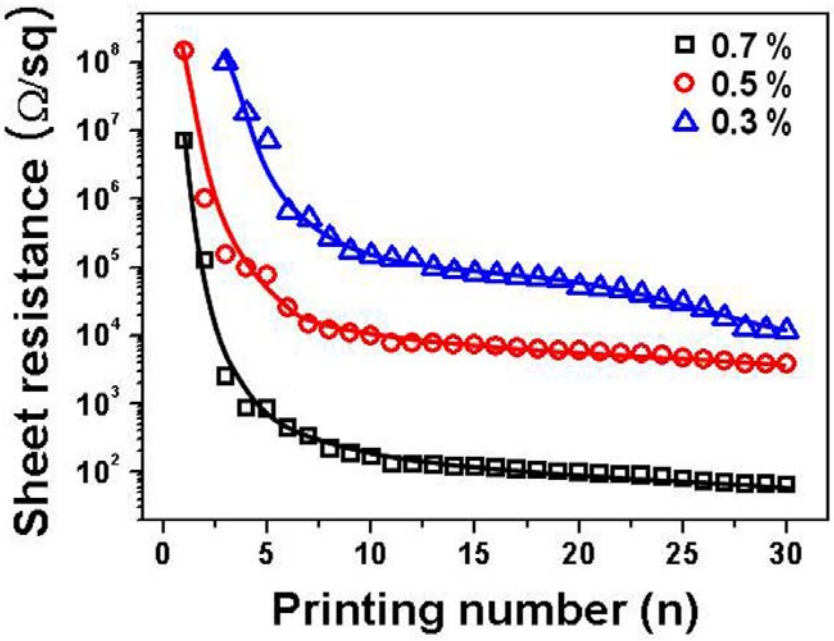

Figure 44. Surface resistance of patterned graphene sheets as functions of the GO concentration and printing number. The surface resistance was measured by four-probe method, and patterned graphene-based thin film has minimum sheet resistance of 65 Ω sq^{-1} (30 times printing with 0.7 % GO ink).

Two key parameters such as bandwidth and voltage standing wave ratio (*VSWR*) or return loss (*RL*) of the antenna have to be considered to evaluate the performance of the designed antenna [116,117]. The bandwidth is basically frequency that the antenna is required to radiate, and the *VSWR* represents that the measure of how efficiently frequency power is transmitted from a power source. A large positive return loss indicates that the reflected power is smaller than the incident power, and implies good impedance matching between source and load.

Figure 45 shows the return loss curve of the dipole antenna using patterned graphene sheets electrode. The bandwidth of simulated *RL* was ranged from 460.4 MHz to 524.8 MHz with respect to 10 dB standard. Furthermore, the *VSWR* and *RL* at the center frequency are displayed in Table 3 and high transmitted power efficiency of 96.7 % is obtained using patterned graphene sheets electrode. The inset photograph indicates a typical Smith chart impedance diagram of the dipole antenna. The chart, the graphical representation of the mathematical properties of a network, is widely used to represent port impedances and *VSWR*. From the data, the impedance point of passband was located near the center of Smith chart. It meant that the smaller return loss was, the closer impedance point located to the center [118].

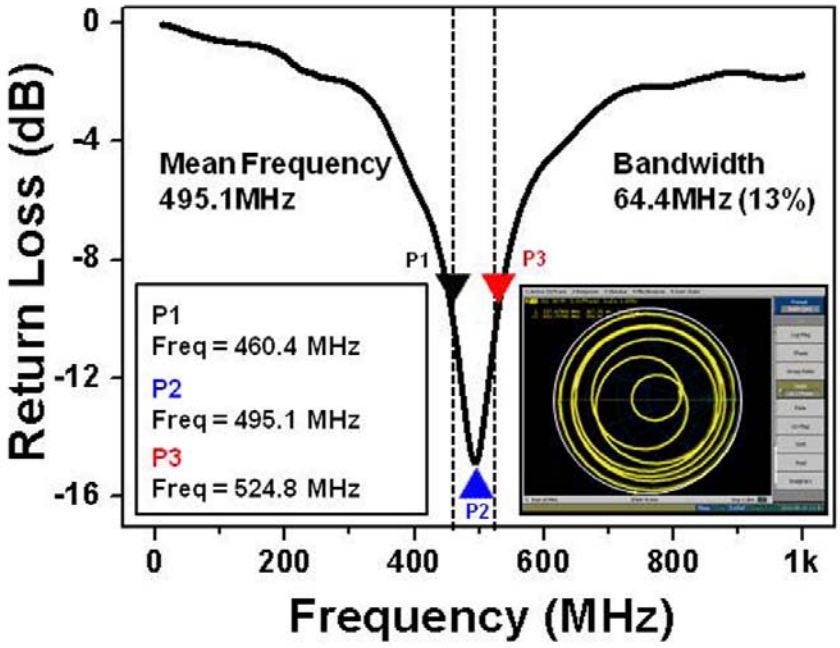

Figure 45. The return loss curve of the dipole antenna application using patterned graphene sheets electrode. (inset: Smith chart impedance diagram of designed dipole antenna).

Table 3. *VSWR* and *RL* of designed dipole antenna by patterned graphene sheets.

VSWR [a]	*RL*	Reflection Coefficeint (Γ)	Transmitted Power	Reflected Power
1.44	14.9	0.144	96.7	3.3

[a] These values were acquired in the E5071B ENA RF Network Analyzer of Agilent Technologies.

3.3.3. Flexible & transparent graphene electrode as an acoustic actuator using inkjet printing

The structure and functional principle of graphene-based PVDF thin film speaker using converse piezoelectric effect was illustrated in Figure 46a. When a time variable voltage (AC electric field) was applied to graphene electrodes on the piezoelectric PVDF film, it could produce the sound wave as attractive and repulsive forces between internal charge and external field were continued to repeat. Figure 46b shows the photograph of the acoustic actuator that consists of graphene-based transducer connected to the sound source and amplifier.

The overall procedure for fabrication of the graphene film onto the PVDF substrate by inkjet printing is illustrated in Figure 47. For fabrication of the graphene film onto the PVDF substrate, exfoliated GO aqueous solution was used as conductive ink, and the thermal annealing for reduction process was performed under vacuum conditions (*ca.* 10^{-3} torr). The hydrophilic property of GO solution could make it possible to overcome the limitations on conductive ink preparation to be printed through a nozzle including optimization of suitable solubility, viscosity and surface tension [119,120]. Furthermore, in order to prevent the deformation of the film and match between surface energy of substrate and surface tension of GO ink (75.2 mNm^{-1}), PVDF film was

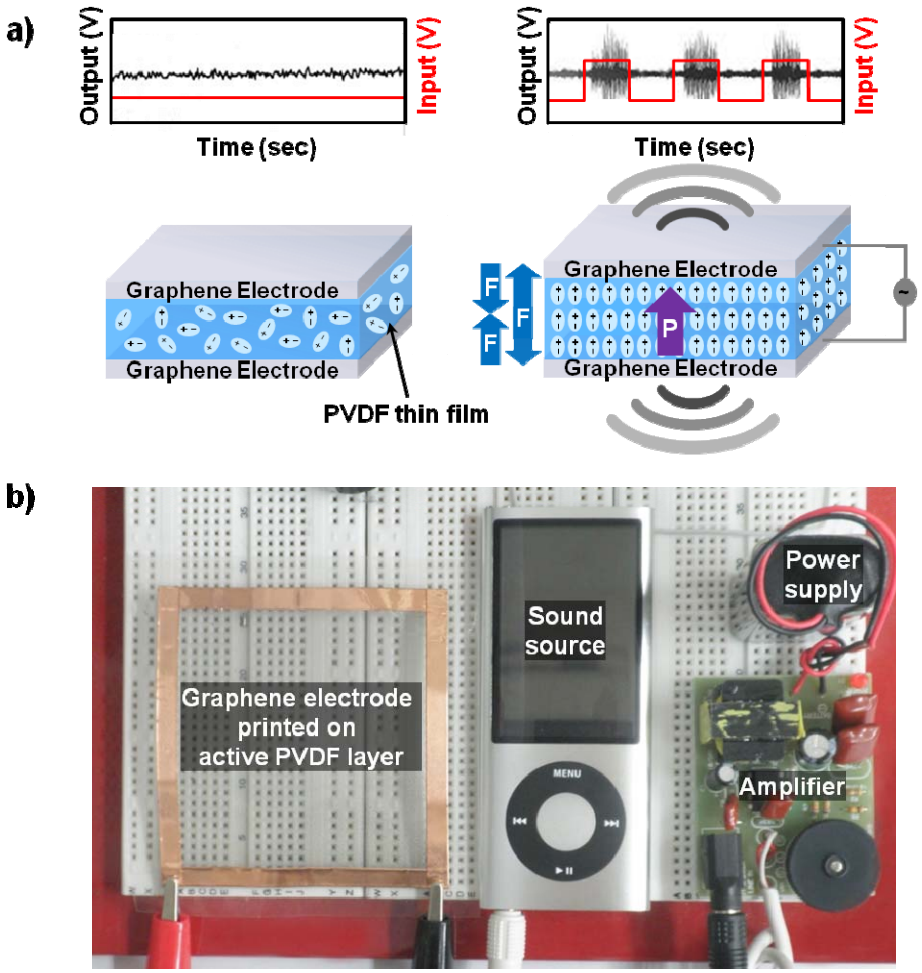

Figure 46. a) Schematic illustration and b) photograph of PVDF-based thin film acoustic actuator using flexible and transparent graphene electrodes. The P and F meant polarization and force of the acoustic actuator, respectively.

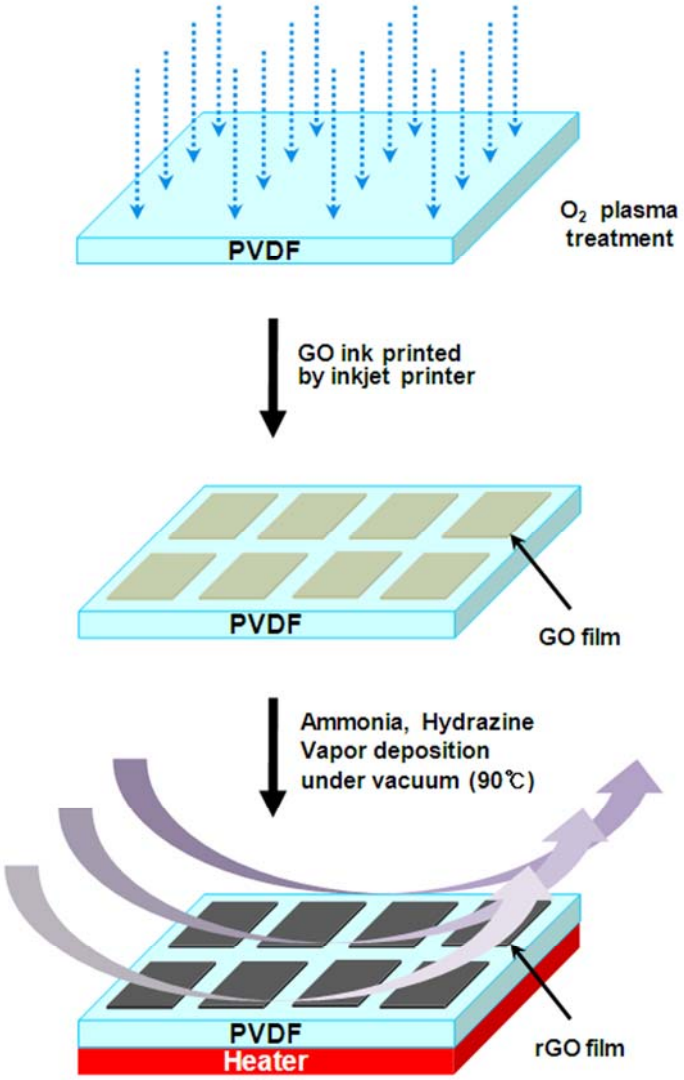

Figure 47. Fabrication of graphene electrodes on PVDF film by inkjet printing and vapor deposition process. The reduction process was performed by mild-thermal annealing at 90 °C with hydrazine and ammonia vapor.

modified with low-temperature oxygen plasma (gas flow rate: 20 sccm, power: 100 W and time: 120 s at 5 ^{o}C) [121,122]. As a result, the surface energy of the film increased from 25.0 mNm^{-1} to 58.7 mNm^{-1}, indicating that the GO ink could be printed out precisely onto the substrate.

To confirm the successful reduction from printed GO to graphene film onto the PVDF substrate, XPS analysis for four different films (pristine PVDF, O_2 plasma modified PVDF, GO film on PVDF substrate and graphene film on PVDF substrate) are conducted (Figure 48). For pristine PVDF film, each main peak of CF_2, CH_2 and C–C bonding appeared at 290.8, 286.2 and 284.5 eV. After the low-temperature O_2 plasma treatment on the PVDF film, the intensity of the CF_2 peak decreased. On the contrary, the C–O component (286.3 eV) from epoxy and hydroxyl groups and the C=O bond (288.5 eV) from carboxy and carbonyl groups had emerged. It could be originated from the defluorination and oxidation of carbon radical occurred on the PVDF surface. When the GO ink was printed out by repeat printing for 10 passes, it was apparent that the CF_2 peak of pristine PVDF film was disappeared. It meant that the PVDF substrate had negligible effect on XPS intensity of GO film. Furthermore, as a result of reduction process for graphene film, the ratio of the I_{C-O}/I_{C-C} decreased from 1.19 (GO) to 0.29 (graphene).

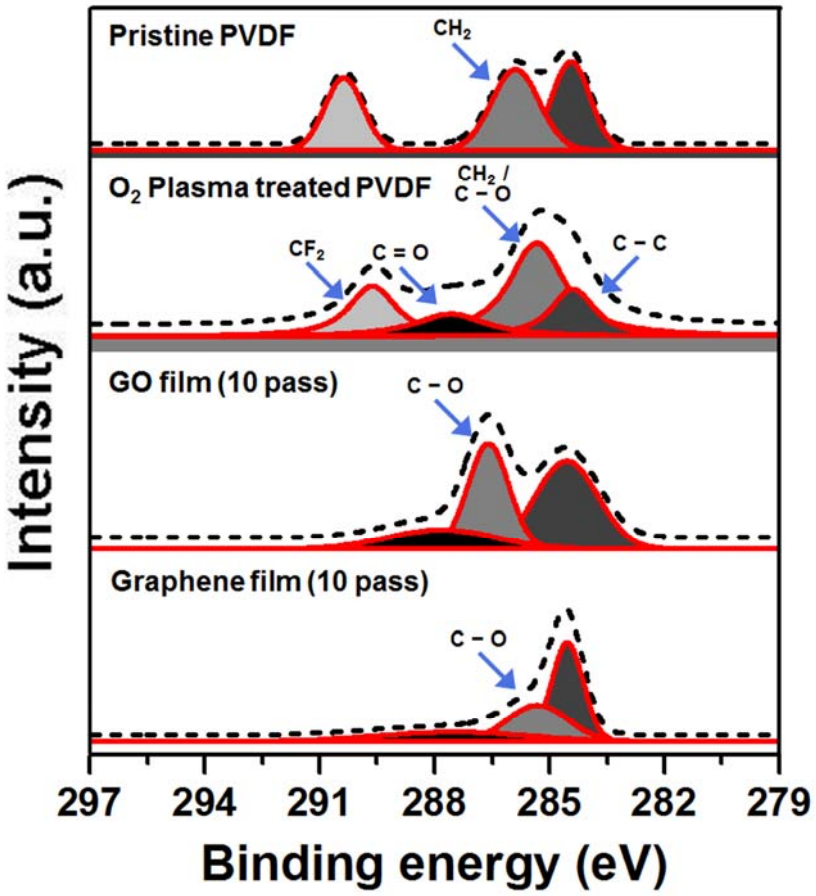

Figure 48. Comparison of deconvoluted XPS spectrum of pristine PVDF, O_2 plasma treated PVDF films, exfoliated GO by inkjet printing for 10 passes and graphene thin films resulted from the reduction procedure onto the PVDF substrate in the C1s region.

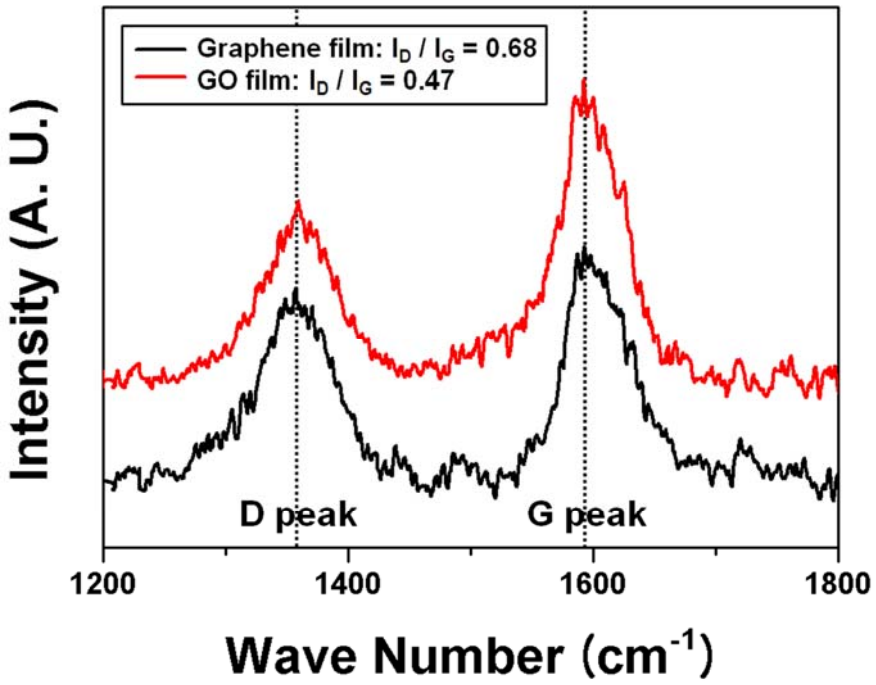

Figure 49. Raman spectra of GO and graphene film on the PVDF substrate showing G and D peaks.

The Raman spectrum of GO and graphene film on the PVDF substrate is exhibited in Figure 49. It is well-known that the G peak (around at 1,586 cm^{-1}) indicates graphite carbon structure, whereas the D peak (around at 1,355 cm^{-1}) means typical defects ascribed to the structural edge effects, such as epoxides covalently bonded to the basal plane. The intensity ratio of I_D/I_G for GO film was 0.47. Furthermore, the Raman spectrum of the graphene film also contained both G and D bands. However, with an increased I_D/I_G intensity ratio (0.68) compared to that in GO. This change suggested a decrease in the average size of the sp^2 domains upon reduction of the exfoliated GO [123]. Judging from these data, it was evident that the printed GO was successfully reduced to graphene film without defect by the hydrazine vapor as a reducing agent.

In order to measure the thickness of graphene thin film, AFM analysis was also carried out. Figure 50 presents that the film thickness increased linearly with increasing printing number, and the average of layer thickness was considered to be *ca.* 15~20 nm. The inserted image was AFM topography of graphene film by inkjet printing for 1 pass which had the observable range of 50 μm. Considering this result, it was proved that graphene thin film consisted of multilayers of graphene. Moreover, the fine tuning of the surface sheet resistance and transmittance was accomplished *via* controlling the number of printing.

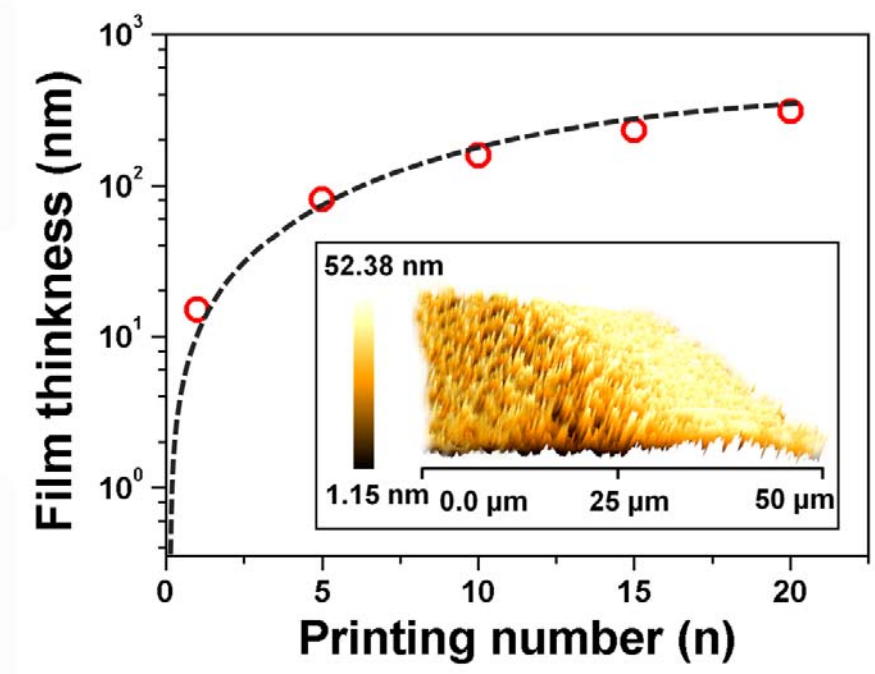

Figure 50. Film thickness of graphene electrodes as a function of the printing number using inkjet printing and reduction process (Inset: AFM image of graphene film acquired by inkjet printing for 1 pass which has observable range of 50 μm).

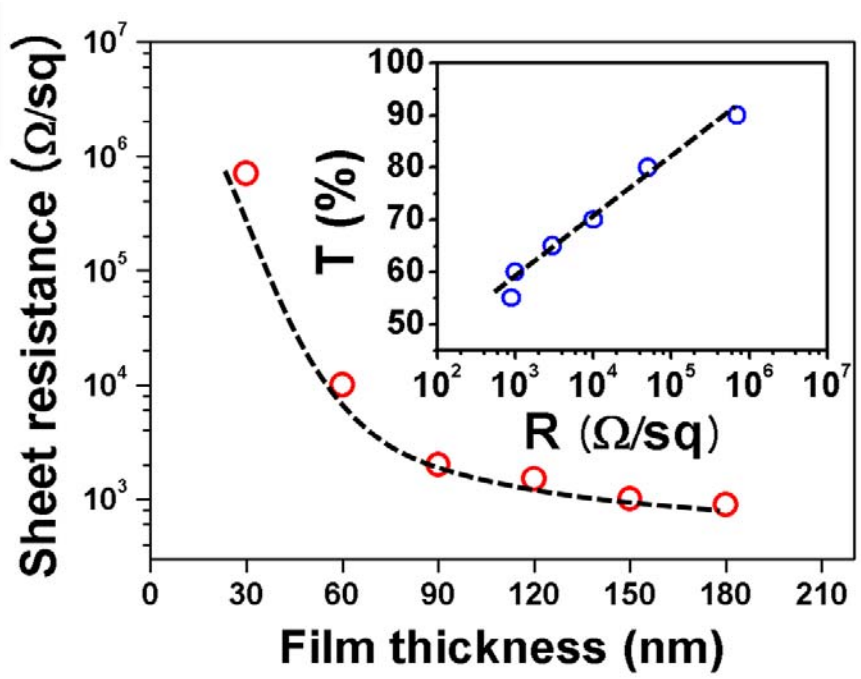

Figure 51. Surface sheet resistances of graphene-based PVDF films with different film thickness (Inset: the data represented by transmittance versus sheet resistance with the same film thickness). The average layer thickness is considered to be *ca*. 15~20 nm.

As shown in Figure 51, the obtained multilayer graphene films on the PVDF substrate had sheet resistances of 700, 10, 2 and 1.5 kΩ sq^{-1} at room temperature and transparencies (defined as transmittance at a wavelength of 550 nm and presented in the inserted graph) of 92.65, 81.85, 72.35 and 66.94 %, respectively. This result implied that the conductivity of graphene film synthesized by reduction process under vacuum was 7 times higher than that without vacuum, though the graphene film on the both sides of PVDF substrate had lower transmittance than that printed on one side of the substrate.

Figure 52 depicts the acoustic response of graphene-based thin film speaker with different electrode thickness (60, 90 and 120 nm) compared to that of PEDOT:PSS-based commercial thin film. In general, the wavelength of substrate is inversely proportional to frequency, while the film thickness is directly proportional to wavelength [124]. Furthermore, an increase of the film thickness could lead to lower surface sheet resistance. For these reasons, the overall frequency responses were enhanced with increasing the film thickness, particularly over the midrange frequency. In addition, the acoustic actuators with graphene electrode had higher responses over all frequencies than those with PEDOT:PSS electrode. In particular, the graphene-based PVDF film with 60 nm thickness had the 10 dB higher response in the treble frequency range than the commercial thin film, which meant that the sound level of the

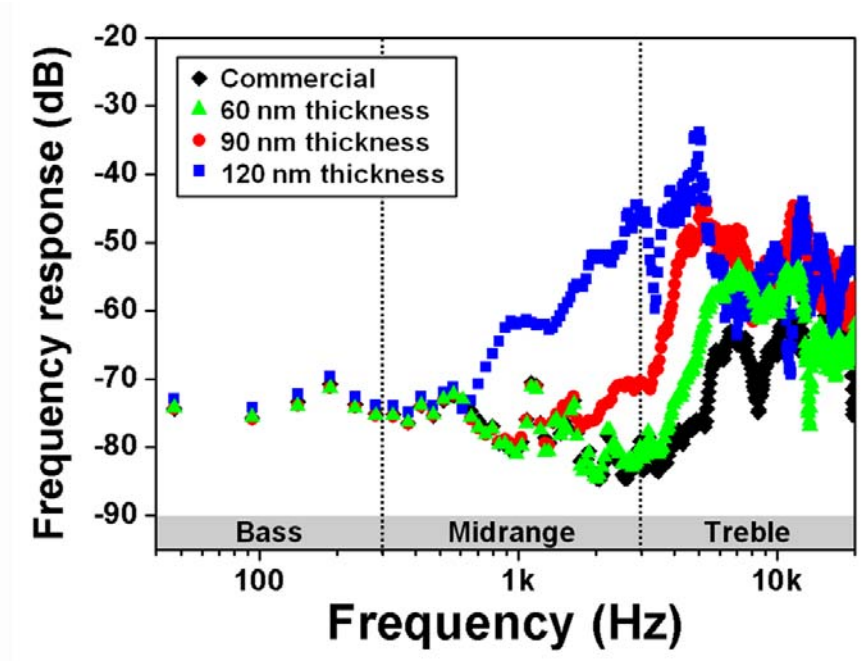

Figure 52. The frequency response of the graphene-based thin film transducer with three different electrode thickness (60, 90 and 120 nm) compared to the PEDOT:PSS-based commercial thin film transducer.

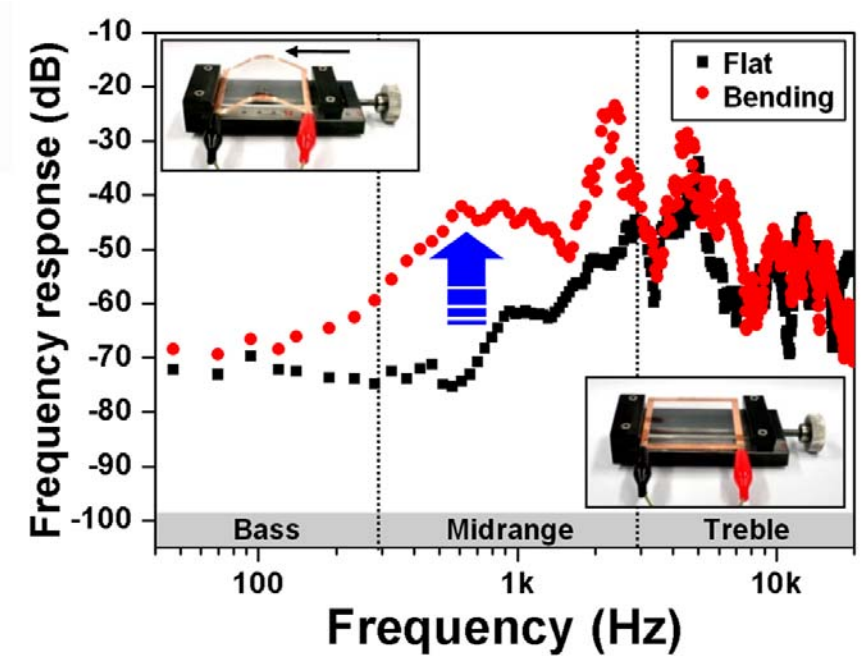

Figure 53. Each frequency response at the flat and bending conditions (radius: 6 cm) of graphene-based thin film transducer with 120 nm electrode thickness.

graphene-based transducer could produce at least 3.1 times higher than that of the commercial transducer at the same driving voltage. Moreover, each frequency response at the flat and bending conditions (radius: 6 cm) of the graphene-based transducer with 120 nm thickness was estimated in Figure 53. It also showed that the frequency response was obviously enhanced in the bass and midrange frequency at the bending condition compared to the flat condition. This result was based on the principle that waves of sound energy could be focused at the bending condition. From the point of view, the graphene-based acoustic actuator was expected to remove the need for expensive high-power voltage amplifiers due to much less power consumption, and be used as a transparent, extremely thin and lightweight loudspeaker.

It was also found that the performance of the graphene-based acoustic actuator could be optimized for adaptive noise cancellation (ANC) application which was achieved by introducing a cancelling anti-noise wave of both equal amplitude and opposite phase using a soft substrate. The important effect of the soft substrate was that could help to eliminate the nonlinear harmonics of the graphene-based acoustic actuator. As a result of the 3 kHz tonal signal input, the graphene-based transducer without soft substrate generated harmonic sounds at multiples of 3 kHz (Figure 54). However, the spectrum of graphene-based transducer with soft substrate had attenuated harmonics of 6~21 kHz due

to the added damping and amplified 3 kHz frequency response which was considered as desired tonal signal. This finding provides new possibility for ANC application.

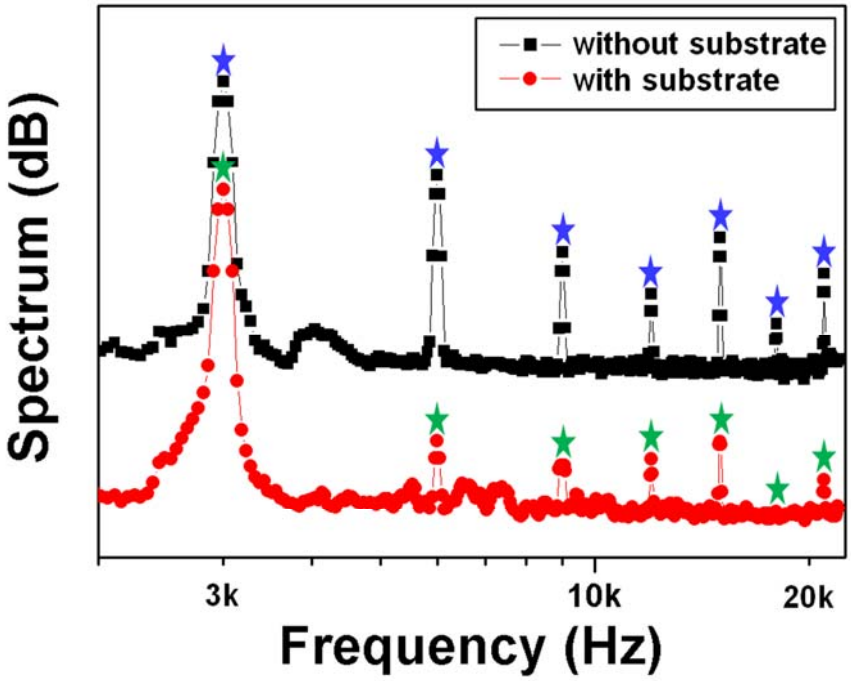

Figure 54. The ANC effect on the harmonics of graphene-based thin film transducer from 3 kHz tonal signal. A soft substrate (3M VHB4910 acrylic form tape) was cleaved to the film to make an ANC actuator (stars indicate harmonic sounds at multiples of 3 kHz).

3.3.4. Electrorheological properties of graphene suspensions with improved sedimentation stability

The ability to control rheological characteristic is important in many technological applications. Various approaches for controlling the rheological property have been developed. In particular, ER fluids have received much attention due to their unique rheological features [125–127]. The ER fluids have received considerable attention due to its several attractive features, such as simple mechanics, low power consumption, rapid response time, and reversibility [128–131].

As mentioned it above, graphene has attracted a great deal of interest because of their fascinating properties different from those of the carbon-based materials (*e.g.*, extremely high charge carrier mobility, large specific surface area, thermal/electrical conductivity, and chemical & mechanical stability). In particular, GO could be regarded as an oxidation state of graphene. The GO has the hydroxyl, carboxylic, and epoxide oxygen functional groups on the basal planes and edges, and can be expected to give good dispersion stability in aqueous and other organic solvents. In addition, the GO can be adopted as ER materials without any post-treatment as a result of its insulated conjugated structure.

Up to date, diverse synthetic strategies toward fabricating graphene-based

ER materials have been developed, including GO sheets, GO/polyaniline (PANI) nanocomposite, GO/TiO_2 nano-composite, graphene/chitosan nano-composite, graphene coated polystyrene (PS), and so forth [132–135]. However, previous researches are still in the very early stages of commercialization in terms of complicated procedures, electrical breakdown at high electrical field, and insufficient shear strength. Furthermore, they had the important drawbacks of low colloidal stability and a tendency to sediment, which could limit their practical or industrial applications. Therefore, it is still challenging to develop efficient and facile strategy for dispersing GO sheets in silicone oil and a more simple alternative method is desired.

In this study, a reliable approach for preparing GO sheet-based ER fluids with anti-sedimentation properties is proposed. The ER activity of GO-based ER fluids were investigated as functions of shear rate, electric field strength, and a weight fraction GO sheets. In addition, the sedimentation stability of the ER fluids was also examined.

The overall procedure for fabricating two different types of GO sheet-based ER fluids is illustrated in Figure 55. In dispersion state, isolated GO sheets existed in ethanol medium. However, isolated GO sheets aggregated and stacked into a layered structure like graphite in dry state. Once the medium solvent is removed by drying, the π–π attractions become dominant and the

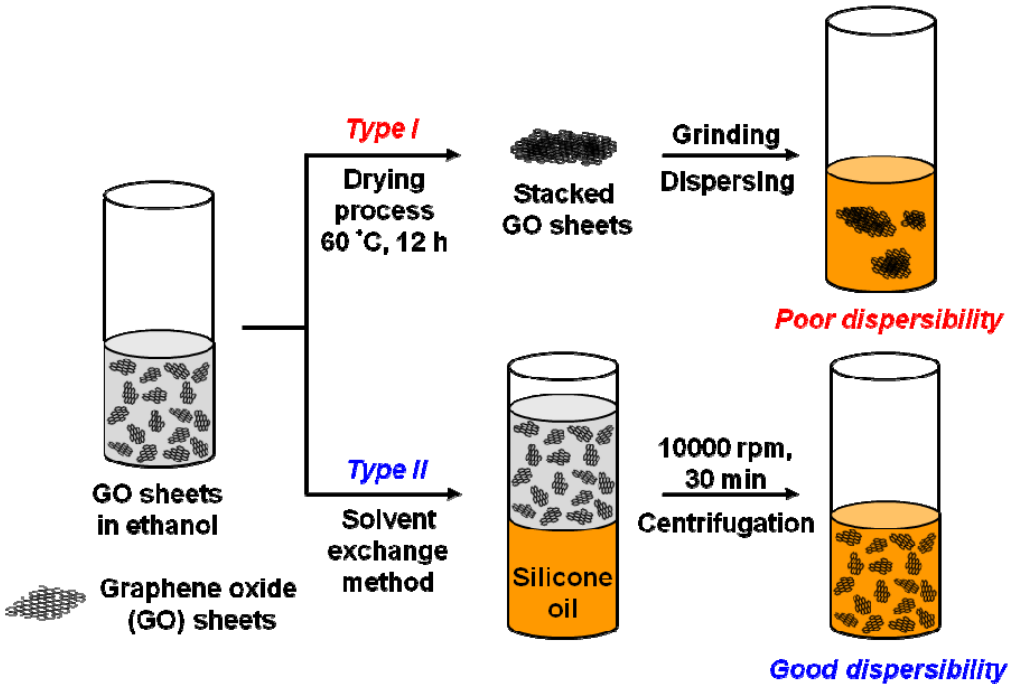

Figure 55. Schematic illustration of the different steps for fabricating GO sheet-based ER fluids.

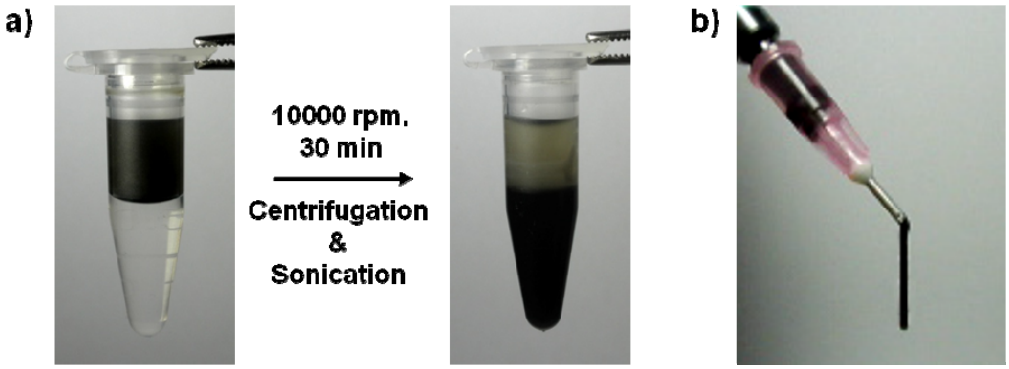

Figure 56. a) Photographs of the GO sheet-based ER fluid prepared by centrifugation of dispersion of GO sheets in ethanol (upper phase) and silicone oil (lower phase). b) Extrusion of the GO sheet-based ER fluid from a needle.

formed structure is not recoverable [136,137]. Consequently, the enhanced intersheet π–π interaction makes it difficult for the stacked GO sheets to re-disperse in silicone oil [poly(methylphenylsiloxane), viscosity = 100 cSt] (*Type I*). However, isolated GO sheets can form relatively stable high concentration dispersion in silicone oil using a solvent exchange process from ethanol medium. It is noteworthy that this technique ensures that the high specific surface area as well as other unique properties exhibited by GO sheet is retained in silicone oil (*Type II*). In addition, the GO sheet-based ER fluid thus obtained can readily be processed. For example, via extrusion from a syringe, one can fabricate cables exhibits properties of physical gels (Figure 56).

Prior to the preparation of the ER fluid, the electrical conductivity of the synthesized GO sheet was measured by a four-probe method. Generally, suitable conductivity of ER material is typically less than 1×10^{-6} S cm^{-1} [138]. In our experiment, the conductivity of the GO sheet was measured to be ca. 1.0×10^{-7} S cm^{-1}. This conductivity value is sufficient for an ER application without any post-treatment. The off-field viscosity of dispersion increases with increasing intermolecular forces between dispersing materials. In dispersion state, well-dispersed isolated GO sheets produce larger particle-particle interaction between GO sheets than flocculated or agglomerated GO sheets at equal GO concentration (Figure 57). Therefore, the solvent exchanged GO

sheet-based ER fluid has a relatively high off-field viscosity. The off-field viscosity value of solvent exchanged GO sheets is *ca.* 0.513 Pa·s, which is 2.1 times that of mechanically grinded GO sheets (Table 4).

To evaluate the real-time responses of two different types of GO sheet-based ER fluids, applied electric fields (1, 3, and 5 kV mm^{-1}) were alternately turned on and off, and their shear stress values were monitored in real time (Figure 58). When the electric field was applied, the shear stress values of both mechanically grinded GO sheets and solvent exchanged GO sheets increased instantaneously. In contrast, the shear stress values dropped rapidly back to their original level when the electric field was turn off. This result indicates that the responses of the GO sheet-based ER fluids, upon the application of an electric field, are reversible and reproducible.

However, two different types of GO sheet-based ER fluids displayed significantly different ER activity in terms of their ER efficiency (defined as $(\tau_E - \tau_0)/\tau_0 \times 100$ or $\Delta\tau/\tau_0 \times 100$, where τ_E is the shear stress with an applied electric field strength and τ_0 is the shear stress without an electric field strength). When the shear rate reaches to 100 s^{-1}, the solvent exchanged GO sheets provided consistently higher ER efficiency than that of mechanically grinded GO sheets and the corresponding ER efficiencies were about 207 and 67 %, respectively (Figure 59).

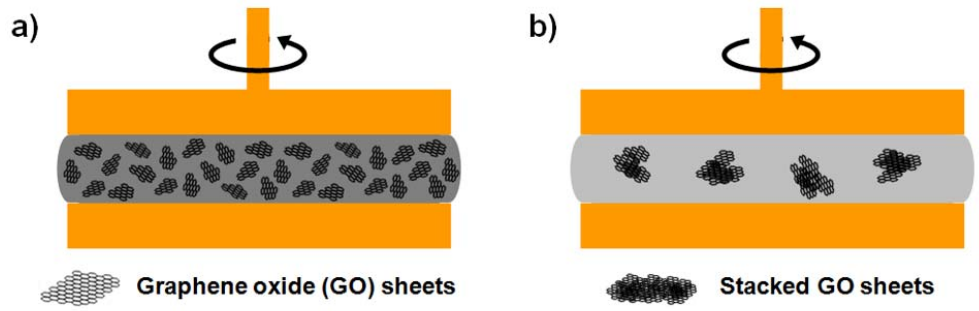

Figure 57. Schematic illustration for the dispersing state of (a) solvent exchanged GO sheets and (b) mechanically grinded GO sheets.

Table 4. Off-field viscosity of GO sheets in silicone oil.

	Silicone oil [a]	Mechanically grinded GO sheets	Solvent exchanged GO sheets
Off-field viscosity [b]	0.097 Pa·s	0.245 Pa·s	0.513 Pa·s

[a] The silicone oil (Aldrich, poly(methylphenylsiloxane), viscosity = 100 cSt) was used as a dispersing medium. [b] These values were obtained using rheometer (AR 2000 Advanced Rheometer, TA Instruments) at a standard temperature of 20 ºC.

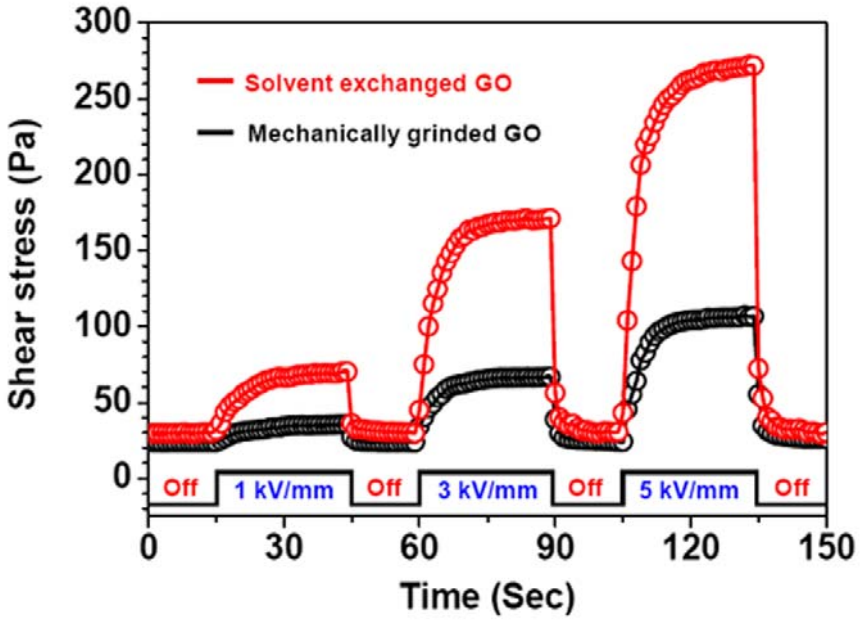

Figure 58. Effect of switching the applied electric field on the shear stress of the GO sheet-based ER fluids (5 wt% in silicone oil).

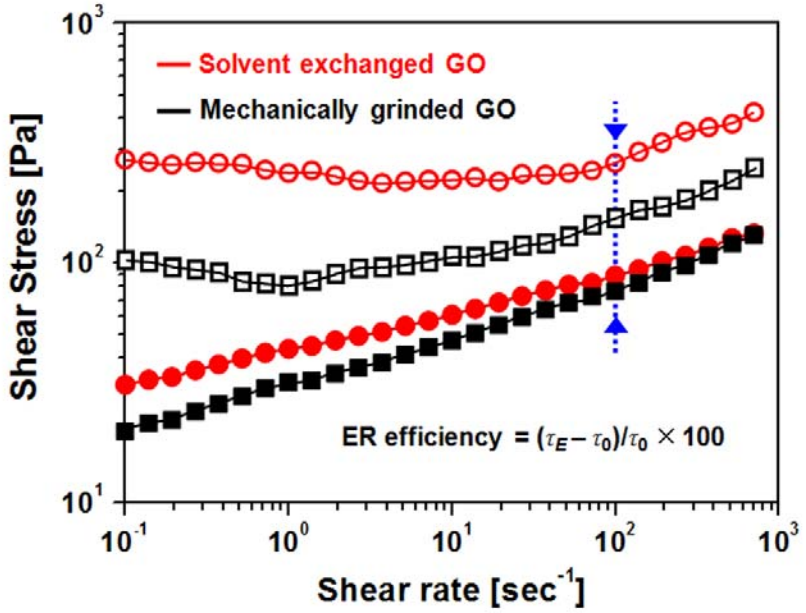

Figure 59. Shear stress for the 5 wt% of GO sheet-based ER fluids under electric field strength (5 kV mm^{-1}). Open and closed symbols indicate with and without electric field strengths, respectively.

A possible explanation of the difference in the ER efficiencies may reside with the surface area of GO sheets. It is noted that the solvent exchanged GO sheets can possess a high surface area compared with the mechanically grinded GO sheets. The high surface area provides sufficient electrostatic interaction to counteract the hydrodynamic inter-action under shear flow [139].

To gain an insight into the ER activity of GO sheet-based ER fluids, the influence of the GO weight fraction (ω) on the dynamic yield stress was evaluated in the viewpoint of volume fraction of ER fluids in the ω = 1–5 wt% range (Figure 60). The dynamic yield stress value of solvent exchanged GO gradually increased with increasing particle weight fraction. The dynamic yield stress value of solvent exchanged GO is ca. 270 Pa at 5 wt%, which is 15 times that of identical ER materials at 1 wt%. This dramatic increment in the yield stress may be attributed to the enhanced interparticle interactions. At high particle weight fraction, this particle interaction between polarized ER materials will undoubtedly lead to substantially different mechanical rigidities, which resist deformation in shear flow. Consequently, the solvent exchanged GO sheets with a high surface area represent typical Bingham fluid behavior and enhanced ER activity in an extremely low concentration of GO sheets (<1 wt%).

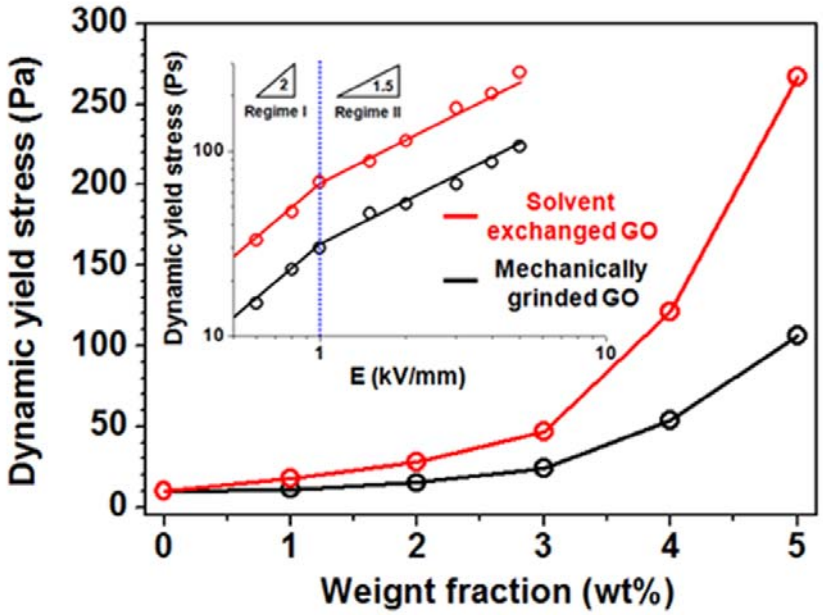

Figure 60. Dynamic yield stress as a function of weight fraction for the GO sheet-based ER fluids under 5 kV/mm of electric field [inset: Dynamic yield stress of various GO sheet-based ER fluids as a function of electric field strength (5 wt% in silicone oil)].

The relationship between the yield stress (τ_y) and the electric field strength is also investigated (Figure 60 inset). When the ω is fixed, the ER properties show the dependence on the electric field strengths. Similar to most ER fluids, the yield stress values of ER fluids is directly proportional to the increase in the applied electric field strength. In our experimental condition, the GO sheet-based ER fluid exhibited that τ_y is proportional to E_0^2 at low E_0 (under 1 kV/mm) and typically approaches $E_0^{3/2}$ at high E_0 , as shown in Fig. 2b inset. This phenomenon is because of the reinforced fibrous structures due to the enhanced electrostatic interaction under high electric field strengths [140,141]. In addition, high surface area resulting from the enhanced dispersibility also contributed to the enhanced ER activity by synergistic effect.

A microstructural transition of GO-based ER fluid was observed using an optical microscope (OM) under an applied electric field as shown in Figure 61. Randomly dispersed GO sheets began to move rapidly toward the electrodes (within 100 milliseconds) and then formed a fibrillated structure along the applied electric field direction. The aligned fibrous structure, which is dominated by sufficient electrostatic interaction between GO sheets, provides rapid structure reformation under a shear force as well as a better resistance to the shear flow.

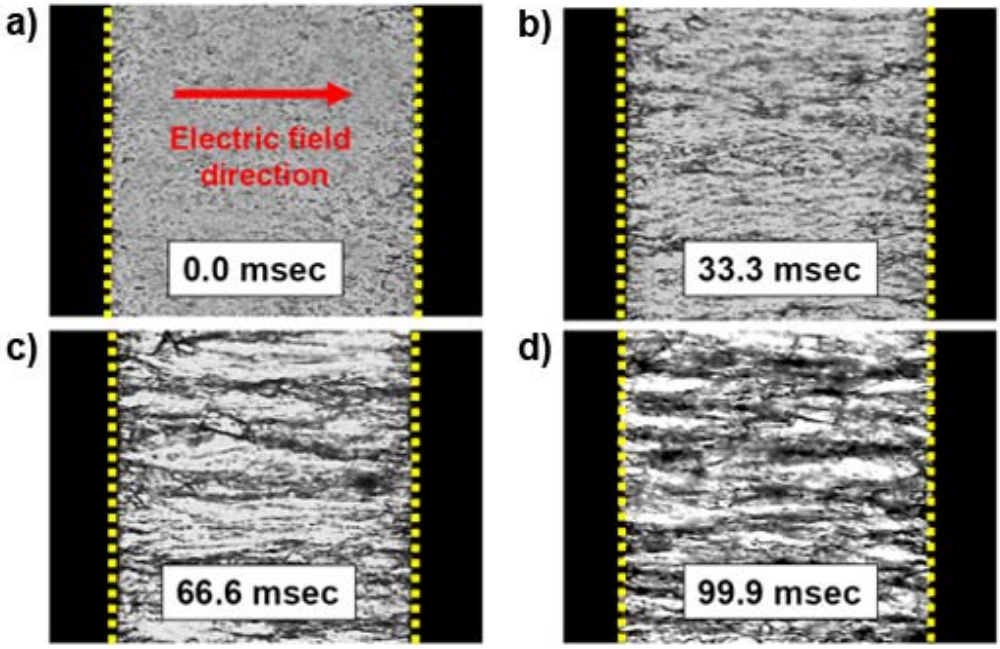

Figure 61. (a-d) Microscope images of chain formation in silicone oil suspension of GO (5 wt % in silicone oil) under an applied electric fields of 1 kV mm^{-1}. The gap between two electrodes was fixed to 1.0 mm.

In particular, the solvent exchanged GO dispersed in silicone oil (1 wt%) exhibited a superior sedimentation ratio compared to that of the mechanically grinded GO as well as the other conventional ER fluids. In Figure 62, the solvent exchanged GO sheets provide excellent anti-settling properties (looks like "ink"). There is no sediment deposited after ninety days. This predominant dispersion stability can be ascribed in terms of the sedimentation velocity. The sedimentation velocity is regarded as important factor in particle precipitation [142,143]. The Stoke's law is a formula for determining the rate of sedimentation. It states that a particle movement through viscous liquid attains a constant velocity or sedimentation rate. The equation for Stoke's law of sedimentation is as follows:

$$V_g = d^2(\rho_p - \rho_l) / 18\eta \times G$$

Where, V_g is sedimentation velocity, d is particle diameter, ρ_p is particle density, ρ_l is liquid density, η is viscosity of liquid, and G is gravitational acceleration. Under our experimental condition, the sedimentation velocity (V_g) was estimated using the Stoke's settling equation and was found to be 3.8×10^{-7} and 6.1×10^{-4} m s^{-1} for solvent exchanged GO sheets and mechanically grinded GO sheets, respectively (Table 5). It is noteworthy that the V_g value of solvent exchanged GO sheets is *ca.* 1600 times slower than that of mechanically grinded GO sheets. It is also expected that the retarded settling velocity of

isolated GO sheet and the electrostatic repulsion between oxygen functional groups on GO sheets would have a combined or synergistic effect on the enhancement in anti-sedimentation property.

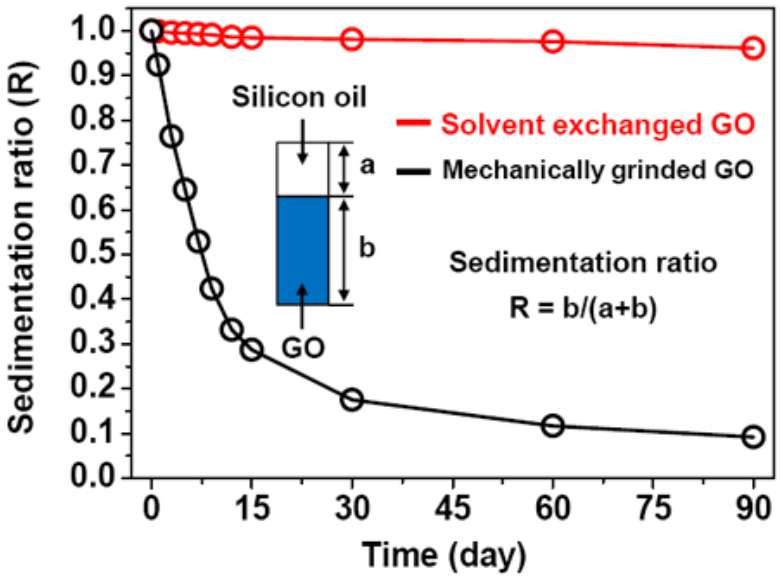

Figure 62. Sedimentation properties of two different types of GO sheet-based ER fluids (1 wt% in silicone oil) [inset: definition of sedimentation ratio].

Table 5. Physical parameters and sedimentation velocity of GO sheets in silicone oil.

	Solvent exchanged GO sheets	Mechanically grinded GO sheets
Particle size [a]	*ca.* 20 μm	*ca.* 300 μm
Particle density [b]	1.14 g cm^{-3}	2.17 g cm^{-3}
Fluid density [c]	0.97 g cm^{-3}	0.97 g cm^{-3}
Fluid viscosity [c]	0.097 Pa·s	0.097 Pa·s
Sedimentation velocity [d]	0.00000038 m s^{-1}	0.00060680 m s^{-1}

[a] The average particle size was determined by SEM (50 particles counted), [b] Particle density was obtained using density hydrometer at a standard temperature of 20 ºC, [c] Silicone oil [poly(methylphenylsiloxane), viscosity = 100 cSt] was used as a dispersing medium, [d] The calculation method used was Stoke's settling equation. Particle Reynolds number less than 0.2.

4. CONCLUSIONS

1. The graphene discs with well-defined shape were successfully fabricated using a simple oxidation and exfoliation process of high-crystalline CNFs. To control the shapes of graphene, two different types of CNFs (platelet and herringbone type) were used as starting materials. Interestingly, the diameter and shape of the graphene discs could be controlled by selectively designing the morphology of starting materials and optimizing the cutting method.
2. A mechanical reduction method for graphene oxide was proposed in order to combine the high recovery of π-conjugated electronic structure with the solution processability of graphene discs. The reduced graphene discs could be formed without any additives such as reducing agent and were highly dispersed in different solvents with high content of graphene discs.
3. A simple and effective method for graphene nanosheets was demonstrated using LbL self-assembly approach with a metallic dopant. The PAA/PSS multi-layers prepared by LbL method were successfully transformed into graphene nanosheets. During the carbonization process, the PSS layers could be transformed into graphene nanosheets due to its inherent aromatic and highly ordered structure. PAA layers served to protect the structural layers as well as prevent the agglomeration of graphene nanosheets. Most

importantly, the metallic dopant played a pivotal role in the formation of graphene nanosheets during the carbonization process.

4. Flexible graphene film was obtained by vacuum filtration of this dilute graphene suspension using AAO membrane and wet-transferred to a PET film. As-prepared graphene-based films represented excellent opto-electronic properties (high optical transparency and low sheet resistance), and provided potential applications as a transparent electrode.
5. A simple and effective strategy to pattern the graphene nanosheets was demonstrated using an inkjet printing method. The graphene nanosheets consisted of a few layers were successfully patterned on PET film with high resolution, and the fine tuning of the sheet resistance was achieved *via* gradient patterning. Furthermore, it could be also simply controlled by varying concentration of GO ink and the number of printing.
6. The graphene-based thin film could be used as an electrode for WB antenna. The graphene sheets- based WB dipole antenna was implemented with 500 MHz bandwidth and high transmitted power efficiency of 96.7 %, and it can be applied for signal receiving apparatus such as RFID tag, airport passenger screening detecting nearby objects and body sensor network using Medical Implant Communication Service (MICS) band.

7. A simple and effective strategy to fabricate flexible and transparent graphene thin film as an acoustic actuator electrode was demonstrated using inkjet printing and VDP method. Most of all, the ability to design shape and size by inkjet printing is expected to offer a great feasibility to give the thin film acoustic actuator various and improved stereo height and width, which is able to produce the sound from everywhere over a large-size panel.
8. A novel and facile dispersion technique based on solvent exchange method was introduced in order to investigate the electro-responsive characteristic of GO sheet. The solvent exchanged GO sheets exhibited consistently higher ER efficiency than that of mechanically grinded GO sheets. It has been known that the sufficient electrostatic interaction originated from high surface area of isolated GO sheets played a dominant role in enhancing the performance of ER fluid and represented ER activity in an extremely low concentration of GO sheets (< 1 wt%). Furthermore, prepared GO sheet-based ER fluids represented excellent anti-sedimentation properties, and provided the feasible candidate for their practical or industrial applications.

In summary, two different ways in the synthetic methodology of shape-controlled graphene were demonstrated in the viewpoint of top-down approach and bottom-up approach. As a ‘top-down approach’, the graphene sheets with well-defined shape were successfully fabricated using a simple oxidation and exfoliation process of high-crystalline CNFs. Interestingly, the diameter and shape of the graphene sheets could be controlled by selectively designing the morphology of starting materials and optimizing the cutting method. As a ‘bottom-up approach’, graphene sheets were formed using LbL self-assembly approach. The well-defined graphene sheets were obtained with the assistance of metallic dopant at a mild carbonization condition. This novel strategy does not require a high carbonization temperature and pressure, and the simple process can be used as an alternative tool for the fabrication of various carbon-based nanomaterials with rational nanostructure design.

The shape-controlled graphene sheets have been successfully applied in a wide variety of applications, suggesting that these nanomaterials may be potentially very useful in many new types of applications related to electronic/optoelectronic devices, conductive nanocomposites, actuators, catalytic supports, and energy storage/conversion systems.

REFERENCES

[1] J. H. Chen, C. Jang, S. Xiao, M. Ishigami, M. S. Fuhrer, *Nature Nanotech*, **2008**, *3*, 206.

[2] A. K. Geim, P. Kim, *Scientific American*, **2008**, *298*, 90.

[3] K. S. Novoselov, A. K. Geim, S. V. Morozov, D. Jiang, Y. Zhang, S. V. Dubonos, I. V. Grigorieva, A. A. Firsov, *Science*, **2004**, *306*, 666.

[4] A. B. Kuzmenko, E. V. Heumen, F. Carbone, D. V. D Marel, *Phys. Rev. Lett.*, **2008**, *100*, 117401.

[5] M. I. Katsnelson, *Materials Today*, **2007**, *10*, 20.

[6] A. K. Geim, K. S. Novoselov, *Nature Mater.*, **2007**, *6*, 183.

[7] D. R. Dreyer, R. S. Ruoff, C. W. Bielawski, *Angew. Chem. Int. Ed.*, **2010**, *49*, 9336.

[8] N. D. Mermin, *Phys. Rev.*, **1968**, *176*, 250.

[9] M. S. Dresselhaus, G. Dresselhaus, *Adv. Phys.*, **1981**, *30*, 139.

[10] V. H. P. Boehm, A. Clauss, G. O. Fischer, U. Hofmann, *Z. Naturforschg.*, **1962**, *17*, 150.

[11] H. P. Boehm, R. Setton, E. Stumpp, *Carbon*, **1986**, *24*, 241.

[12] H. P. Boehm, R. Setton, E. Stumpp, *Pure Appl. Chem.*, **1994**, *66*, 1893.

[13] P. M. Stefan, M. L. Shek, I. Lindau, W. E. Spicer, L. I. Johansson, F. Herman, R. V. Kasowski, G. Brogen, *Phys. Rev. B*, **1984**, *29*, 5423.

[14] T. Aizawa, R. Souda, S. Otani, Y. Ishizawa, C. Oshima, *Phys. Rev.*

Lett., **1990**, *64*, 768.

[15] A. Nagashima, K. Nuka, H. Itoh, T. Ichinokawa, C. Oshima, S. Otani, *Surf. Sci.*, **1993**, *291*, 93.

[16] C. Oshima, E. Bannai, T. Tanaka, S. Kawai, *Jpn. J. Appl. Phys.*, **1977**, *16*, 965.

[17] R. Rosei, M. De Crescenzi, F. Sette, C. Quaresima, A. Savoia, P. Perfetti, *Phys. Rev. B*, **1983**, *28*, 1161.

[18] N. A. Kholin, E. V. Rut'kov, A. Y. Tontegode, *Surf. Sci.*, **1984**, *139*, 155.

[19] N. R. Gall, S. N. Mikhailov, E. V. Rut'kov, A. Y. Tontegode, *Sov. Phys. Solid State*, **1985**, *27*, 1410.

[20] H. Zi–Pu, D. F. Ogletree, M. A. Van Hove, G. A. Somorjai, *Surf. Sci.*, **1987**, *180*, 433.

[21] A. J. Van Bommel, J. E. Crombeen, A. Van Tooren, *Surf. Sci.*, **1975**, *48*, 463.

[22] C. Berger, Z. M. Song, T. B. Li, X. Li, A. Y. Ogbazghi, R. Feng, Z. T. Dai, A. N. Marchenkov, E. H. Conrad, P. N. First, W. A. de Heer, *J. Phys. Chem. B*, **2004**, *108*, 19912.

[23] Y. Zhang, J. Small, W. Pontius, P. Kim, *Appl. Phys. Lett.*, **2005**, *86*, 073104.

[24] D. D. L. Chung, *J. Mater. Sci.*, **1987**, *22*, 4190.

[25] X. Lu, M. Yu, H. Huang, R. Ruoff, *Nanotechnology*, **1999**, *10*, 269.

[26] P. Blake, E. W. Hill, A. H. Castro Neto, K. S. Novoselov, D. Jiang, R. Yang, T. J. Booth, A. K. Geim, *Appl. Phys. Lett.*, **2007**, *91*, 063124.

[27] C. Soldano, A. Mahmood, E. Dujardin, *Carbon*, **2010**, *48*, 2127.

[28] X. L. Li, G. Y. Zhang, X. D. Bai, X. M. Sun, X. R. Wang, E. G. Wang, H. J. Dai, *Nat. Nanotechnol.*, **2008**, *3*, 538.

[29] Y. Hernandez, V. Nicolosi, M. Lotya, F. M. Blighe, Z. Sun, S. De, I. T. McGovern, B. Holland, M. Byrne, Y. K. Gun'ko, J. J. Boland, P. Niraj, G. Duesberg, S. Krishnamurthy, R. Goodhue, J. Hutchison, V. Scardaci, A. C. Ferrari, J. N. Coleman, *Nat. Nanotechnol.*, **2008**, 3, 563.

[30] J. S. Moon, D. Curtis, M. Hu, D. Wong, C. McGuire, P. M. Campbell, G. Jernigan, J. L. Tedesco, B. VanMil, R. Myers-Ward, C. J. Eddy, D. K. Gaskill, *IEEE Electron. Device Lett.*, **2009**, *30*, 650.

[31] O. C. Compton, S. T. Nguyen, *Small*, **2010**, *6*, 711.

[32] S. Park, J. An, I. Jung, R. D. Piner, S. J. An, X. Li, A. Velamakanni, R. S. Ruoff, *Nano Lett.*, **2009**, *9*, 1593.

[33] M. A. Rafiee, J. Rafiee, Z. Wang, H. Song, Z.-Z. Yu, N. Koratkar, *ACS Nano*, **2009**, *3*, 3884.

[34] Y. Shao, J. Wang, M. Engelhard, C. Wang, Y. Lin, *J. Mater. Chem.*,

2010, *20*, 743.

[35] L. J. Cote, R. Cruz-Silva, J. Huang, *J. Am. Chem. Soc.*, **2009**, *131*, 11027.

[36] V. Strong, S. Dubin, M. F. El-Kady, A. Lech, Y. Wang, B. H. Weiller, R. B. Kaner, *ACS Nano*, **2012**, *6*, 1395.

[37] S. Guo, S. Dong, *Chem. Soc. Rev.*, **2011**, *40*, 2644.

[38] W. A. de Heer, C. Berger, X. Wu, M. Sprinkle, Y. Hu, M. Ruan, J. A. Stroscio, P. N. First, R. Haddon, B. Piot, C. Faugeras, M. Potemski, J.-S. Moon, *J. Phys. D: Appl. Phys.*, **2010**, *43*, 374007.

[39] J. Hass, W. A. de Heer, E. H. Conrad, *J. Phys.: Condens. Matter*, **2008**, *20*, 323202.

[40] V. Y. Aristov, G. Urbanik, K. Kummer, D. V. Vyalikh, O. V. Molodtsova, A. B. Preobrajenski, A. A. Zakharov, C. Hess, T. Haenke, B. Buechner, I. Vobornik, J. Fujii, G. Panaccione, Y. A. Ossipyan, M. Knupfer, *Nano Lett.*, **2010**, *10*, 992.

[41] J. D. Caldwell, T. J. Anderson, J. C. Culbertson, G. G. Jernigan, K. D. Hobart, F. J. Kub, M. J. Tadjer, J. L. Tedesco, J. K. Hite, M. A. Mastro, R. L. Myers-Ward, C. R. Eddy, P. M. Campbell, D. K. Gaskill, *ACS Nano*, **2010**, *4*, 1108.

[42] Y. Dedkov, A. Shikin, V. Adamchuk, S. Molodtsov, C. Laubschat, A.

Bauer, G. Kaindl, *Phys. Rev. B*, **2001**, *64*, 035405.

[43] P. W. Sutter, J.-I. Flege, E. A. Sutter, *Nat. Mater.*, **2008**, *7*, 406.

[44] Y. S. Dedkov, M. Fonin, C. Laubschat, *Appl. Phys. Lett.*, **2008**, *92*, 052506.

[45] S. Bae, H. Kim, Y. Lee, X. Xu, J.-S. Park, Y. Zheng , J. Balakrishnan, T. Lei, H. Ri Kim, Y. I. Song, Y.-J. Kim, K. S. Kim, B. Ozyilmaz, J.-H. Ahn, B. H. Hong, S. Iijima, *Nat. Nanotechnol.*, **2010**, *5*, 574.

[46] W. Cai, R. D. Piner, Y. Zhu, X. Li, Z. Tan, H. C. Floresca, C. Yang, L. Lu, M. J. Kim, R. S. Ruoff, *Nano Res.*, **2009**, *2*, 851.

[47] A. Reina, X. Jia, J. Ho, D. Nezich, H. Son, V. Bulovic, M. S. Dresselhaus, J. Kong, *Nano Lett.*, **2009**, *9*, 30.

[48] G. Lopez, E. Mittemeijer, *Scr. Mater.*, **2004**, *51*, 1.

[49] G. L. Selman, P. J. Ellison, A. s. Darling, *Platinum Metals Rev.*, **1970**, *14*, 14.

[50] S. Bhaviripudi, X. Jia, M. S. Dresselhaus, J. Kong, *Nano Lett.*, **2010**, *10*, 4128.

[51] K. Yan, H. Peng, Y. Zhou, H. Li, Z. Liu, *Nano Lett.*, **2011**, *11*, 1106.

[52] S. Chen, W. Cai, R. D. Piner, J. W. Suk, Y. Wu, Y. Ren, J. Kang, R. S. Ruoff, *Nano Lett.*, **2011**, *11*, 3519.

[53] J. Wu, W. Pisula, K. Muellen, *Chem. Rev.*, **2007**, *107*, 718.

[54] X. Yang, X. Dou, A. Rouhanipour, L. Zhi, H. J. Rader, K. Müllen, *J. Am. Chem. Soc.*, **2008**, *130*, 4216.

[55] J. Cai, P. Ruffieux, R. Jaafar, M. Bieri, T. Braun, S. Blankenburg, M. Muoth, A. P. Seitsonen, M. Saleh, X. Feng, K. Muellen, R. Fasel, *Nature*, **2010**, *466*, 470.

[56] X. Yan, X. Cui, L.-s. Li, *J. Am. Chem. Soc.*, **2010**, *132*, 5944.

[57] X. Yan, X. Cui, B. Li, L.-s. Li, *Nano Lett.*, **2010**, *10*, 1869.

[58] W. H. Lee, J. Park, S. H. Sim, S. B. Jo, K. S. Kim, B. H. Hong, K. Cho, *Adv. Mater.*, **2011**, *23*, 1752.

[59] W. J. Yu, S. H. Chae, S. Y. Lee, D. L. Duong, Y. H. Lee, *Adv. Mater.*, **2011**, *23*, 1889.

[60] R.-H. Kim, M.-H. Bae, D. G. Kim, H. Cheng, B. H. Kim, D.-H. Kim, M. Li, J. Wu, F. Du, H.-S. Kim, S. Kim, D. Estrada, S. W. Hong, Y. Huang, E. Pop, J. A. Rogers, *Nano Lett.*, **2011**, *11*, 3881.

[61] K. S. Kim, Y. Zhao, H. Jang, S. Y. Lee, J. M. Kim, K. S. Kim, J. H. Ahn, P. Kim, J.-Y. Choi, B. H. Hong, *Nature*, **2009**, *457*, 706.

[62] L. Hu, J. Li, J. Liu, G. Gruener, T. Marks, *Nanotechnology*, **2010**, *21*, 155202.

[63] S.-K. Lee, B. J. Kim, H. Jang, S. C. Yoon, C. Lee, B. H. Hong, J. A. Rogers, J. H. Cho, J.-H. Ahn, *Nano Lett.*, **2011**, *11*, 4642.

[64] N. M. R. Peres, F. Guinea, A. H. C. Neto, *Ann. Phys.*, **2006**, *321*, 1559.

[65] M. J. Allen, V. C. Tung, L. Gomez, Z. Xu, L. –M. Chen, K. S. Nelson, C. Zhou, R. B. Kaner, Y. Yang, *Adv. Mater.*, **2009**, *21*, 2098.

[66] X. Li, X. Wang, L. Zhang, S. Lee, H. Dai, *Science*, **2008**, *319*, 1229.

[67] S. J. Kang, B. Kim, K. S. Kim, Y. Zhao, Z. Chen, G. H. Lee, J. Hone, P. Kim, C. Nuckolls, *Adv. Mater.*, **2011**, *23*, 3531.

[68] S. Lee, B. J. Kim, H. Jang, S. C. Yoon, C. Lee, B. H. Hong, J. A. Rogers, J. H. Cho, J. Ahn, *Nano Lett.*, **2011**, *11*, 4642.

[69] Y. P. Dan, Y. Lu, N. J. Kybert, Z. T. Luo, A. T. C. Johnson, *Nano Lett.*, **2009**, *9*, 1472.

[70] L. H. Tang, Y. Wang, Y. M. Li, H. B. Feng, J. Lu, J. H. Li, *Adv. Funct. Mater.*, **2009**, *19*, 2782.

[71] Y. Ohno, K. Maehashi, Y. Yamashiro, K. Matsumoto, *Nano Lett.*, **2009**, *9*, 3318.

[72] V. Dua, S. P. Surwade, S. Ammu, S. R. Agnihotra, S. Jain, K. E. Roberts, S. Park, R. S. Ruoff, S. K. Manohar, *Angew. Chem. Int. Ed.*, **2010**, *49*, 2154.

[73] V. K. Kodali, J. Scrimgeour, S. Kim, J. H. Hankinson, K. M. Carroll, W. A. de Heer, C. Berger, J. E. Curtis, *Langmuir*, **2011**, *27*, 863.

[74] J. Jang, J. Bae, M. Choi, *Carbon*, **2005**, *43*, 2730.

[75] M. Choi, B. Lim, J. Jang, *Macromol. Res.*, **2008**, *16*, 200.

[76] M. D. Stoller, S. Park, Y. Zhu, J. An, R. S. Ruoff, *Nano Lett.*, **2008**, *8*, 3498.

[77] A. V. Murugan, T. Muraliganth, A. Manthiram, *Chem. Mater.*, **2009**, *21*, 5004.

[78] J. Yan, T. Wei, B. Shao, Z. Fan, W. Qian, M. Zhang, F. Wei, *Carbon*, **2010**, *48*, 487.

[79] W. Gao, N. Singh, L. Song, Z. Liu, A. L. M. Reddy, L. Ci, R. Vajtai, Q. Zhang, B. Wei, P. M. Ajayan, *Nat. Nanotechnol.*, **2011**, *6*, 496.

[80] G. Zheng, L. Hu, H. Wu, X. Xie, Y. Cui, *Energy Environ. Sci.*, **2011**, *4*, 3368.

[81] S. Yoon, S. Lim, S. Hong, W. Qiao, D. D. Whitehurst, I. Mochida, B. An, K. Yokogawa, *Carbon*, **2004**, *43*, 1828.

[82] S. Helveg, C. Lopez-Cartes, J. Sehested, P. L. Hansen, B. S. Clausen, J. R. Rostrup-Nielsen, F. Abild-Pedersen, J. S. Norskov, *Nature*, **2004**, *427*, 426.

[83] W. S. Hummers, R. E. Offeman, *J. Am. Chem. Soc.*, **1958**, *80*, 1339.

[84] A. B. Bourlinos, D. Gournis, D. Petridis, T. Szabo, A. Szeri, I. Dekany, *Langmuir*, **2003**, *19*, 6050.

[85] H. Y. He, T. Riedl, A. Lerf, J. Kliowski, *J. Phys. Chem.*, **1996**, *100*,

19954.

[86] A. Lerf, H. Y. He, M. Forster, J. Klinowski, *J. Phys. Chem. B*, **1998**, *102*, 4477.

[87] Y. Zhou, Q. Bao, L. A. L. Tang, Y. Zhong, K. P. Loh, *Chem. Mater.*, **2009**, *21*, 2950.

[88] J. P. Rourke, P. A. Pandey, J. J. Moore, M. Bates, I. A. Kinloch, R. J. Young, N. R. Wilson, *Angew. Chem. Int. Ed.*, **2011**, *50*, 3173.

[89] D. V. Kosynkin, A. L. Higginbotham, A. Sinitskii, J. R. Lomeda, A. Dimiev, B. K. Price, J. M. Tour, *Nature*, **2009**, *458*, 872.

[90] C. Y. Su, Y. Xu, W. Zhang, J. Zhao, X. Tang, C. H. Tsai, L. J. Li, *Chem. Mater.*, **2009**, *21*, 5674.

[91] C. Y. Su, Y. Xu, W. Zhang, J. Zhao, A. Liu, X. Tang, C. H. Tsai, Y. Huang, L. J. Li, *ACS Nano*, **2010**, *4*, 5285.

[92] F. Leroux, E. Raymundo-Pinero, J. –M. Nedelec, F. Beguin, *J. Mater. Chem.*, **2006**, *16*, 2074.

[93] D. F. Rohlfing, A. Kuhn, *Carbon*, **2006**, *44*, 1942.

[94] L. Jiao, X. Wang, G. Diankov, H. Wang, H. Dai, *Nature Nanotech.*, **2010**, *5*, 321.

[95] M. S. Dresselhaus G. Dresselhaus, R. Saito, A. Jorio, *Phys. Rep.*, **2005**, *409*, 47.

[96] K. –Y. Shin, J. –Y. Hong, J. Jang, *Adv. Mater.*, **2011**, *23*, 2113.

[97] H. Nakagawa, K. Watanabe, Y. Harada, K. Miura, *Carbon*, **1999**, *37*, 1455.

[98] J. Jang, J. H. Oh, G. D. Stucky, *Angew. Chem. Int. Ed.*, **2002**, *41*, 4016.

[99] J. Jang, J. H. Oh, *Chem. Commun.*, **2004**, 882.

[100] J. Jang, J. H. Oh, *Adv. Mater.*, **2004**, *16*, 1650.

[101] J. Jang, H. Yoon, *Small*, **2005**, *1*, 1195.

[102] J. H. Lee, D. W. Shin, V. G. Makotchenko, A. S. Nazarov, V. E. Fedorov, J. H. Yoo, S. M. Yu. J. –Y. Choi, J. M. Kim, J. –B. Yoo, *Small*, **2010**, *6*, 58.

[103] H. A. Becerril, J. Mao, Z. Liu, R. M. Stoltenberg, Z. Bao, Y. Chen, *ACS Nano*, **2008**, *2*, 463.

[104] X. Wang, L. Zhi, K. Muüllen, *Nano Lett.*, **2008**, *8*, 323.

[105] M. Lotya, Y. Hernandez, P. J. King, R. J. Smith, V. Nicolosi, L. S. Karlsson, F. M. Blighe, S. De, Z. Wang, I. T. McGovern, G. S. Duesberg, J. N. Coleman, *J. Am. Chem. Soc.*, **2009**, *131*, 3611.

[106] S. Stankovich, D. A. Dikin, R. D. Piner, K. A. Kohlhaas, A. Kleinhammes, Y. Jia, Y. Wu, S. T. Nguyen, R. S. Ruoff, *Carbon*, **2007**, *45*, 1558.

[107] D. W. Boukhvalov, M. I. Katsnelson, *J. Am. Chem. Soc.*, **2008**, *130*, 10697.

[108] J. T. Robinson, M. Zalalutdinov, J. W. Baldwin, E. S. Snow, Z. Wei, P. Sheehan, B. H. Houston, *Nano Lett.*, **2008**, *8*, 3441.

[109] H. A. Becerril, J. Mao, Z. Liu, R. M. Stoltenberg, Z. Bao, Y. Chen, *ACS Nano*, **2008**, *2*, 463.

[110] J. Cho, K.-H. Shin, J. Jang, *Synthetic Metals*, **2010**, *160*, 1119.

[111] H. Yoon, J. Jang, *Adv. Funct. Mater.*, **2009**, *19*, 1567.

[112] V. Dua, S. P. Surwade, S. Ammu, S. R. Agnihotra, S. Jain, K. E. Roberts, S. Park, R. S. Ruoff, S. K. Manohar, *Angew. Chem. Int. Ed.*, **2010**, *49*, 2154.

[113] N. A. Luechinger, S. Loher, E. K. Athanassiou, R. N. Grass,W. J. Stark, *Langmuir*, **2007**, *23*, 3473.

[114] M. Dragoman, A. A. Muller, D. Dragoman, F. Coccetti, R. Plana, *J. Appl. Phys.*, **2010**, *107*, 104313.

[115] J. H. So, J. Thelen, A. Qusba, G. J. Hayes, G. Lazzi, M. D. Dickey, *Adv. Funct. Mater.*, **2009**, *19*, 3632.

[116] M. Kubo, X. Li, C. Kim, M. Hashimoto, B. J. Wiley, D. Ham, G.M. Whitesides, *Adv. Mater.*, **2010**, *22*, 2749.

[117] S. Cheng , A. Rydberg , K. Hjort , Z. Wu , *Appl. Phys. Lett.*, **2009**, *94*,

144103.

[118] Y. Tikhov, J. H. Won, *Electronics Letters*, **2004**, *40*, 574.

[119] H. Sirringhaus, T. Kawase, R. H. Friend, T. Shimoda, M. Inbasekaran, W. Wu, E. P. Woo, *Science*, **2000**, *290*, 2123.

[120] Y. Yoshioka, P. D. Calvert, G. E. Jabbour, *Macromol. Rapid. Commun.*, **2005**, *26*, 238.

[121] T. Ding, Y. Tian, K. Liang, K. Clays, K. Song, G. Yang, C. -H. Tung, *Chem. Commun.*, **2011**, *47*, 2429.

[122] N. Vandencasteele, D. Merche, F. Reniers, *Surf. Interface Anal.*, **2006**, *38*, 526.

[123] F. Tuinstra, J. L. Koenig, *J. Chem. Phys.*, **1970**, *53*, 1126.

[124] A. Vesel, M. Mozetic, A. Zalar, *Vacuum*, **2008**, *82*, 248.

[125] J.–Y. Hong, J. Jang, *Soft matter*, **2010**, *6*, 4669.

[126] J.–Y. Hong, E. Kwon, J. Jang, *Soft Matter*, **2009**, *5*, 951.

[127] J.–Y. Hong, M. Choi, C. Kim, J. Jang, *J. Colloid. Interface Sci.*, **2010**, *347*, 177.

[128] J. Yin, X. Zhao, L. Xiang, X. Xia, Z. Zhang, *Soft Matter*, **2009**, *5*, 4687.

[129] P. Tan, J. Huang, D. Liu, W. Tian, L. Zhou, *Soft Matter*, **2010**, *6*, 4800.

[130] W. Wen, X. Huang, P. Sheng, *Soft Matter*, **2008**, *4*, 200.

[131] Y. G. Ko, U. S. Choi, *Soft Matter*, **2012**, *8*, 253.

[132] J. Yin, W. Wang, R. Chang, X. Zhao, *Soft Matter*, **2012**, *8*, 294.

[133] W. L. Zhang, B. J. Park, H. J. Choi, *Chem. Comm.*, **2010**, *46*, 5596.

[134] W L. Zhang, H. J. Choi, *Chem. Comm.*, **2011**, *47*, 12286.

[135] H. Hu, X. Wang, J. Wang, F. Liu, M. Zhang, C. Xu, *Appl. Surf. Sci.*, **2011**, *257*, 2637.

[136] X. Zhang, A. C. Coleman, N. Katsonis, W. R. Browne, B. J. Wees, B. L. Feringa, *Chem. Comm.*, **2010**, *46*, 7539.

[137] Y. Si, E. T. Samulski, *Chem. Mater.*, **2008**, *20*, 6792.

[138] T. Hao, *Adv. Mater.*, **2001**, *13*, 1847.

[139] J. B. Yin, X. P. Zhao, *J. Phys. Chem. B*, **2006**, *110*, 12916.

[140] S. Park, M. Cho, S. Lim, H. J. Choi, M. Jhon, *Macromol. Chem. Phys.*, **2005**, *26*, 1563.

[141] B. Wang, X. Zhao, *Langmuir*, **2005**, *21*, 6553.

[142] H. Yilmaz, U. Yilmaz, *J. Appl. Polym. Sci.*, **2007**, *103*, 3798.

[143] T. Uemure, K. Minagawa, K. Koyama, *Polym. Prepr. Jpn.*, **1994**, *43*, 1286.

국문초록

지난 수년 동안 집중적인 연구적 관심을 불러 일으키고 있는 그래핀은 탄소원자가 한층으로 벌집모양의 육각형의 격자를 가진 탄소의 2차원적인 동소체이다. 그래핀의 높은 전자이동도나 높은 전기전도도 등의 물리적 특성뿐만 아니라 우수한 광투과도와 같은 그들 고유구조 특성에 기인한 서로운 물성을 바탕으로 전자공학, 광전자공학, 촉매반응, 에너지 저장 및 변환, 생의학 등의 다양한 분야에 적용되고 있다.

본 연구에서는 하향식/상향식 접근방법을 이용하여 형태조절된 그래핀 나노재료를 제조하였으며, 이들의 형성 메커니즘을 체계적으로 고찰하였고, 아울러 투명전극소재, 다이폴 안테나, 음향 작동장치, 전기유변유체로의 응용에 대해 살펴보았다.

하향식 접근방법으로, 그래핀은 탄소나노섬유의 횡단절단법을 이용해 제조할 수 있었다. 결정성이 우수한 카본나노섬유의 단순한 산화 및 박리공정을 통해서 형태 조절된 그래핀이 제조되었다. 더불어, 카본나노섬유의 결정구조 및 직경에 따라서 최종적인 그래핀의 형태 및 크기 또한 조절 할 수 있었다. 뿐만 아니라 그래핀 본래의 전기적, 물리적 특성을 활용하기 위해서 필요한 산화그래핀의 환원공정으로 나노분산기를 이용한 물리적 환원방법을 제안하였다. 물리적 환원방법을 통해서 환원제 없이 성공적으로 환원된 그래핀을 얻을 수 있었다.

상향식 접근방법으로, 층상자기조립법을 이용하여 그래핀을 제조할 수 있었다. 층상자기조립법으로 형성된 폴리알릴아민/폴리스티렌설포네이트 다층막은 금속도펀트 존재하에 탄화공정을 거쳐 그래핀을 형성함을 확인하였다. 탄화공정을 통한 그래핀 형성 시, 폴리스티렌설포네이트 와 폴리알릴아민은 각각 탄소원 및 보호막의 역할을 각각 담당함을 알 수 있었다. 또한 그래핀 형성 시 금속도펀트는 폴리스티렌설포네이트 구조변화의 촉매로 작용하여 비교적 낮은 온도에서 그래핀을 성공적으로 제조 할 수 있었다.

본 연구에서 새롭게 개발한 하향식/상향식 접근방법은 제어된 크기 및 모양을 지닌 다양한 종류의 그래핀 제조에 적용될 수 있으며, 이를 통해 투명전극소재, 다이폴 안테나, 음향 작동장치, 전기유변유체를 포함한 여러가지 응용분야에 폭넓게 활용될 수 있을 것으로 사료된다.

주요어: 탄소나노물질, 그래핀, 제조방법, 하향식, 상향식, 투명전극, 전기유변유체

학번: 2006-21396

감사의 글

서울대학교 고분자재료 실험실에 입학한지 어느덧 7년이라는 세월이 흘렀습니다. 대학원 생활은 학부과정에서 얻을 수 없었던 전공 지식, 인간관계, 책임감 등에 대해 배울 수 있었던 매우 소중한 배움의 시간이었으며, 제 인생의 매우 소중한 자산이 될 것으로 생각됩니다. 짧은 글이지만 이 글을 통해서 대학원 생활에 도움을 주신 분들에게 감사를 표하고자 합니다.

우선 부족한 저를 열정적으로 지도해 주신 장정식 교수님께 감사의 말씀을 드립니다. 연구에 대한 무한한 열정과 모범적인 생활태도를 바탕으로 많은 학문적 가르침을 주셨고, 때로는 아버지와 같은 자상함으로 인생에 대한 귀중한 조언을 아끼지 않으셨습니다. 고통이 없으면 결과도 없다는 말씀과 늘 긍정적으로 생각하라는 말씀은 저뿐만 아니라 모든 제자들의 마음속에서 가장 큰 힘과 재산으로 빛날 것입니다. 앞으로도 교수님의 가르침을 거울삼아 부끄럽지 않은 제자가 될 수 있도록 열심히 노력할 것입니다. 항상 건강하시고 가정에 행복한 일만 넘치시길 바랍니다. 또한 바쁘신 중에도 부족한 논문을 심사해 주시고 조언해주신 조재영 교수님, 김영규 교수님, 이종찬 교수님, 임순호 박사님께도 깊은 감사의 말씀 드립니다. 그리고 실험실에서 동고동락했던 선·후배님을 포함한 여러 지인들과 맺은 소중한 인연에 깊이 감사하며 말로는 다 표현하기 힘든 고마움을 전합니다.

박사학위 종심발표날, 제가 얼마나 행복하며 부족한게 없는 사람인가 하는 아주 충만한 행복감을 느꼈습니다. 이 충만함의 근원은 바로 사랑하는 아내와 양가 부모님들 누나와 매형 그리고 처남이 제 옆에 있기 때문일 것입니다. 정말 저에게 너무 소중한 분들입니다. 가족분들의 격려와 도움이 없었으면 이렇게 무사히 학위를 마치는 저 자신도 없었을 것입니다. 그렇지만 단순히 학위를 마치며 감사의 마음을 전한다는 것이 또한 저어되기도 합니다. 더 큰 감사와 고마움을 표현하고 싶습니다.

우선 사랑하는 저의 아내 윤지에게 고마움과 감사함을 전하겟습니다. 학위과정중 저를 위해 배려해주고 믿어주고 저에게 용기를 북돋아 주었습니다. 또한, 인생에 대한 멋진 가치관과 큰 그림을 공유하며 저에게 인생의 동반자로서 많은 도움과 힘을 주었습니다. 늘 건강하게 저와 함께 행복한 가정 평생 꾸며 나갔으면 좋겠습니다. 저도 많이 노력하겠습니다.

“언제나 최선을 다해라” 라고 말씀하시고 삶으로 직접 보여주신 아버님과 어머님께 특별한 감사를 드립니다. 아버님 어머님께는 항상 죄송스럽고 또한 너무 고맙고 감사드립니다. 올바른 가치관과 바른 생활 태도를 갖도록 끊임없이 보살펴 주시면서 건강하게 키워주신 점, 그리고 무엇보다 부모가 자식에에 보여줄 수 있는 아무 조건없는 그 크고 아름다운 사랑을 몸소 실천하고 베풀어주신 것에 대해서 정말 더 깊은 감사와 고마움을 느낍니다. 항상 건강하시고 행복한 모습 오래도록 뵙고 싶습니다. 아버님 어머님 사랑합니다.

지금 부모님을 도와 언제나 열심히 노력하는, 마음이 저보다 훨씬 큰 누나는 저의 든든한 버팀목 입니다. 지금까지 살면서 누나가 없었으면 얼마나 외롭고 허전했을지 모릅니다. 착한 매형과 사랑스런 조카 화영이를 만나게 해주어서 이 또한 너무 고마운 일이 아닐 수 없습니다. 항상 누나가 원하는 일이 잘 되리라 믿고, 행복하고 건강하기를 바랍니다.

결혼을 하면서 또 한분의 아버님과 어머님을 만나게 된 것도 행운입니다. 항상 챙겨주시고 격려해주신 점 그리고 무엇보다도 저를위해 늘 기도해주셔서 정말 감사드립니다. 늘 건강하시고 행복하게 지내시길 기도드립니다. 저희 부부 또한 주님의 뜻을 따라 믿음의 가정 이룰 수 있도록 노력하겠습니다. 그리고 항상 듬직한 처남 광명이도 지금 대학원에서 신학을 공부하고 있습니다. 공부 및 미래에 대한 탐색과 계획의 시간속에서 어떤 결정을 내리던지 항상 최선의 선택일 것이라 믿습니다. 따뜻하고 멋진 품성 그대로 항상 건강하고 행복하기를 바랍니다.

지금의 제가 있기까지 정말 여러 분들의 도움과 사랑이 있었습니다. 이런 깨달음은 제가 앞으로 살아가면서 겸손한 태도로 남과 더불어 살아가는데 큰 가르침으로 인도해 줄 것입니다. 또한 좋은 남편이자, 부모이자, 자식으로써 열심히 생활하겠습니다. 주변 모든 분들의 행복과 건강을 다시 한번 진심으로 기원하면서 마칩니다. 감사합니다.

2013년 2월, 관악을 내려가며

홍진용 드림